中央大学博士論文

A Study on Metamaterial Transmission Lines for RF and Microwave Applications

CHU BA HIEN

博士 (工学)

中央大学大学院 理工学研究科 情報セキュリティ科学専攻

Information Security Science Course

Graduate School of Science and Engineering

Chuo University

March 2018

Contents

List of Figures

List of Tables

Chapter 1

Introduction

1.1 Metamaterials

A basic material classification can be established regarding signs of permittivity ε and permeability μ of materials. This common classification is divided into four parts of positive and negative values in Fig. 1.1 as follows:

- Double Positive (DPS): $\varepsilon > 0$, $\mu > 0$
- Double Negative (DNG): $\varepsilon < 0$, $\mu < 0$
- Mu Negative (MNG): $\varepsilon > 0$, $\mu < 0$
- Epsilon Negative (ENG): $\varepsilon < 0$, $\mu > 0$

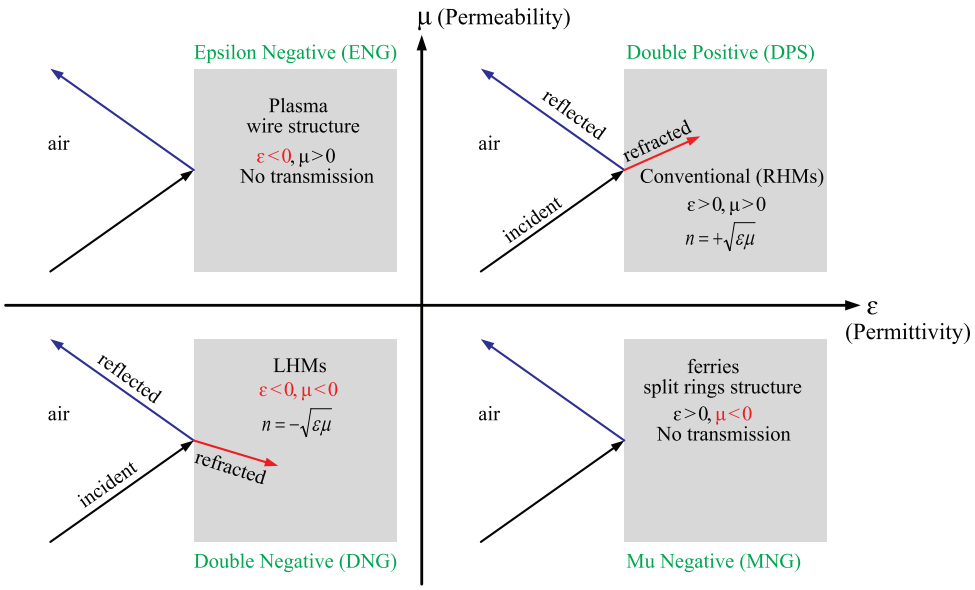

Figure 1.1: Basic classification of materials in ε and μ plane.

Conventional materials exhibit Double Positive (DPS) signs of the permittivity ε and the permeability μ and follow a right handed triad rule as shown in Fig. 1.2 (a). So, these materials are called by Right Handed Materials (RHMs).

The ancient Greek prefix "*Meta*" means "*Beyond*". Terminology "*Metamaterial*" has been used to describe a composite material in form of effective medium which can have negative permittivity ε and/or negative permeability μ. Metamaterials include Double Negative (DNG), Mu Negative (MNG) and Epsilon Negative (ENG) materials. In addition, Double Negative (DNG) materials are called by Left Handed Materials (LHMs) since the electric field, magnetic field, and phase constant propagation vectors follow left handed triad rule in the LHMs as shown in Fig. 1.2 (b). The theoretical speculation of electromagnetic metamaterials was first presented by Veselago [1]. He proposed the existence of "substances with simultaneously negative permittivity ε and permeability μ". As the result, LHMs support electromagnetic waves with anti-parallel phase and group velocities that are also known as backward waves. Compared with RHMs, this unique electromagnetic property induces different phenomena, such as reversals of Snell's law (negative index of refraction), the Doppler effect, and the Cerenkov effect. An example for backward waves and negative index of refraction is shown in Fig. 1.3.

With the non-existence in nature and lack of experimental verification, metamaterials attract few attention over 30 years in science community. In 1998, thin wire structures (TWs) exhibit a negative value of effective permittivity which was first demonstrated by Pendry [2]. In 1999, he presented split ring resonator structures (SRRs) with a negative value of effective permeability [3]. Shelby and Smith verified a negative index of refraction of negative ε and negative μ by constituting TWs and SRRs in 2001 [4]. Then metamaterials have attracted much attention in theoretical exploration as well as experimental study for their unique electromagnetic properties.

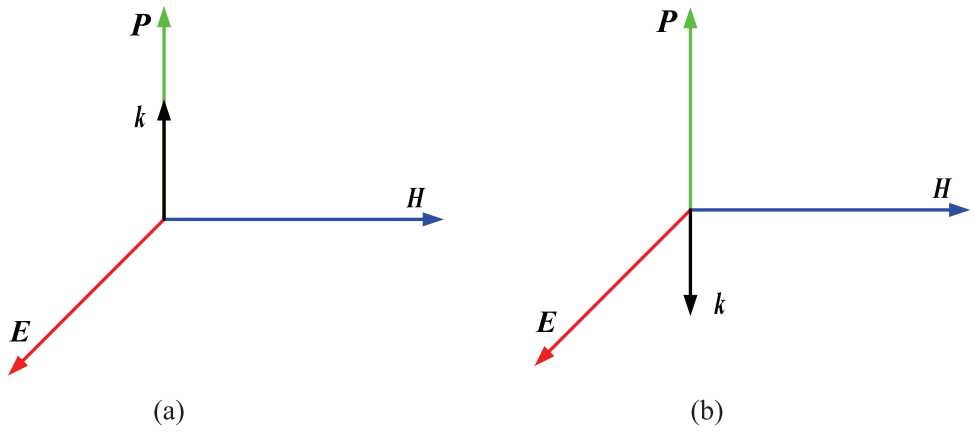

Figure 1.2: (a) Right handed triad. (b) Left handed triad.

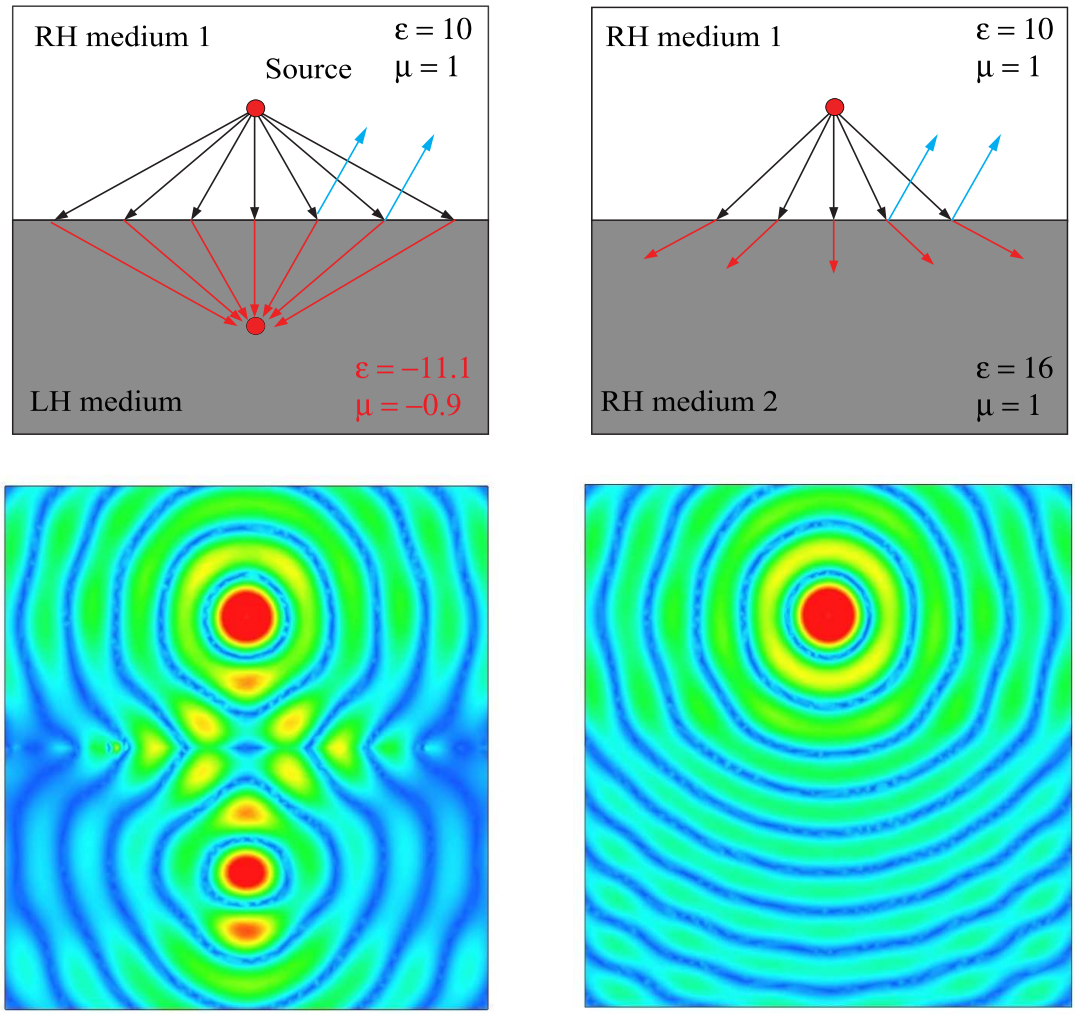

Figure 1.3: The HFSS simulated result of negative refraction (left) and positive refraction (right) at 10 GHz.

Later, a transmission line approach for metamaterials was first introduced approximately at the same time in June 2002 by three different groups, Eleftheriades [5], Oliner [6], and Caloz [7]. The proposed structures consist simply of L-C elements loaded-transmission line networks and are called by left-handed transmission line (LH TL) or negative-refractive-index transmission line (NRI TL). In 2006, composite right/left-handed transmission line (CRLH TL) and dual composite right/left-handed transmission line (D-CRLH L) are presented by Caloz [8, 9]. The CRLH TL exhibits a LH band at low frequency, a RH band at high frequency, and is of pass-band while D-CRLH TL is in opposition. More recently, an extended-composite right/left-handed transmission line (E-CRLH TL) has been combined from CRLH and D-CRLH TLs to get more involved band structures [10]. This TL is also known as a generalized negative refraction index transmission line (NRI TL) [11].

1.2 Motivation

The rapid development of wireless communication systems is bringing new challenges. Firstly, there is a trend towards the miniaturization of components associated with handheld devices. So the space left for the engineers to integrate all the necessary components becomes smaller. When miniaturizing, the RF and microwave modules are very difficult to reduce the size. This is mainly because the size of these devices is highly dependent on the operational frequency. Secondly, manufacturers also require low cost in fabrication while maintaining good performance.

Metamaterial technologies provide an opportunity to solve the new challenges. Metamaterials have been applied to a large number of RF and microwave devices including antennas, filters, power dividers and direction couplers with many advantages of multiband and small size. For example, metamaterials enable the antennas to be multiband and sized on the order of one-tenth the operating wavelength and providing performance better than conventional microstrip antennas sized of one-half the wavelength, thereby providing a five times the size reduction. Moreover, metamaterials can also be used to design absorbers [12], microwave lens [13], and metamaterial slabs for enhancing gain of the antennas [14] and efficiency of wireless power transfers [15, 16, 17].

These reasons are my motivation to do research on metamaterials with metamaterial transmission line approach as well as resonant metamaterial approach to utilize metamaterial technologies for RF and microwave applications.

1.3 Objectives

An objective of this study is to bring new research results and applications for extended-composite right/left handed transmission line (E-CRLH TL), the most recent metamaterial transmission lines. It paves the way for novel arbitrary dual-, tri- and quad-band RF and microwave components.

Beside multiband applications, there is a growing demand for faster data transmission of ultra wide band (UWB) applications. Antipodal Vivaldi antenna is a candidate for UWB applications. With resonant metamaterial approach, we improve gain of the antipodal Vivaldi antenna by using nearly zero-index metamaterial (ZIM) unit cell. Before combining with the ZIM unit cell, the single antipodal Vivaldi is designed to exhibit a very good performance to compare the previous antipodal Vivaldi antenna. In addition, a new estimation method for the operational low frequency end of the Vivaldi antenna is presented in this study.

Summarily, this thesis has four highlight points as follows:

- Analysis and design of E-CRLH TL with new closed-form solutions.
- A compact metamaterial antenna based on E-CRLH unit cell for multiband applications.
- An antipodal Vivaldi antenna for UWB applications and new estimation method for the operational low frequency end.
- Zero-index metamaterial (ZIM) unit cell for improving gain of antipodal Vivaldi antennas.

1.4 Thesis outline

From above stated objectives, this thesis is divided into four chapters.

Chapter 2 will have three sections. Section 2.1 starts with the basic model for conventional transmission line and is followed by the analysis of homogeneous CRLH, D-CRLH and E-CRLH TLs. L-C loaded unit cell networks approached by Bloch-Floquet analysis are introduced at the end of this section. New closed-form solutions are developed in Section 2.2 and presented for deriving inductance and capacitance elements of the E-CRLH unit cell from the cut-off frequencies of right-handed (RH) and left-handed (LH) bands. The characteristics of the E-CRLH TL are calculated for unbalanced, balanced, and mixed cases. The dispersion diagram, the Bloch impedance, S-parameters are also investigated. The usefulness of our method has been shown in detail by designing the desired characteristics for various cases. In Section 2.3, a compact quad-band antenna is designed from an unit cell of asymmetric E-CRLH TL as the main resonator part and a 50 Ω coplanar waveguide (CPW) as the feeding part. The design concept and the resonant frequencies are analyzed and discussed. The results show that the proposed antenna exhibits four frequency bands covering GSM810, WLAN 2.45/5.5 GHz and WiMAX 3.5 GHz bands. The overall size of the fabricated antenna is only 57.2 mm $\times$ 31.2 mm $\times$ 1.6 mm and is very small to compare with other proposed quad-band antennas. In addition, a good agreement can be observed among the estimated resonant frequencies, HFSS simulated and measured results.

Chapter 3 entitled as resonant metamaterials, will present a robust method to retrieve effective parameters of resonant metamaterials in Section 3.1, and zero-index metamaterial (ZIM) unit cell for improving gain of antipodal Vivaldi antennas in Section 3.2. The first section of this chapter, refractive index n, impedance z, permittivity ε and permeability μ of resonant metamaterials are retrieve from S-parameters. This method is very useful for designing resonant metamaterial unit cells. In Section 3.2, a simple approach is

presented for designing antipodal Vivaldi antennas. A new and better estimation of the low frequency end of the operational range is shown. Final dimensions of the antenna parameters are determined by using the commercially available simulation software (High Frequency Structure Simulator, HFSS). The proposed antenna has simple configuration but exhibits low return loss, good radiation characteristics, high and flat gain in the operating ultra wideband frequency range (3.1–10.6 GHz). The fabrication has been done along with the specification to confirm the properties by measurements. Then, the gain of the designed antipodal Vivaldi antenna is enhanced by arranging zero-index metamaterial (ZIM) unit cells in the aperture of the antenna. The effective parameters of the proposed ZIM unit cell are calculated from the robust method in Section 3.1. With an optimized configuration, an improved gain to compare conventional methods is observed.

Finally, conclusions are made in Chapter 4.

In the following discussion, the time harmonic factor $e^{j\omega t}$ is assumed and suppressed throughout the context.

Chapter 2

Metamaterial transmission lines

2.1 Metamaterial transmission line theory

2.1.1 Introduction

Transmission line theory has a significant important in RF and microwave circuits since it is the gap between field analysis and circuit theory. In this section, we will see the phenomenon of wave propagation on a conventional transmission line and metamaterial transmission lines which are approached from an extension of circuit theory.

Firstly, basic model for a conventional transmission line is presented Section 2.1.2. Composite right/left-handed transmission line (CRLH TL) is outlined in Section 2.1.3. The CRLH TL exhibits a LH band at low frequency, a RH band at high frequency, and is of pass-band [8]. In opposition to the CRLH TL, D-CRLH TL exhibits a LH band at high frequency, a RH band at low frequency, and is of stop-band nature [9]. These characteristics of the D-CRLH TL are shown in Section 2.1.4. As a consequence, the E-CRLH TL has been combined from CRLH and D-CRLH TLs to get more involved band structures [10]. This TL also known as a generalized negative refraction index transmission line (NRI TL) [11]. The E-CRLH TL exhibits two LH and two RH bands and is presented in Section 2.1.5. Any practical implementation of these metamaterial transmission line must be periodic structure. Hence, analysis of periodic L-C loaded unit cell networks are presented in Section 2.1.6.

2.1.2 Basic model for a conventional transmission line

A conventional transmission line is often schematically represented as a two-conductor line in Fig. 2.1 (a). The piece of infinitesimal length Δz of transmission line can be modeled as shown in Fig. 2.1 (b), where R, L, C, and G are per-unit-length quantities defined as follows:

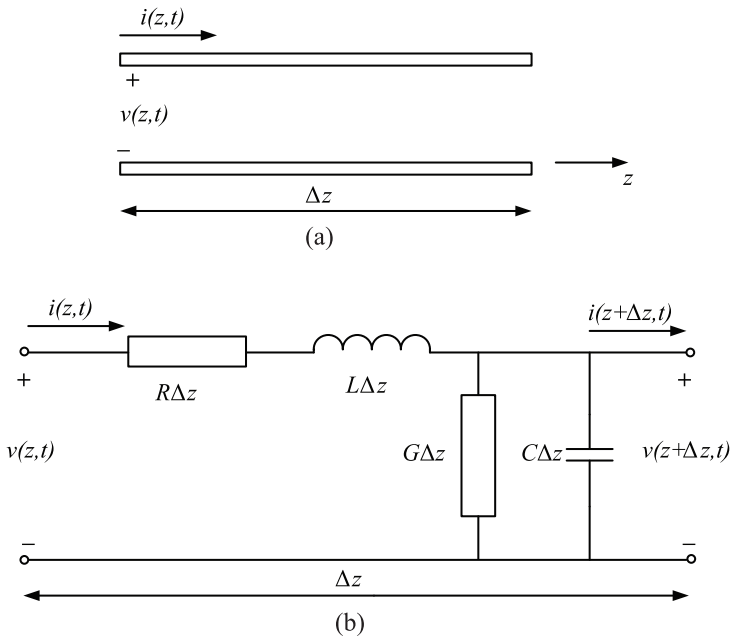

Figure 2.1: (a) Voltage and current distribution in a conventional transmission line. (b) Its equivalent circuit [18].

R = series resistance per unit length in [Ω/m].

L = series inductance per unit length in [H/m].

C = shunt capacitance per unit length in [F/m].

G = shunt conductance per unit length in [S/m].

Applying Kirchhoff's voltage and current laws for equivalent circuit in Fig. 2.1 (b), we have

$$v(z,t) - R\Delta z i(z,t) - L\Delta z \frac{\partial i(z,t)}{\partial t} - v(z+\Delta z,t) = 0, \tag{2.1}$$

$$i(z,t) - G\Delta z v(z+\Delta z,t) - C\Delta z \frac{v(z+\Delta,t)}{\partial t} - i(z+\Delta z,t) = 0. \tag{2.2}$$

Then dividing Eqs. (2.1) and (2.2) by Δz and taking the limit as $\Delta z \to 0$ gives the following differential equations

$$\frac{\partial v(z,t)}{\partial z} = -Ri(z,t) - L\frac{\partial i(z,t)}{\partial t}, \tag{2.3}$$

$$\frac{\partial i(z,t)}{\partial z} = -Gv(z,t) - C\frac{\partial v(z,t)}{\partial t}. \tag{2.4}$$

Two equation above are called "*Telegrapher equations*". For the sinusoidal steady-state condition, with cosine-based phasors, Equations (2.3) and (2.4) simplify to

$$\frac{dV(z)}{dz} = -(R + j\omega L)I(z), \tag{2.5}$$

$$\frac{dI(z)}{dz} = -(G + j\omega C)V(z). \tag{2.6}$$

Wave equations for $V(z)$ and $I(z)$ can be solved from Eqs. (2.5) and (2.6) as

$$\frac{d^2V(z)}{dz^2} - \gamma^2 V(z) = 0, \tag{2.7}$$

$$\frac{d^2I(z)}{dz^2} - \gamma^2 I(z) = 0, \tag{2.8}$$

where

$$\gamma = \alpha + j\beta = \sqrt{(R + j\omega L)(G + j\omega C)}, \tag{2.9}$$

is the complex propagation constant. One gets travelling wave solution from Eqs. (2.7) and (2.8) as

$$V(z) = V_0^+ e^{-\gamma z} + V_0^- e^{\gamma z}, \tag{2.10}$$

$$I(z) = I_0^+ e^{-\gamma z} + I_0^- e^{\gamma z}, \tag{2.11}$$

where $e^{-\gamma z}$ is the wave propagation in the $+z$ direction, and $e^{\gamma z}$ is the wave propagation in the $-z$ direction. Applying Eq. (2.5) to voltage of Eq. (2.10) gives the current on the line

$$I(z) = \frac{\gamma}{R + j\omega L}(V_0^+ e^{-\gamma z} - V_0^- e^{\gamma z}). \tag{2.12}$$

Comparison Eq. (2.12) with Eq. (2.11), impedance characteristic Z_0 can be defined as

$$Z_0 = \frac{V_0^+}{I_0^+} = \frac{-V_0^-}{I_0^-} = \frac{R + j\omega L}{\gamma} = \sqrt{\frac{R + j\omega L}{G + j\omega C}}. \tag{2.13}$$

The wave length on the line is

$$\lambda = \frac{2\pi}{\beta}, \tag{2.14}$$

and the phase velocity is

$$v_p = \frac{\omega}{\beta} = \frac{2\pi f}{\beta} = \lambda f. \tag{2.15}$$

The above solution includes loss effects, and it can be seen that the propagation constant and characteristic impedance are complex. In many practical cases, the loss of the line is very small and so can be neglected [18], resulting in a simplification of the results.

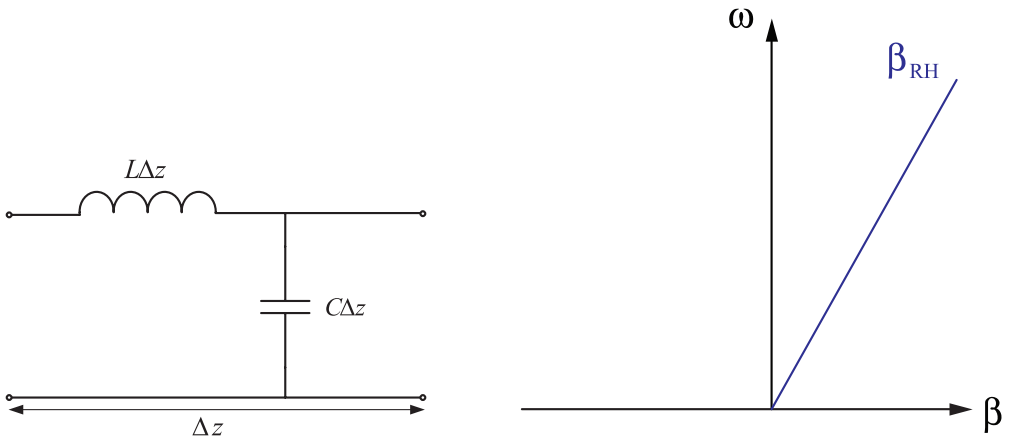

Figure 2.2: Purely RH TL (a) Equivalent circuit (b) Dispersion diagram.

Setting $R = G = 0$ in Eq. (2.9) gives the propagation constant as

$$\gamma = \alpha + j\beta = j\omega\sqrt{LC}, \tag{2.16}$$

or

$$\beta = \omega\sqrt{LC}, \tag{2.17}$$

$$\alpha = 0 \tag{2.18}$$

The conventional transmission line become purely RH transmission line as shown in Fig. 2.2.

2.1.3 Composite right/left handed transmission line

Metamaterials are effective homogeneous materials that under certain assumption can be modeled as a transmission line. To consider them as a homogeneous material the key assumption is that a effective homogeneous TL has an incremental length Δz and the following restriction has to be applied

$$\Delta z \ll \lambda_g \qquad (\text{at least} \quad \Delta z \leq \frac{\lambda_g}{4}), \tag{2.19}$$

where λ_g represents the guided wavelength.

As presented in [8], a purely left-handed transmission line (LH TL) as shown in Fig. 2.3 can not exist physically because parasitic series inductance and shunt capacitance effects, increasing with increasing frequency, will avoidably occur due to current flowing in the metallization and voltage gradients developing between the metal patterns of the trace and the ground plane. Therefore, the composite right/left-handed transmission line (CRLH TL) model is the most possible metmaterial transmission line structure.

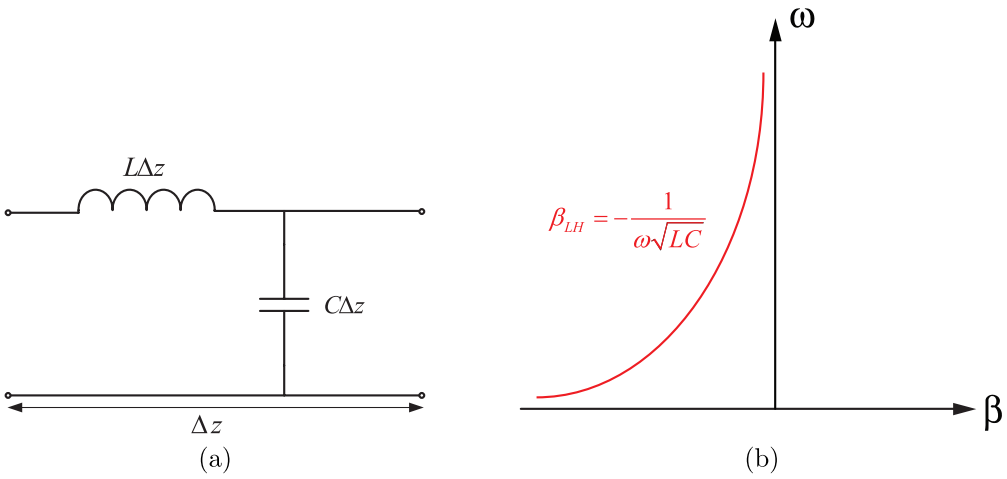

Figure 2.3: Purely LH TL (a) Equivalent circuit (b) Dispersion diagram.

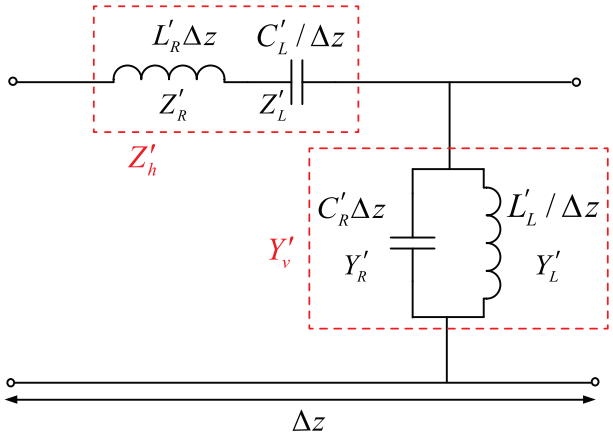

Figure 2.4: Equivalent circuit for a homogeneous CRLH TL [8].

The incremental model for a homogeneous CRLH TL is shown in Fig. 2.4. The model consists of a impedance per unit length Z'_h[Ω/m] constituted by a inductance RH per-unit-length L'_R[H/m] in series with a LH capacitance times-unit-length C'_L[F·m], and a admittance per unit length Y'_h[S/m] constituted by a capacitance RH per unit length C'_R[F/m] in parallel with a LH inductance times unit length L'_L[H·m]:

$$Z'_h = j\left(\omega L'_R - \frac{1}{\omega C'_L}\right), \tag{2.20}$$

$$Y'_v = j\left(\omega C'_R - \frac{1}{\omega L'_L}\right). \tag{2.21}$$

The fundamental characteristics of the CRLH TL has been presented in Ref. [8]. At low frequencies ($\omega \to 0$), $Z'_R \to 0$, $Y'_R \to 0$, so that the CRLH TL becomes equivalent to a purely LH TL. At high frequencies ($\omega \to \infty$), $Z'_L \to 0$, $Y'_L \to 0$, so that the CRLH TL becomes equivalent to a purely RH TL. At other frequencies, the TL characteristics

depend on the combination of LH and RH contributions. To further analysis of the CRLH TL, applying telegrapher equations for this case, one gets

$$\frac{dV}{dz} = -Z_h^{'} I = -j\left(\omega L_R^{'} - \frac{1}{\omega C_L^{'}}\right), \tag{2.22}$$

$$\frac{dI}{dz} = -Y_v^{'} I = -j\left(\omega C_R^{'} - \frac{1}{\omega L_L^{'}}\right). \tag{2.23}$$

Then by solving simultaneously two above equations and associated with the $+z/-z$ propagating traveling wave solutions, the wave equations for V and I of CRLH TL can be obtained as

$$V(z) = V_0^{+} e^{-\gamma z} + V_0^{-} e^{\gamma z}, \tag{2.24}$$

$$I(z) = I_0^{+} e^{-\gamma z} + I_0^{-} e^{\gamma z} = \frac{\gamma}{Z_h^{'}}(V_0^{+} e^{-\gamma z} - V_0^{-} e^{\gamma z}), \tag{2.25}$$

where

$$\gamma = \alpha + j\beta = \sqrt{Z_h^{'} Y_v^{'}}.$$

For convenience, the following variables are introduced

$$\omega_R^{'} = \frac{1}{\sqrt{L_R^{'} C_R^{'}}}, \tag{2.26}$$

$$\omega_L^{'} = \frac{1}{\sqrt{L_L^{'} C_L^{'}}}, \tag{2.27}$$

$$\kappa = L_R^{'} C_L^{'} + L_L^{'} C_R^{'}, \tag{2.28}$$

and the series and shunt resonance frequencies are

$$\omega_{se} = \frac{1}{\sqrt{L_R^{'} C_L^{'}}}, \tag{2.29}$$

$$\omega_{sh} = \frac{1}{\sqrt{L_L^{'} C_R^{'}}}, \tag{2.30}$$

respectively.
Now the complex propagation constant can be expressed as following

$$\gamma = \alpha + j\beta = \sqrt{Z_h^{'} Y_v^{'}} = j s(\omega) \sqrt{\left(\frac{\omega}{\omega_R^{'}}\right)^2 + \left(\frac{\omega_L^{'}}{\omega}\right)^2 - \kappa(\omega_L^{'})^2}, \tag{2.31}$$

where $s(\omega)$ is the sign function, $s(\omega) = -1$ if $\omega < \min(\omega_{se}, \omega_{sh})$ LH range, and $s(\omega) = +1$ if $\omega > \max(\omega_{se}, \omega_{sh})$ RH range. The propagation constant γ is purely imaginary $\gamma = j\beta$ in pass band and purely real $\gamma = \alpha$ in stop band at some ranges of frequency.

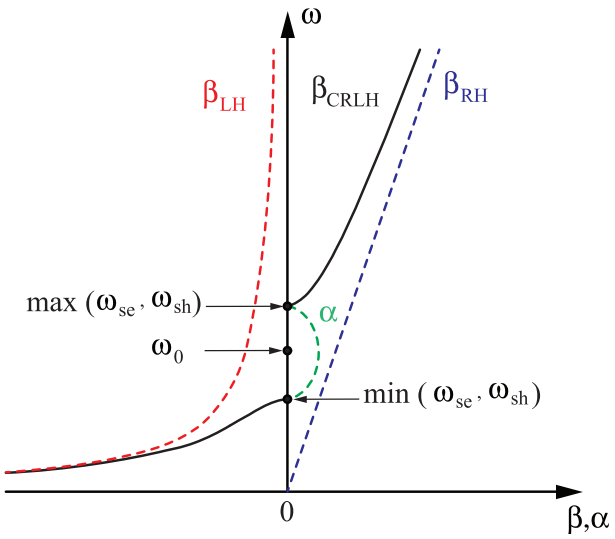

Figure 2.5: Dispersion diagram of a homogeneous CRLH TL

The sign function is explained by considering phase velocity ($v_p = \omega/\beta$) and group velocity ($v_g = d\omega/d\beta$). When $\omega < \min(\omega_{se}, \omega_{sh})$, the phase velocity and group velocity are anti-parallel since they have opposite signs meaning. There the TL is LH and β is negative. When $\omega > \max(\omega_{se}, \omega_{sh})$, the phase and group velocities are parallel since they have the same sign. The TL is RH and β is positive. A typical dispersion diagram of CRLH TL for propagation of energy v_g in the $+z$ direction is shown in Fig. 2.5.

The frequency of maximum attenuation ω_0 can be found by solving the following equation:

$$\frac{d\gamma}{d\omega} = js(\omega)\frac{\omega/\omega_R'^2 - \omega_L'^2/\omega^3}{\sqrt{(\omega/\omega_R')^2 + (\omega_L'/\omega)^2 - \kappa\omega_L'^2}} = 0, \tag{2.32}$$

yielding

$$\omega_0 = \sqrt{\omega_R'\omega_L'} = \sqrt{\omega_{se}\omega_{sh}} = \frac{1}{\sqrt[4]{L_R' L_L' C_R' C_L'}}. \tag{2.33}$$

The CRLH characteristic impedance is calculated from Eq. (2.25) as

$$Z_C = \frac{V_0^+}{I_0^+} = \frac{-V_0^-}{I_0^-} = \frac{Z_h'}{\gamma} = \sqrt{\frac{Z_h'}{Y_v'}} = \sqrt{\frac{L_L'}{C_L'}}\sqrt{\frac{(\omega/\omega_{se})^2 - 1}{(\omega/\omega_{sh})^2 - 1}}. \tag{2.34}$$

The other fundamental transmission line quantities, guided wavelength λ_g, phase velocity v_p, and group velocity v_g of the CRLH TL are derived from Eq. (2.31):

$$\lambda_g = \frac{2\pi}{|\beta|} = \frac{2\pi}{\sqrt{(\omega/\omega'_R)^2 + (\omega'_L/\omega)^2 - \kappa\omega'^2_L}}, \tag{2.35}$$

$$v_p = \frac{\omega}{\beta} = s(\omega)\frac{\omega}{\sqrt{(\omega/\omega'_R)^2 + (\omega'_L/\omega)^2 - \kappa\omega'^2_L}}, \tag{2.36}$$

$$v_g = \left(\frac{d\beta}{d\omega}\right)^{-1} = \frac{|\omega/\omega'^2_R - \omega'^2_L/\omega^3|}{\sqrt{(\omega/\omega'_R)^2 + (\omega'_L/\omega)^2 - \kappa\omega'^2_L}}. \tag{2.37}$$

Now we discuss interesting characteristics of the CRLH TL in a balanced case when the series and shunt resonant frequencies in Eqs. (2.29) and (2.30) are equal

$$\omega_{se} = \omega_{sh}, \tag{2.38}$$

or $L'_R C'_L = L'_L C'_R$. As a consequence, the gap closes up and the impedance characteristic becomes a frequency-independent quantity

$$Z_C = \sqrt{\frac{L'_L}{C'_L}} = \sqrt{\frac{L'_R}{C'_R}} = Z_L. \tag{2.39}$$

This means that the balanced condition allows matching over broad bandwidth. Since $\alpha = 0$, the simplified propagation constant β is purely real at all frequencies from $\omega = 0$ to $\omega = \infty$,

$$\beta = \frac{\omega}{\omega'_R} - \frac{\omega'_L}{\omega}, \tag{2.40}$$

exhibiting the root

$$\omega_0 = \sqrt{\omega'_R \omega'_L} = \omega_{se} = \omega_{sh}. \tag{2.41}$$

This indicates that the frequency of maximum attenuation of the unbalanced CRLH TL becomes transition frequency between LH and RH ranges if the TL is in balanced case.

Examples for the dispersion diagram of a homogeneous CRLH TL in an unbalanced and a balanced cases are shown in Figs. 2.6 and 2.7, respectively. While the impedance characteristics for these cases are plotted in Figs. 2.8 and 2.9. From Fig. 2.6, the unbalanced case has a stop band between 3.55 GHz and 5.03 GHz and $\alpha \neq 0$ in this band. For the balanced case, the gap of the stop band is closed in Fig. 2.7 and $\alpha = 0$. In addition, we have a constant impedance as expected in Fig. 2.9.

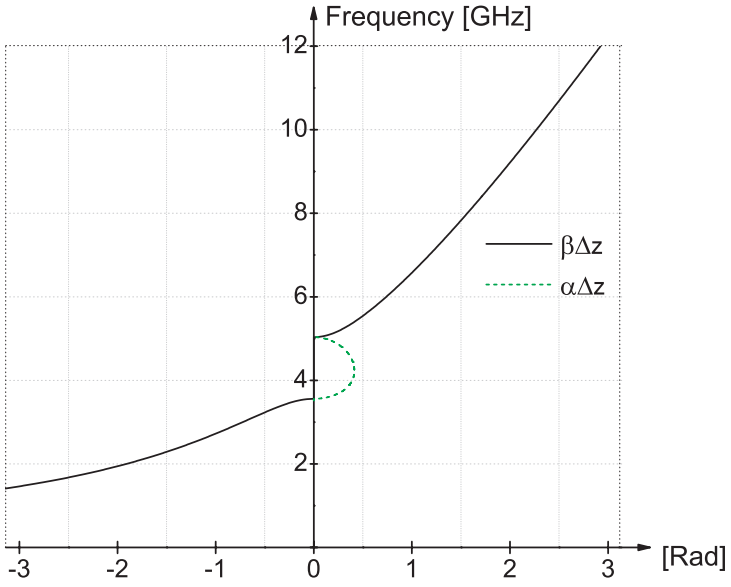

Figure 2.6: Dispersion diagram of a homogeneous CRLH TL in an unbalanced case with L'_R=2 nH/mm, C'_R=1 pF/mm, L'_L=1 nH·mm and C'_L=1 pF·mm

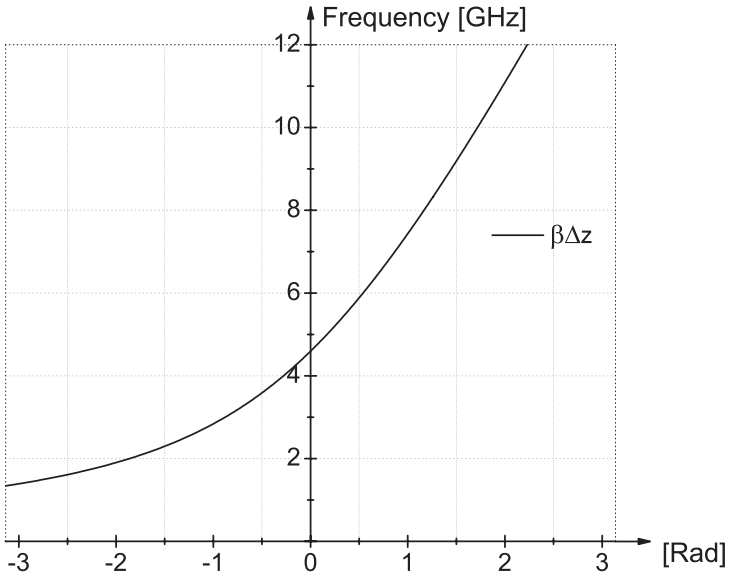

Figure 2.7: Dispersion diagram of a homogeneous CRLH TL in a balanced case with L'_R=1 nH/mm, C'_R=1.2 pF/mm, L'_L=1 nH·mm and C'_L=1.2 pF·mm

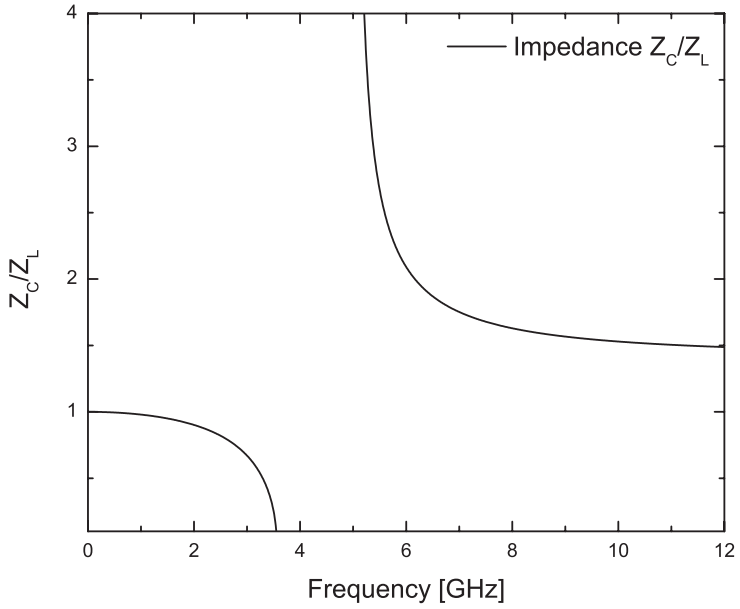

Figure 2.8: Impedance characteristic of a homogeneous CRLH TL in an unbalanced case with $L_R^{'}$=2 nH/mm, $C_R^{'}$=1 pF/mm, $L_L^{'}$=1 nH·mm and $C_L^{'}$=1 pF·mm

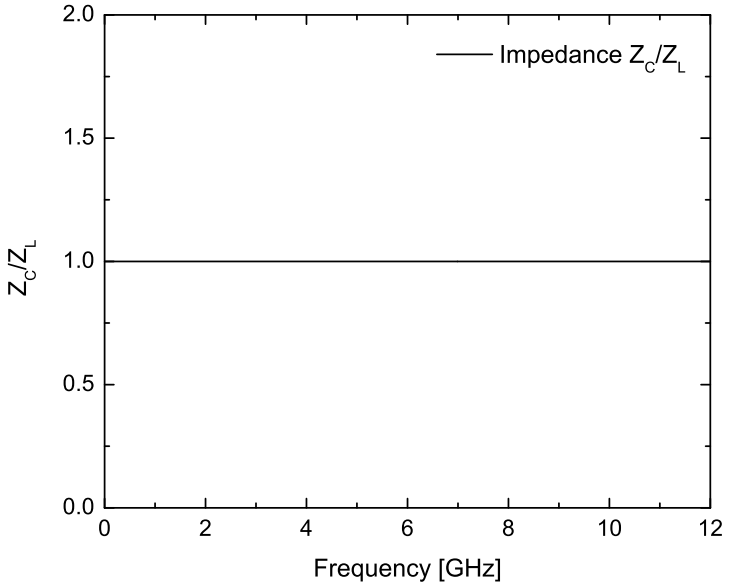

Figure 2.9: Impedance characteristic of a homogeneous CRLH TL in a balanced case with $L_R^{'}$=1 nH/mm, $C_R^{'}$=1.2 pF/mm, $L_L^{'}$=1 nH·mm and $C_L^{'}$=1.2 pF·mm

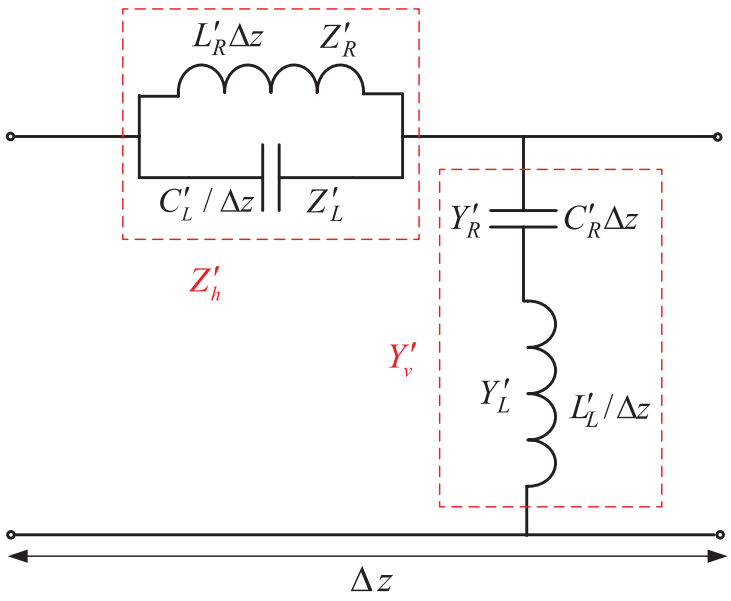

Figure 2.10: Equivalent circuit for a homogeneous dual-composite right/left handed transmission line (D-CRLH TL) [9]

2.1.4 Dual-composite right/left handed transmission line

The equivalent circuit model for a dual-composite right/left handed transmission line (D-CRLH TL) is shown in Fig. 2.10. The most fundamental property of the D-CRLH TL can be inferred from the observation with the impedances $Z'_R = j\omega L'_R$, $Z'_L = 1/(j\omega C'_L)$ and the admittance $Y'_R = j\omega C'_R$, $Y'_L = 1/(j\omega L'_L)$. From Ref. [9], at low frequencies $Z'_R \ll Z'_L$ and $Y'_R \ll Y'_L$ therefore the dominant components are L'_R and C'_R and the TL becomes equivalent to RH TL. At high frequencies, $Z'_R \gg Z'_L$ and $Y'_R \gg Y'_L$ therefore the dominant components are L'_L and C'_L and the TL becomes equivalent to LH TL.

The horizontal impedance Z'_h, the vertical admittance Y'_v, are obtained by

$$Z'_h = j\frac{\omega L'_R}{1-(\omega/\omega_{se})^2}, \tag{2.42}$$

$$Y'_v = j\frac{\omega C'_R}{1-(\omega/\omega_{sh})^2}, \tag{2.43}$$

where

$$\omega_{se} = \frac{1}{\sqrt{L'_R C'_L}}, \tag{2.44}$$

$$\omega_{sh} = \frac{1}{\sqrt{L'_L C'_R}}. \tag{2.45}$$

The complex propagation constant γ, and the characteristic impedance Z_C for a homogeneous D-CRLH TL are calculated as

$$\gamma = \alpha + j\beta = js(\omega)\frac{\omega\omega_L^{'}}{\sqrt{\omega^4 - (\omega_{se}^2 + \omega_{sh}^2)\omega^2 + \omega_{se}^2\omega_{sh}^2}}, \tag{2.46}$$

$$\omega_L^{'} = \frac{1}{\sqrt{L_L^{'}C_L^{'}}},$$

$$Z_C = \sqrt{\frac{Z_h^{'}}{Y_v^{'}}}$$

$$= \sqrt{\frac{L_R^{'}}{C_R^{'}}}\sqrt{\frac{1-(\omega/\omega_{sh})^2}{1-(\omega/\omega_{se})^2}} = Z_R\sqrt{\frac{1-(\omega/\omega_{sh})^2}{1-(\omega/\omega_{se})^2}}, \tag{2.47}$$

where $s(\omega)$ the sign function, $s(\omega) = -1$ at a high frequency LH range, and $s(\omega) = +1$ at a low frequency RH range.

The balanced case of the D-CRLH TL can be obtained when $\omega_{se} = \omega_{sh} = \omega_0$ or $L_R^{'}C_L^{'} = L_L^{'}C_R^{'}$. It leads to $\alpha = 0$ and the expression of the propagation constant β and the characteristic impedance Z_c simplify to

$$\beta = \frac{\omega\omega_L^{'}}{\omega_0^2 - \omega^2}, \tag{2.48}$$

$$Z_C = Z_R. \tag{2.49}$$

One can seen that β has a pole at the transition frequency ω_0 between the RH and LH bands.

Figures 2.11 and 2.13 show the dispersion diagram and the impedance characteristic of a homogeneous D-CRLH TL in an unbalanced with $L_R^{'}$=2 nH/mm, $C_R^{'}$=1 pF/mm, $L_L^{'}$=20 nH·mm and $C_L^{'}$=2 pF·mm, respectively. As inference from the beginning of this section, D-CRLH TL exhibits a LH band at high frequencies, a RH band at low frequencies in Fig. 2.11. This is opposite to the CRLH TL behavior. The value of α at the stop-band between the LH and RH band is is higher than the CRLH TL. Figures 2.12 and 2.14 show the dispersion diagram and the impedance characteristic of a homogeneous D-CRLH TL in a balanced case with $L_R^{'}$=2 nH/mm, $C_R^{'}$=1 pF/mm, $L_L^{'}$=2 nH·mm and $C_L^{'}$=1 pF·mm. In this case, the stop-band between the RH and LH band is not delimited and this is in contrast with the balanced case of the CRLH TL. Similarly, we have $\alpha = 0$ and a constant impedance which allows a broadband matching.

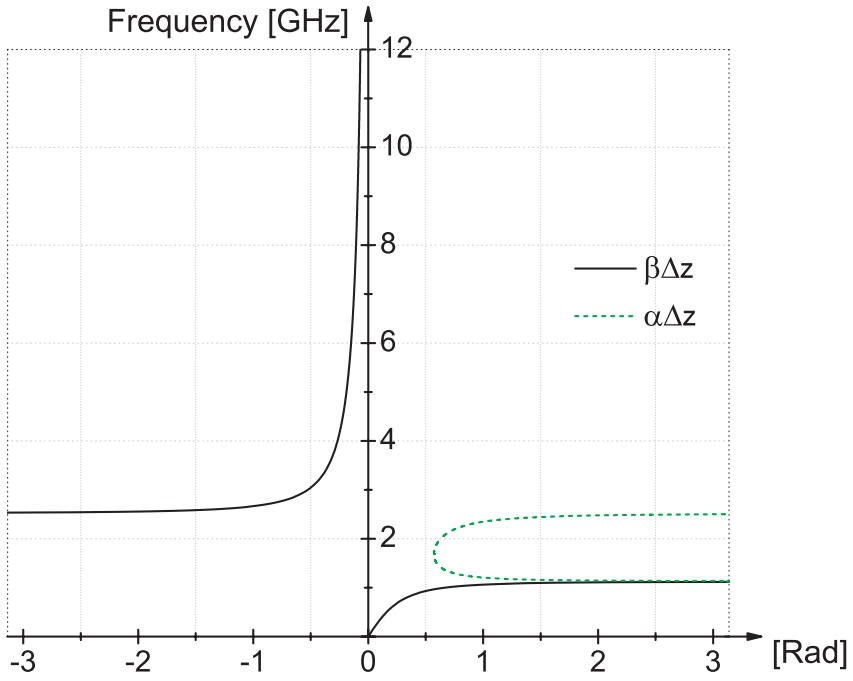

Figure 2.11: Dispersion diagram of a homogeneous D-CRLH TL in an unbalanced case with L'_R=2 nH/mm, C'_R=1 pF/mm, L'_L=20 nH·mm and C'_L=2 pF·mm

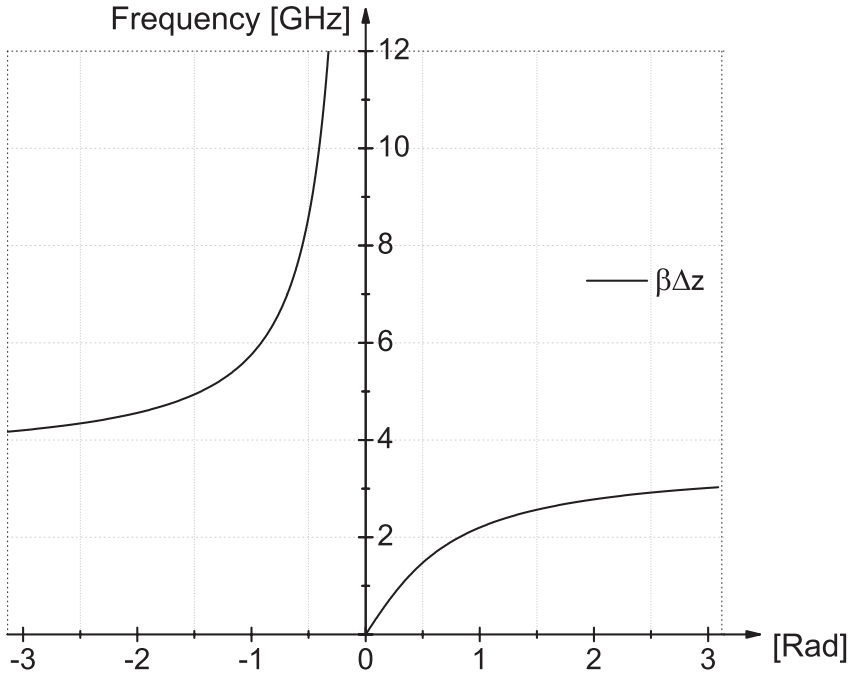

Figure 2.12: Dispersion diagram of a homogeneous D-CRLH TL in a balanced case with L'_R=2 nH/mm, C'_R=1 pF/mm, L'_L=2 nH·mm and C'_L=1 pF·mm

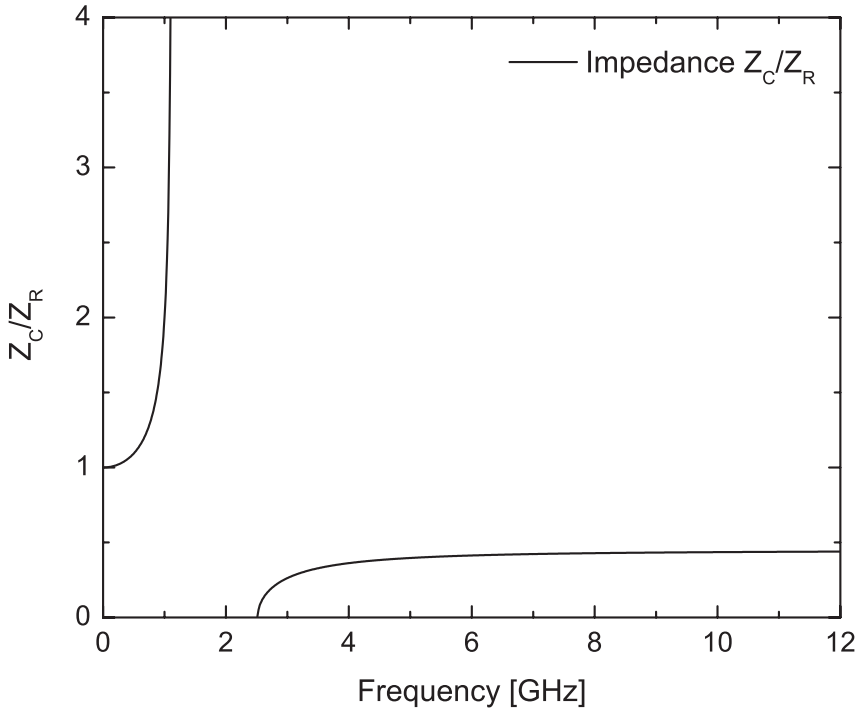

Figure 2.13: Impedance characteristic of a homogeneous D-CRLH TL in an unbalanced case with $L_R^{'}$=2 nH/mm, $C_R^{'}$=1 pF/mm, $L_L^{'}$=20 nH·mm and $C_L^{'}$=2 pF·mm

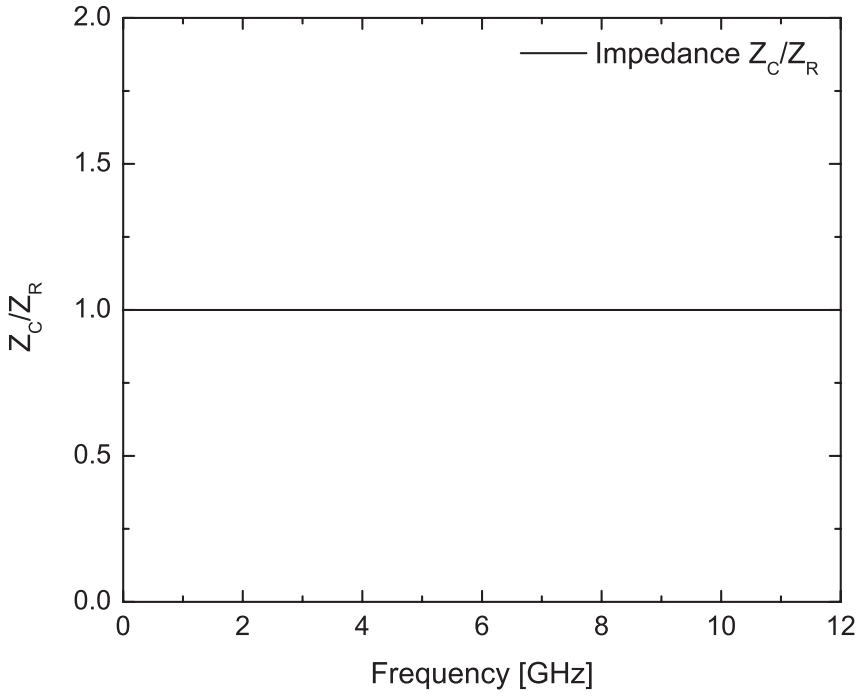

Figure 2.14: Impedance characteristic of a homogeneous D-CRLH TL in a balanced case with $L_R^{'}$=2 nH/mm, $C_R^{'}$=1 pF/mm, $L_L^{'}$=2 nH·mm and $C_L^{'}$=1 pF·mm

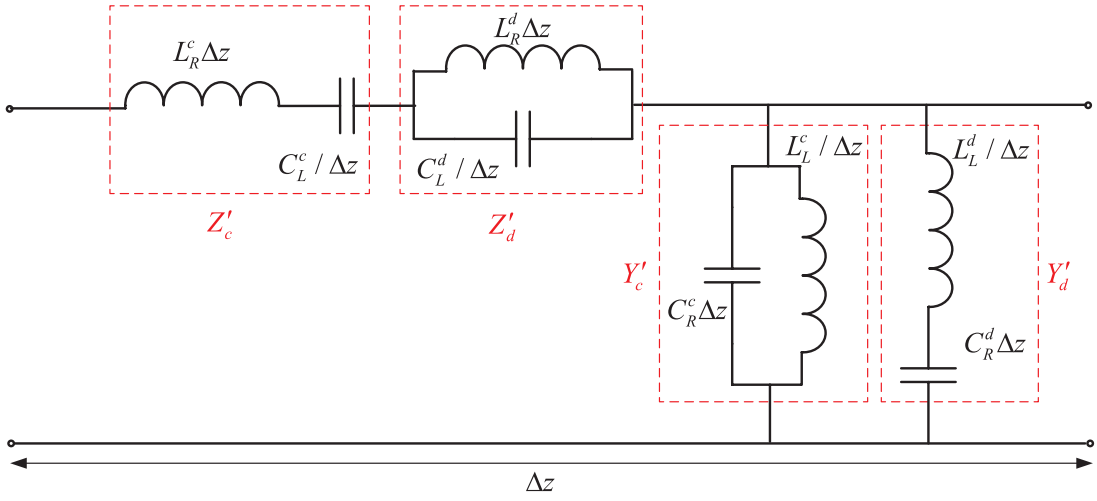

Figure 2.15: Equivalent circuit for a homogeneous extended-composite right/left handed transmission line (E-CRLH TL) [10]

2.1.5 Extended-composite right/left handed transmission line

Figure 2.15 shows the incremental circuit model of a homogeneous extended-composite right/left handed transmission tine (E-CRLH TL) which is combined from the CRLH and the D-CRLH TLs [10]. The superscripts "c" and "d" stands for the CRLH and D-CRLH TLs, respectively. The impedance $Z_h^{'}$ of the horizontal branch and the admittance $Y_v^{'}$ of the vertical branch are given by

$$Z_h^{'} = Z_c^{'} + Z_d^{'} = j\omega L_R^c \left[1 - \left(\frac{\omega_{se}^c}{\omega}\right)^2\right] + \frac{j\omega L_R^d}{1-(\omega/\omega_{se}^d)^2}, \tag{2.50}$$

$$\omega_{se}^c = \frac{1}{\sqrt{L_R^c C_L^c}}, \quad \omega_{se}^d = \frac{1}{\sqrt{L_R^d C_L^d}}, \tag{2.51}$$

$$Y_v^{'} = Y_c^{'} + Y_d^{'} = j\omega C_R^c \left[1 - \left(\frac{\omega_{sh}^c}{\omega}\right)^2\right] + \frac{j\omega C_R^d}{1-(\omega/\omega_{sh}^d)^2}, \tag{2.52}$$

$$\omega_{sh}^c = \frac{1}{\sqrt{L_L^c C_R^c}}, \quad \omega_{se}^d = \frac{1}{\sqrt{L_L^d C_R^d}}. \tag{2.53}$$

The complex propagation constant γ, and the characteristic impedance Z_C for the E-CRLH TL are obtained by

$$\gamma = \alpha + j\beta = \sqrt{(Z_c^{'} + Z_d^{'})(Y_c^{'} + Y_d^{'})}, \tag{2.54}$$

$$Z_C = \sqrt{\frac{Z_c^{'} + Z_d^{'}}{Y_c^{'} + Y_d^{'}}}. \tag{2.55}$$

The balanced condition for the E-CRLH TL is

$$\omega_{se}^{c} = \omega_{sh}^{c}, \tag{2.56}$$

$$\omega_{se}^{d} = \omega_{sh}^{d}, \tag{2.57}$$

$$\frac{L_R^d}{L_R^c} = \frac{C_R^d}{C_R^c}. \tag{2.58}$$

If this condition is fulfilled, $\alpha = 0$ and Equation (2.54) reduces to purely real expression

$$\beta = \frac{\omega^2 - \omega_0^2}{\omega\omega_R^c} - \frac{\omega\omega_L^d}{\omega^2 - \omega_0^2}, \tag{2.59}$$

where

$$\omega_R^c = \frac{1}{\sqrt{L_R^c C_R^c}}, \tag{2.60}$$

$$\omega_L^d = \frac{1}{\sqrt{L_L^d C_L^d}}, \tag{2.61}$$

$$\omega_0 = \frac{1}{\sqrt{L_R^c C_L^c}} = \frac{1}{\sqrt{L_R^d C_L^d}} = \frac{1}{\sqrt{L_L^c C_R^c}} = \frac{1}{\sqrt{L_L^d C_R^d}}. \tag{2.62}$$

The characteristic impedance Z_C is purely real and frequency independent,

$$Z_C = \sqrt{\frac{L_R^c}{C_R^c}} = \sqrt{\frac{L_L^c}{C_L^c}} = \sqrt{\frac{L_R^d}{C_R^d}} = \sqrt{\frac{L_L^d}{C_L^d}} = Z_R. \tag{2.63}$$

The two balanced transition frequencies $\omega_{01,02}$ can be calculated by setting Eq. (2.59) to zero, which yields

$$\omega_{01,02} = \sqrt{\omega_0^2 + \frac{\omega_R^c \omega_L^d}{4}} \pm \sqrt{\frac{\omega_R^c \omega_L^d}{4}}, \tag{2.64}$$

$$\sqrt{\omega_{01}\omega_{02}} = \omega_0. \tag{2.65}$$

Firgures 2.16 and 2.17 show the dispersion diagram of a homogeneous E-CRLH TL in an unbalanced and a balanced cases, respectively. While the impedance characteristic of these cases are shown in Figs. 2.18 and 2.19. The E-CRLH TL exhibits a richer behavior, with two LH bands and two RH bands to compare with the CRLH and D-CRLH TLs. At the unbalanced case, we have four pass-bands and three stop-bands. For instance, this case can be applied to design multiband applications. At the balanced case, there is an unavoidable intermediate gap due to the stop-band nature of the D-CRLH TL in Section 2.1.4. The impedance is also purely real and frequency independent. Therefore, we can impedance matching at a broadband.

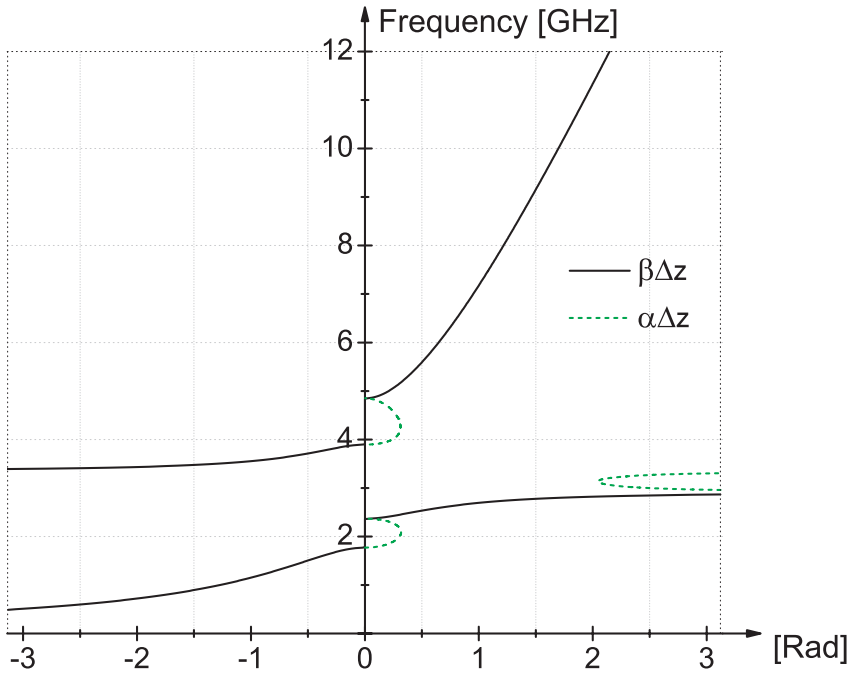

Figure 2.16: Dispersion diagram of a homogeneous E-CRLH TL in an unbalanced case with L_R^c=2 nH/mm, C_L^c=3 pF·mm, L_R^d=0.5 nH/mm, C_L^d=4.5 pF·mm, L_L^c=3.25 nH·mm, C_R^c=0.5 pF/mm, L_L^d=10 pF·mm, and c_R^d=0.3 pF/mm

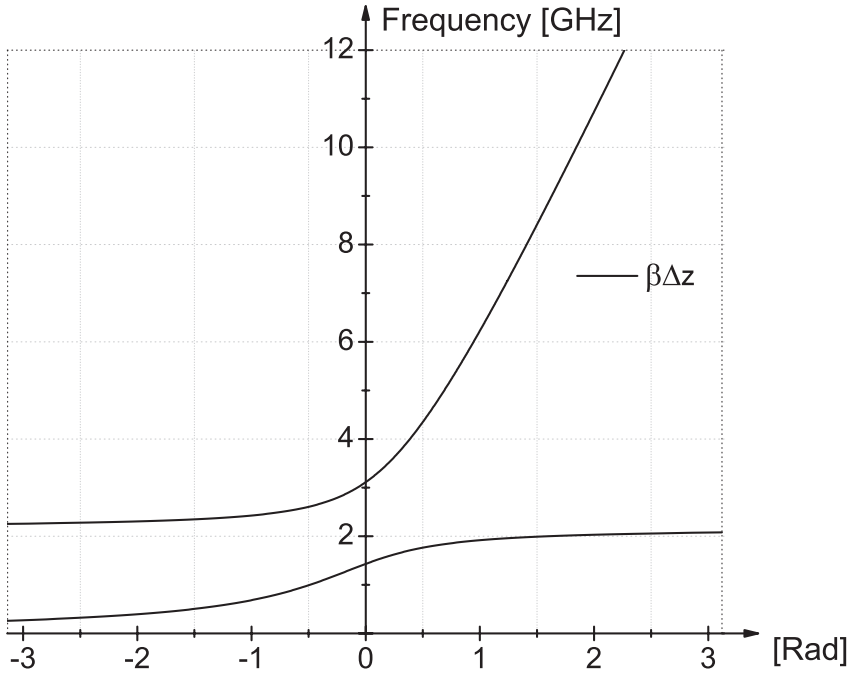

Figure 2.17: Dispersion diagram of a homogeneous E-CRLH TL in a balanced case with L_R^c=2 nH/mm, C_L^c=3 pF·mm, L_R^d=1.2 nH/mm, C_L^d=4.5 pF·mm, L_L^c=12 nH·mm, C_R^c=0.5 pF/mm, L_L^d=18 pF·mm, and c_R^d=0.3 pF/mm

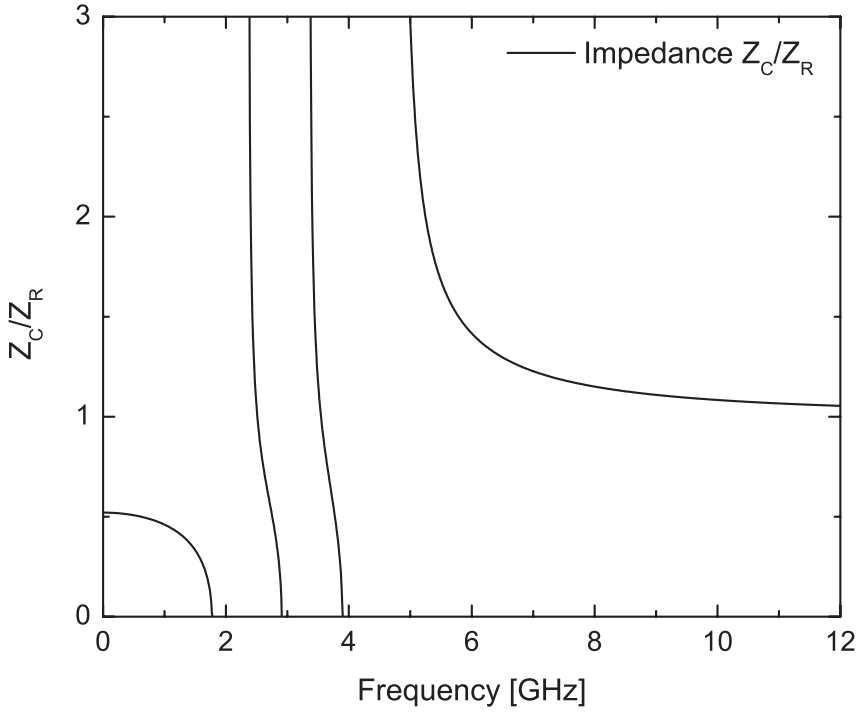

Figure 2.18: Dispersion diagram of a homogeneous E-CRLH TL in an unbalanced case with L_R^c=2 nH/mm, C_L^c=3 pF·mm, L_R^d=0.5 nH/mm, C_L^d=4.5 pF·mm, L_L^c=3.25 nH·mm, C_R^c=0.5 pF/mm, L_L^d=10 pF·mm, and c_R^d=0.3 pF/mm

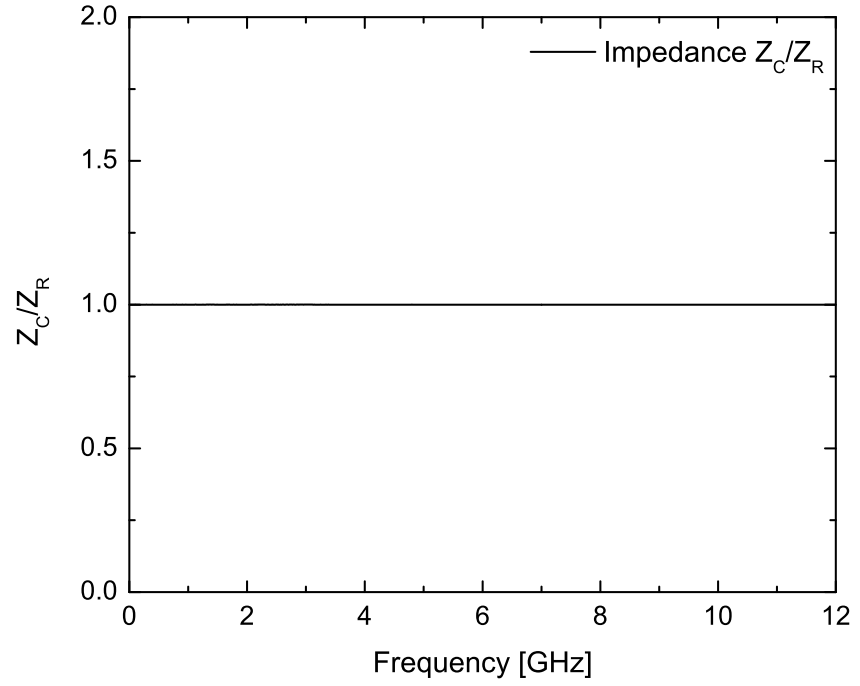

Figure 2.19: Dispersion diagram of a homogeneous E-CRLH TL in a balanced case with L_R^c=2 nH/mm, C_L^c=3 pF·mm, L_R^d=1.2 nH/mm, C_L^d=4.5 pF·mm, L_L^c=12 nH·mm, C_R^c=0.5 pF/mm, L_L^d=18 pF·mm, and c_R^d=0.3 pF/mm

2.1.6 Periodic L–C loaded unit cell networks

Previously, the metamaterial transmission lines (CRLH, D-CRLH and E-CRLH TLs) were mapped to the circuit expressions obtained from Kirchhoff's laws in order to show its general characteristics and to confirm backward propagation waves. However, this approach may not be realized. Any practical implementation of these metamaterial transmission lines must be periodic L–C loaded unit cell network. As the circuit theory, the physical dimensions of the unit cells need to be much smaller than the wavelength, such that each section can be considered as a lumped-element equivalent circuit. When the circuit model with finite-dimension is periodically cascaded, a band structure is considerably developed on the corresponding dispersion relation by conducting periodic Bloch-Floquet analysis which is the standard procedure for 1-D periodic of microwave networks.

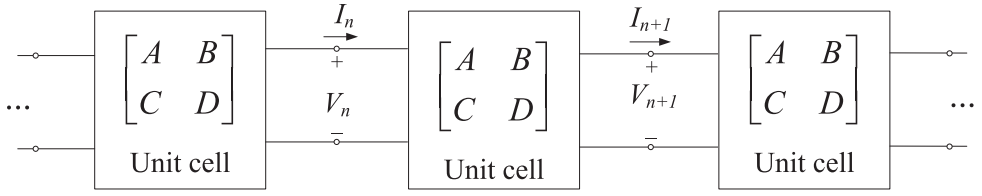

Figure 2.20: Periodically unit cell network

According to the periodic Bloch-Floquet theorem with a forward propagation in z direction as shown in Fig. 2.20, the voltage and current at the terminal (n) unit cell are related to the voltage and current at the terminal $(n+1)$ unit cell by propagation $e^{-\gamma d}$. Thus

$$V_{n+1} = V_n e^{-\gamma d}, \tag{2.66}$$

$$I_{n+1} = I_n e^{-\gamma d}. \tag{2.67}$$

Using the ABCD matrix, one gets

$$\begin{bmatrix} V_n \\ I_n \end{bmatrix} = \begin{bmatrix} A & B \\ C & D \end{bmatrix} \times \begin{bmatrix} V_{n+1} \\ I_{n+1} \end{bmatrix}. \tag{2.68}$$

Then, from Eqs. (2.66),(2.67) and (2.68), we have

$$\begin{bmatrix} V_{n+1}e^{\gamma d} \\ I_{n+1}e^{\gamma d} \end{bmatrix} = \begin{bmatrix} A & B \\ C & D \end{bmatrix} \begin{bmatrix} V_{n+1} \\ I_{n+1} \end{bmatrix}. \tag{2.69}$$

or

$$\begin{bmatrix} A - e^{-\gamma d} & B \\ C & D - e^{-\gamma d} \end{bmatrix} \begin{bmatrix} V_{n+1} \\ I_{n+1} \end{bmatrix} = 0. \tag{2.70}$$

For a nontrivial solution, the determinant of the above matrix must vanish:

$$AD - BC + e^{j2\gamma d} - (A + D)e^{j\gamma d} = 0. \tag{2.71}$$

In addition, $AD - BC = 1$ as required for reciprocal networks

$$1 + e^{j2\gamma d} - (A + D)e^{j\gamma d} = 0 \tag{2.72}$$

$$\Rightarrow e^{-\gamma d} + e^{-\gamma d} = A + D \tag{2.73}$$

$$\Rightarrow \cosh \gamma d = \frac{A + D}{2}. \tag{2.74}$$

If $\gamma = \alpha + j\beta$, we have

$$\cosh \alpha d \cos \beta d + j \sinh \alpha d \sin \beta d = \frac{A + D}{2}, \tag{2.75}$$

As presented in [18], the right hand side of Equation 2.75 purely real, we must have either $\alpha = 0$ or $\beta = 0$. For the case $\alpha \neq 0$ and $\beta = 0/\pi$, the wave is attenuated along the line, this defines the stop band of the structure. For the case $\alpha = 0$ and $\beta \neq 0$, this case corresponds to a nonattenuated propagating wave on the periodic structure, and defines the pass band of the structure. Equation (2.75) reduces to

$$\cos \beta d = \frac{A + D}{2}, \tag{2.76}$$

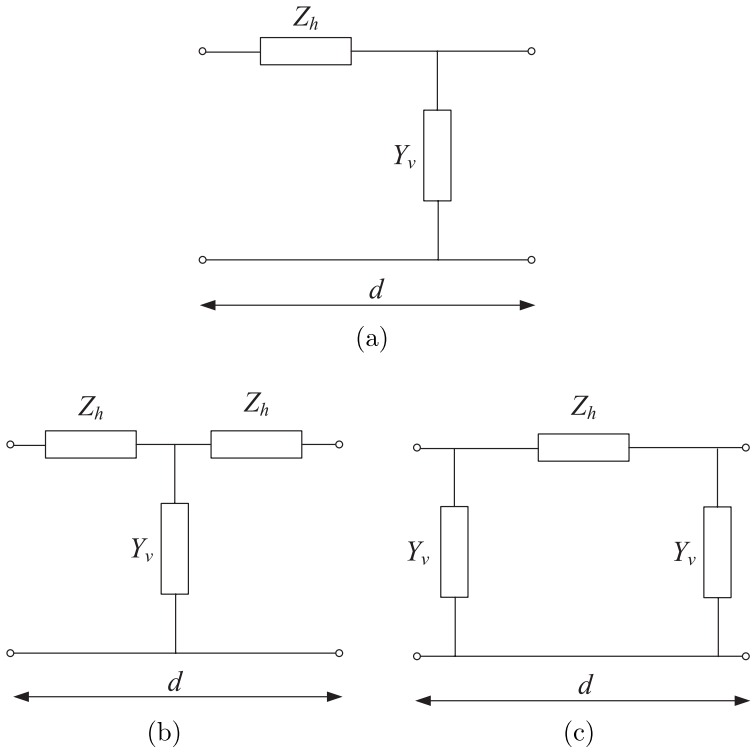

Figure 2.21: (a) Asymmetric, (b) Symmetric T-shape, (c) Symmetric π-shape

ABCD matrixes for asymmetric, symmetric T-shape and symmetric π-shape unit cells are calculated from the following equations:

$$\begin{aligned}\begin{bmatrix} A & B \\ C & D \end{bmatrix}_{\text{asymmetric}} &= \begin{bmatrix} 1 & Z_h \\ 0 & 1 \end{bmatrix} \begin{bmatrix} 1 & 0 \\ Y_v & 1 \end{bmatrix} \\ &= \begin{bmatrix} 1 + Z_h Y_v & Z_h \\ Y_v & 1 \end{bmatrix}, \end{aligned} \tag{2.77}$$

$$\begin{aligned}\begin{bmatrix} A & B \\ C & D \end{bmatrix}_{\text{symmetric T-shape}} &= \begin{bmatrix} 1 & Z_h \\ 0 & 1 \end{bmatrix} \begin{bmatrix} 1 & 0 \\ Y_v & 1 \end{bmatrix} \begin{bmatrix} 1 & Z_h \\ 0 & 1 \end{bmatrix} \\ &= \begin{bmatrix} 1 + Z_h Y_v & 2Z_h + Z_h^2 Y_v \\ Y_v & 1 + Z_h Y_v \end{bmatrix}, \end{aligned} \tag{2.78}$$

$$\begin{aligned}\begin{bmatrix} A & B \\ C & D \end{bmatrix}_{\text{symmetric } \pi\text{-shape}} &= \begin{bmatrix} 1 & 0 \\ Y_v & 1 \end{bmatrix} \begin{bmatrix} 1 & Z_h \\ 0 & 1 \end{bmatrix} \begin{bmatrix} 1 & 0 \\ Y_v & 1 \end{bmatrix} \\ &= \begin{bmatrix} 1 + Z_h Y_v & Z_h \\ 2Y_v + Z_h Y_v^2 & 1 + Z_h Y_v \end{bmatrix}. \end{aligned} \tag{2.79}$$

Therefore, the dispersion relations from Eq. (2.76) can be obtained as

$$\cos \beta d = 1 + \frac{Z_h Y_v}{2} \quad \text{for asymmetric unit cell,} \tag{2.80}$$

$$\cos \beta d = 1 + Z_h Y_v \quad \text{for symmetric T-shape unit cell,} \tag{2.81}$$

$$\cos \beta d = 1 + Z_h Y_v \quad \text{for asymmetric } \pi\text{-shape unit cell.} \tag{2.82}$$

Alternatively, the metamaterial transmission lines can be modeled as a general asymmetric, symmetric T-shape and π-shape as shown in Figs. 2.21 (a), (b) and (c), respectively. Now we apply the analysis of periodic L–C loaded unit cell networks for the asymmetric unit cells of the CRLH, D-CRLH and E-CRLH TLs in Figs. 2.4, 2.10 and 2.15, respectively. The dispersion relations of these TL are calculated for its balanced cases which the values of L–C elements are similar with Figs. 2.7, 2.12, 2.17.

Then the comparison of propagation constant β between the homogeneous transmission lines by incremental circuit analysis and the periodic L–C loaded unit cell networks by the Bloch-Floquet analysis is shown in Fig. 2.22. In the same manner, the incremental transmission line model approached by Telegrapher's equations exhibit a continuous dispersion at high and low frequencies. This imply that there are no cut-off frequencies at $\beta = \pi$. However, the lumped-element periodic unit cell approached by Bloch-Floquet analysis exhibit cut-off frequencies at $\beta = \pi$.

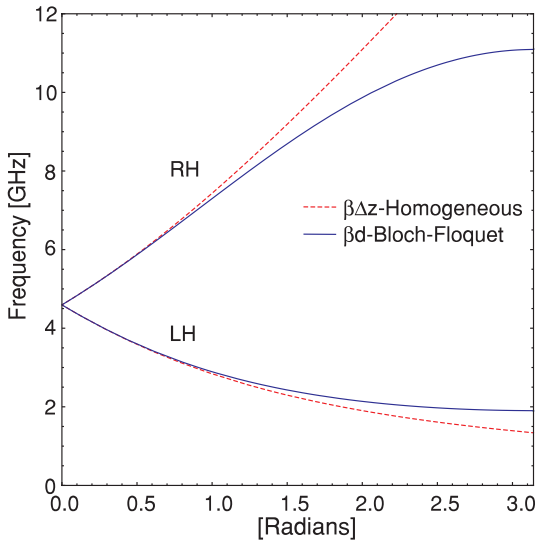

(a)

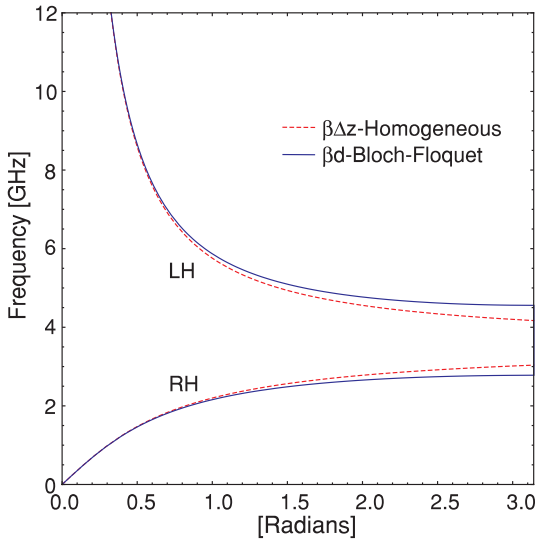

(b)

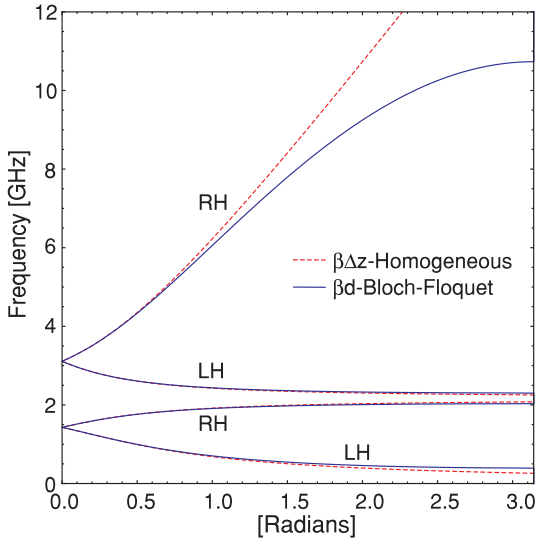

(c)

Figure 2.22: Comparison between the homogeneous TLs and Bloch-Floquet analysis (a) CRLH TL in Fig. 2.7, (b) D-CRLH TL in Fig 2.12, (c) E-CRLH TL in Fig. 2.17.

2.2 Analysis and design of E-CRLH TL with new closed-form solutions

2.2.1 Introduction

Most microwave application design with the E-CRLH TL are based on the controllability of the dispersion diagram, and the impedance matching consideration of the Bloch impedance. Therefore, it is important to find appropriate L–C elements to match the requirements. Previous studies for designing E-CRLH TL have presented for balanced cases and have seldom mentioned about unbalanced cases. Reference [19] presented a possible solution for a balanced case to achieve a desired phase at four specified frequencies. A balanced E-CRLH TL with arbitrary phase shifts at four arbitrary frequencies is reported in Ref. [20] by using the results of homogeneous E-CRLH medium. Homogeneous E-CRLH medium may be useful for idealization, but not for the case of a practical E-CRLH TL lumped implementation, since the unit-cells would sometimes cascaded periodically to build effectively the corresponding uniform TL structure [10].

This section shows a novel procedure for analysis and design of the E-CRLH TL in unbalanced, balanced, mixed and special cases. By solving a set of equations explicitly, one can design easily a desired dispersion diagram and control the Bloch impedance. In addition, scattering parameters of a periodic E-CRLH TL unit-cells network have been investigated carefully to show a complete view about the applicability of E-CRLH TLs.

2.2.2 E-CRLH TL analysis

The equivalent circuit of an E-CRLH TL unit cell [10, 11] is shown in Fig. 2.23. For convenience, we use numbering subscripts $(1, 2, 3, 4)$ for L–C elements. In the horizontal branch, a series L_1–C_1 resonator connects in series with a parallel L_2–C_2 resonator. The vertical branch contains a parallel L_3–C_3 resonator in shunt with a series L_4–C_4 resonator.

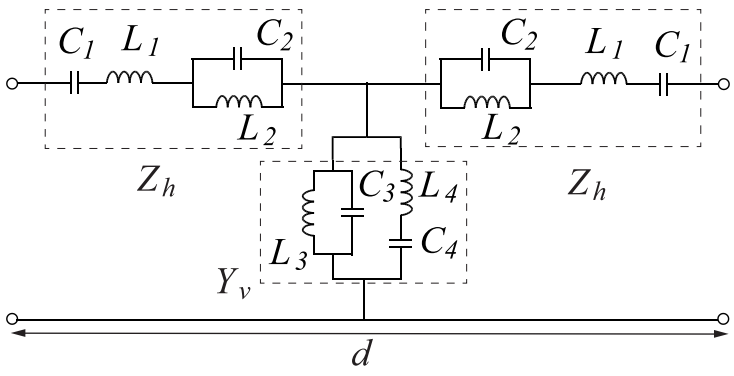

Figure 2.23: Equivalent circuit of an E-CRLH TL unit cell [10, 11].

From this equivalent circuit model, the fundamental characteristics of this transmission line are straight forwardly analyzed by a standard TL and circuit theories. The impedance Z_h of the horizontal branch and the admittance Y_v of the vertical branch are given respectively by

$$Z_h = \frac{jL_1(\omega^2 - \omega_{Z01}^2)(\omega^2 - \omega_{Z02}^2)}{\omega(\omega^2 - \omega_{Z\infty}^2)}, \tag{2.83}$$

$$Y_v = \frac{jC_3(\omega^2 - \omega_{Y01}^2)(\omega^2 - \omega_{Y02}^2)}{\omega(\omega^2 - \omega_{Y\infty}^2)}, \tag{2.84}$$

where

$$\omega_{Z\infty}^2 = \frac{1}{L_2C_2},\ \omega_{Y\infty}^2 = \frac{1}{L_4C_4}, \tag{2.85}$$

$$\omega_{Z01}^2 = \frac{B_1 + \sqrt{B_1^2 - 4A_1}}{2},\ \omega_{Z02}^2 = \frac{B_1 - \sqrt{B_1^2 - 4A_1}}{2}, \tag{2.86}$$

$$\omega_{Y01}^2 = \frac{B_2 + \sqrt{B_2^2 - 4A_2}}{2},\ \omega_{Y02}^2 = \frac{B_2 - \sqrt{B_2^2 - 4A_2}}{2}, \tag{2.87}$$

$$A_1 = \frac{1}{L_1C_1L_2C_2},\ B_1 = \frac{1}{L_1C_1} + \frac{1}{L_2C_2} + \frac{1}{L_1C_2}, \tag{2.88}$$

$$A_2 = \frac{1}{L_3C_3L_4C_4},\ B_2 = \frac{1}{L_3C_3} + \frac{1}{L_4C_4} + \frac{1}{L_4C_3}. \tag{2.89}$$

By using the results for the T-shape unit cell in Section 2.1.6, the dispersion relation is obtained as

$$\cos(\beta d) = 1 + Z_hY_v, \tag{2.90}$$

where β is the propagation constant for the Bloch waves and d is the length of the unit cell. The possible bands of the E-CRLH TL are shown by the dispersion diagram, which can be plotted from Eq. (2.90). An example of the dispersion diagram of the unbalanced E-CRLH TL is depicted in Fig. 2.24. The dispersion diagram shows two RH bands (f_{C8}, f_{C4}), (f_{C6}, f_{C2}), two LH bands (f_{C1}, f_{C5}), (f_{C3}, f_{C7}). The balanced E-CRLH TL is obtained when $f_{C5} = f_{C6}$ and $f_{C7} = f_{C8}$. The cut-off frequencies f_{C1}~f_{C8} are calculated from the conditions: $\cos(\beta d) = \pm 1$.

The Bloch impedance is a quantity to use for the impedance matching. The Bloch impedance of the proposed metamaterial transmission line may be approximately calculated by the expression [11], [21]:

$$Z_B = \sqrt{\frac{2Z_h}{Y_v}} = \sqrt{\frac{2L_1(\omega^2 - \omega_{Z01}^2)(\omega^2 - \omega_{Z02}^2)(\omega^2 - \omega_{Y\infty}^2)}{C_3(\omega^2 - \omega_{Y01}^2)(\omega^2 - \omega_{Y02}^2)(\omega^2 - \omega_{Z\infty}^2)}}. \tag{2.91}$$

In this study, a different approach is proposed to determine lumped elements of the equivalent circuit. Required L–C elements of the E-CRLH TL unit cell are calculated

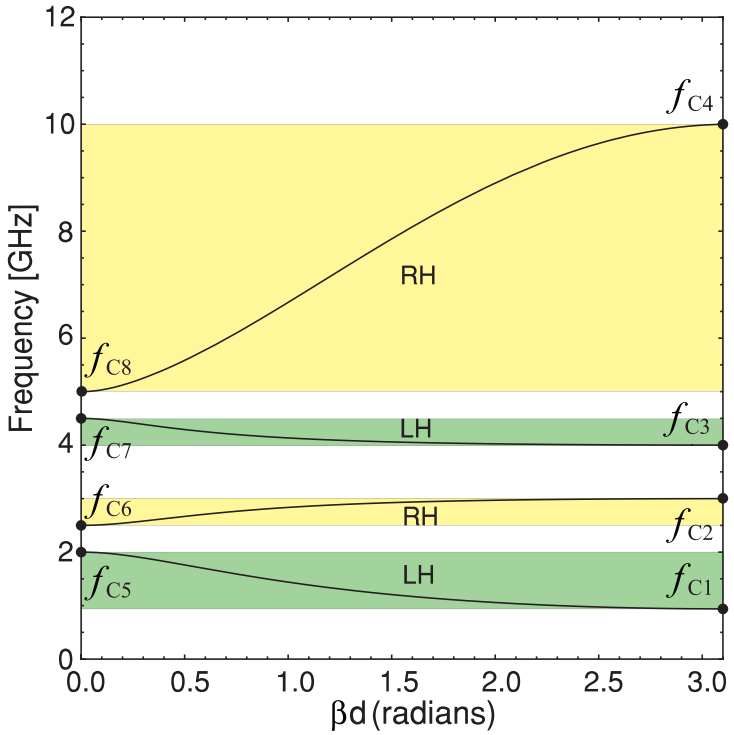

Figure 2.24: A typical dispersion diagram of E-CRLH TL in an unbalanced case.

from the cut-off frequencies f_{C1}~f_{C8} of a desired dispersion diagram. So the proposed procedure can be used for both an unbalanced case and a balanced case.

Let us begin from a general unbalanced case. From the condition $\cos(\beta d) = 1$, Eq. (2.90) becomes $Z_h Y_v = 0$, then the cut-off frequencies f_{C5}~f_{C8} are determined from ω_{Z01}, ω_{Z02}, ω_{Y01}, ω_{Y02}. Accordingly, six cases are available:

$$\omega_{Z02} \leq \omega_{Y02} < \omega_{Z01} \leq \omega_{Y01}, \tag{2.92}$$

$$\omega_{Z02} \leq \omega_{Z01} < \omega_{Y02} \leq \omega_{Y01}, \tag{2.93}$$

$$\omega_{Z02} \leq \omega_{Y02} < \omega_{Y01} \leq \omega_{Z01}, \tag{2.94}$$

$$\omega_{Y02} \leq \omega_{Z02} < \omega_{Y01} \leq \omega_{Z01}, \tag{2.95}$$

$$\omega_{Y02} \leq \omega_{Y01} < \omega_{Z02} \leq \omega_{Z01}, \tag{2.96}$$

$$\omega_{Y02} \leq \omega_{Z02} < \omega_{Z01} \leq \omega_{Y01}, \tag{2.97}$$

provided $\Delta_1 = B_1^2 - 4A_1 \geq 0$, and $\Delta_2 = B_2^2 - 4A_2 \geq 0$.
From the condition $\cos(\beta d) = -1$, the cut-off frequencies f_{C1}~f_{C4} are calculated from:

$$Z_h Y_v + 2 = 0, \tag{2.98}$$

which is a fourth order equation with respect to ω^2, and has four roots $(\omega_{C1}^2, \omega_{C2}^2, \omega_{C3}^2, \omega_{C4}^2)$.

From the relation between these roots and the coefficients of Eq. (2.98), one gets:

$$\omega_{Z01}^2\omega_{Z02}^2\omega_{Y01}^2\omega_{Y02}^2 = \omega_{C1}^2\omega_{C2}^2\omega_{C3}^2\omega_{C4}^2, \tag{2.99}$$

$$\omega_{Z01}^2 + \omega_{Z02}^2 + \omega_{Y01}^2 + \omega_{Y02}^2 + \frac{2}{L_1C_3} = \omega_{C1}^2 + \omega_{C2}^2 + \omega_{C3}^2 + \omega_{C4}^2, \tag{2.100}$$

$$\begin{aligned}&\omega_{Z01}^2\omega_{Z02}^2 + \omega_{Y01}^2\omega_{Y02}^2 + (\omega_{Z01}^2 + \omega_{Z02}^2)(\omega_{Y01}^2 + \omega_{Y02}^2) + \frac{2}{L_1C_3}(\omega_{Z\infty}^2 + \omega_{Y\infty}^2)\\ &\quad = \omega_{C1}^2\omega_{C2}^2 + \omega_{C2}^2\omega_{C3}^2 + \omega_{C3}^2\omega_{C4}^2 + \omega_{C4}^2\omega_{C1}^2 + \omega_{C4}^2\omega_{C2}^2 + \omega_{C1}^2\omega_{C3}^2,\end{aligned} \tag{2.101}$$

$$\begin{aligned}&(\omega_{Z01}^2 + \omega_{Z02}^2)\omega_{Y01}^2\omega_{Y02}^2 + (\omega_{Y01}^2 + \omega_{Y02}^2)\omega_{Z01}^2\omega_{Z02}^2 + \frac{2}{L_1C_3}\omega_{Z\infty}^2\omega_{Y\infty}^2\\ &\quad = \omega_{C1}^2\omega_{C2}^2\omega_{C3}^2 + \omega_{C2}^2\omega_{C3}^2\omega_{C4}^2 + \omega_{C3}^2\omega_{C4}^2\omega_{C1}^2 + \omega_{C4}^2\omega_{C1}^2\omega_{C2}^2.\end{aligned} \tag{2.102}$$

From the magnitude relations in Eqs. (2.92)∼(2.97), one gets respectively, as

$$\omega_{C5} = \omega_{Z02},\ \omega_{C6} = \omega_{Y02},\ \omega_{C7} = \omega_{Z01},\ \omega_{C8} = \omega_{Y01}, \tag{2.103}$$

$$\omega_{C5} = \omega_{Z02},\ \omega_{C6} = \omega_{Z01},\ \omega_{C7} = \omega_{Y02},\ \omega_{C8} = \omega_{Y01}, \tag{2.104}$$

$$\omega_{C5} = \omega_{Z02},\ \omega_{C6} = \omega_{Y02},\ \omega_{C7} = \omega_{Y01},\ \omega_{C8} = \omega_{Z01}, \tag{2.105}$$

$$\omega_{C5} = \omega_{Y02},\ \omega_{C6} = \omega_{Z02},\ \omega_{C7} = \omega_{Y01},\ \omega_{C8} = \omega_{Z01}, \tag{2.106}$$

$$\omega_{C5} = \omega_{Y02},\ \omega_{C6} = \omega_{Y01},\ \omega_{C7} = \omega_{Z02},\ \omega_{C8} = \omega_{Z01}, \tag{2.107}$$

$$\omega_{C5} = \omega_{Y02},\ \omega_{C6} = \omega_{Z02},\ \omega_{C7} = \omega_{Z01},\ \omega_{C8} = \omega_{Y01}. \tag{2.108}$$

From Eqs. (2.85)∼(2.87), (2.99)∼(2.102), one gets two solutions in the case of Eq. (2.103) for L–C elements, if L_1 is given.

Solution 1:

$$\begin{aligned}
C_1 &= \frac{B + \sqrt{B^2 - 4A}}{2x_5x_7L_1},\\
C_2 &= \left[\left(x_5 + x_7 - \frac{2x_5x_7}{B + \sqrt{B^2 - 4A}} - \frac{B + \sqrt{B^2 - 4A}}{2}\right)L_1\right]^{-1},\\
L_2 &= \frac{2}{(B + \sqrt{B^2 - 4A})C_2},\\
C_3 &= \frac{2}{[(x_1 + x_2 + x_3 + x_4) - (x_5 + x_6 + x_7 + x_8)]\,L_1},\\
L_3 &= \frac{B - \sqrt{B^2 - 4A}}{2x_6x_8C_3},\\
L_4 &= \left[\left(x_6 + x_8 - \frac{2x_6x_8}{B - \sqrt{B^2 - 4A}} - \frac{B - \sqrt{B^2 - 4A}}{2}\right)C_3\right]^{-1},\\
C_4 &= \frac{2}{(B - \sqrt{B^2 - 4A})L_4},
\end{aligned} \tag{2.109}$$

Solution 2:

$$
\begin{aligned}
C_1 &= \frac{B-\sqrt{B^2-4A}}{2x_5x_7L_1},\\
C_2 &= \left[\left(x_5+x_7-\frac{2x_5x_7}{B-\sqrt{B^2-4A}}-\frac{B-\sqrt{B^2-4A}}{2}\right)L_1\right]^{-1},\\
L_2 &= \frac{2}{(B-\sqrt{B^2-4A})C_2},\\
C_3 &= \frac{2}{\left[(x_1+x_2+x_3+x_4)-(x_5+x_6+x_7+x_8)\right]L_1},\\
L_3 &= \frac{B+\sqrt{B^2-4A}}{2x_6x_8C_3},\\
L_4 &= \left[\left(x_6+x_8-\frac{2x_6x_8}{B+\sqrt{B^2-4A}}-\frac{B+\sqrt{B^2-4A}}{2}\right)C_3\right]^{-1},\\
C_4 &= \frac{2}{(B+\sqrt{B^2-4A})L_4},
\end{aligned}
\tag{2.110}
$$

where A and B are calculated as follows:

$$A = \frac{D-[x_5x_7(x_6+x_8)+x_6x_8(x_5+x_7)]}{(x_1+x_2+x_3+x_4)-(x_5+x_6+x_7+x_8)}, \tag{2.111}$$

$$B = \frac{E-[x_5x_7+x_6x_8+(x_5+x_7)(x_6+x_8)]}{(x_1+x_2+x_3+x_4)-(x_5+x_6+x_7+x_8)}, \tag{2.112}$$

$$D = x_1x_2x_3+x_2x_3x_4+x_1x_2x_4+x_1x_3x_4, \tag{2.113}$$

$$E = x_1x_2+x_2x_3+x_3x_4+x_4x_1+x_1x_3+x_2x_4, \tag{2.114}$$

$$x_i = \omega_{Ci}^2 = (2\pi f_{Ci})^2,\ i=1,2,...,8. \tag{2.115}$$

In addition, the following conditions should be satisfied:

$$\Delta = B^2-4A \geq 0, \tag{2.116}$$

$$L_1, C_1, L_2, C_2, L_3, C_3, L_4, C_4 > 0. \tag{2.117}$$

When $\Delta = 0$, two solutions degenerate. Possible solutions for other cases of Eqs. (2.104)$\sim$(2.108) are shown in Appendix A.

In order to design an E-CRLH TL, cut-off frequencies $f_{C1}\sim f_{C8}$, and inductance L_1 are set as design parameters. From Eq. (2.99), one gets for positive cut-off frequencies

$$f_{C1}f_{C2}f_{C3}f_{C4} = f_{C5}f_{C6}f_{C7}f_{C8}. \tag{2.118}$$

Accordingly, the cut-off frequencies $f_{C1}\sim f_{C8}$ are not independent. Our design method can be described in the following steps:

1) Select seven of eight cut-off frequencies, the other is determined from Eq. (2.118).

2) By setting inductance L_1, other elements will be calculated from Eqs. (2.109) and (2.110).
3) Test the conditions in Eqs. (2.116), (2.117).
In a balanced case, two solutions for Eqs. (2.105), (2.106) and (2.108) are the same with two solutions for Eq. (2.103) since $x_5 = x_6$ and $x_7 = x_8$. Thus one may get maximum 6 solutions for a balanced case, and maximum 12 solutions for an unbalanced case with fixed design parameters (f_{C1}~f_{C8}, L_1). The variety of the solutions gives a chance to choose suitable L–C elements. From Eqs. (2.91), (2.109) and (2.110), the Bloch impedance becomes a function of L_1 with fixed cut-off frequencies f_{C1}~f_{C8}. So the Bloch impedance level is controlled by changing the value of L_1. Therefore the desired dispersion diagram and the Bloch impedance are designed easily by using the proposed closed-form solutions. In next section, some numerical examples will be presented for various cases.

2.2.3 Unbalanced case, balanced case, and mixed case

a. Unbalanced case

In order to check the validity of our method, let us first start an unbalanced case, where two sets of the short-circuited frequencies of the horizontal branch and the open-circuited frequencies of the vertical branch are different. For example, let us find a desired dispersion diagram in an unbalanced case with design frequencies: $f_{C2} = 3.000$ GHz, $f_{C3} = 4.000$ GHz, $f_{C4} = 10.00$ GHz, $f_{C5} = 2.000$ GHz, $f_{C6} = 2.500$ GHz, $f_{C7} = 4.500$ GHz, $f_{C8} = 5.000$ GHz. Then from Eq. (2.118), one gets $f_{C1} = 0.9375$ GHz.

Table 2.1: The solutions in an unbalanced case with $f_{C1} = 0.9375$ GHz, $f_{C2} = 3.000$ GHz, $f_{C3} = 4.000$ GHz, $f_{C4} = 10.00$ GHz, $f_{C5} = 2.000$ GHz, $f_{C6} = 2.500$ GHz, $f_{C7} = 4.500$ GHz, $f_{C8} = 5.000$ GHz.

Eqs.	Sol.	L_1 [nH]	C_1 [pF]	C_2 [pF]	L_2 [nH]	C_3 [pF]	L_3 [nH]	L_4 [nH]	C_4 [pF]
(2.103)	1	1.50	3.21	4.68	0.352	0.480	3.25	9.80	0.269
	2	1.50	2.00	2.72	0.969	0.480	5.20	9.24	0.178
(2.105)	1	1.50	2.60	2.37	0.694	0.480	4.01	14.2	0.186
	2	1.50	1.62	1.88	1.40	0.480	6.41	18.3	0.0902
(2.106)	1	1.50	1.66	2.96	0.557	0.480	6.26	8.50	0.310
	2	1.50	1.04	3.14	0.840	0.480	10.0	14.6	0.112
(2.108)	1	1.50	2.05	5.84	0.282	0.480	5.07	5.88	0.448
	2	1.50	1.28	4.54	0.581	0.480	8.12	7.41	0.222

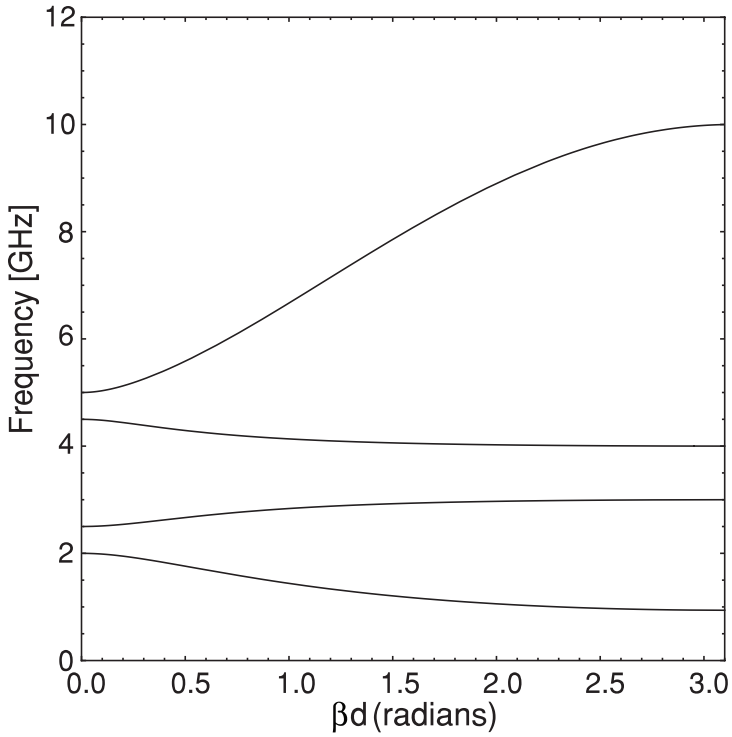

Figure 2.25: Dispersion diagram in an unbalanced case with the L–C elements in Table 2.1.

By setting $L_1 = 1.50$ nH and applying our closed-form solutions, totally eight solutions for Eqs. (2.103), (2.105), (2.106), and (2.108) are listed in Table 2.1. Solutions for Eqs. (2.104) and (2.107) do not satisfy the condition in Eq. (2.117) because C_2, L_2, C_4, and L_4 are found to be negative. Eight solutions have exactly the same dispersion diagram characteristic in Fig. 2.25. Curves connect smoothly the desired cut-off frequencies, as expected. From the dispersion diagram of the unbalanced case, one may able to design four pass-band (two RH and two LH bands) characteristics. Three gaps exist between these RH and LH bands. The Bloch impedances for Eqs. (2.103), (2.105), (2.106), and (2.108) are plotted in Figs. 2.26 (a), (b), (c), and (d), respectively. These figures show three stop-bands corresponding to three gaps in the dispersion diagram at (2.000∼2.500 GHz), (3.000∼4.000 GHz), and (4.500∼5.000 GHz). At the high-frequency band ($>$ 5.000 GHz) or the low-frequency band ($<$ 2.000 GHz), impedance matching may be facilitated. However, the Bloch impedances change dramatically at the middle-frequency bands (2.500∼3.000 GHz) and (4.000∼4.500 GHz). In these bands, it is not easy for the impedance matching.

While a proper method for deriving the parameters of the unbalanced E-CRLH TL is not yet reported, our closed-form solutions clearly have effectiveness for deriving this case. In addition, the ability to select flexibly the cut-off frequencies f_{C1}∼f_{C8} is beneficial for designing the resonant frequencies of a multi-band antenna, and building the pass- or stop-bands of a filter.

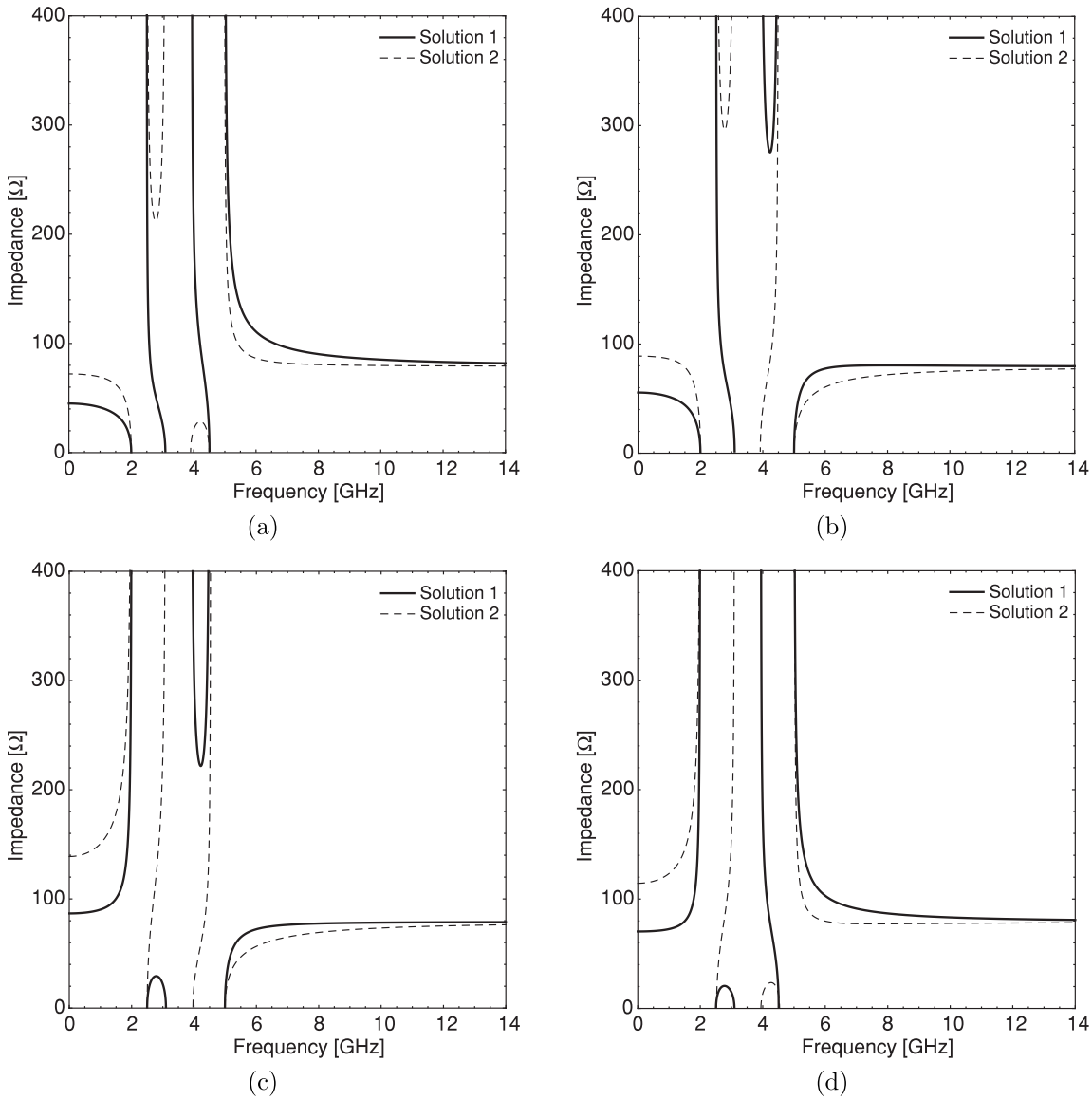

Figure 2.26: Bloch impedances in an unbalanced case with the L–C elements in Table 2.1. (a) Bloch impedance for Eq. (2.103). (b) Bloch impedance for Eq. (2.105). (c) Bloch impedance for Eq. (2.106). (d) Bloch impedance for Eq. (2.108).

b. Mixed case

Tri-pass band characteristics can also be realizable by choosing $f_{C5} = f_{C6}$ or $f_{C7} = f_{C8}$. This means that the one set of the short-circuited frequencies of the horizontal branch and the open-circuited frequencies of the vertical branch is equal (balanced case) while the another set of those is different (unbalanced case). This mixed case of the E-CRLH TL has not been mentioned in previous papers. A numerical example for $f_{C5} = f_{C6}$ is presented for this case. Design parameters are set to be $f_{C1} = 0.7500$ GHz, $f_{C2} = 3.000$ GHz, $f_{C3} = 4.000$ GHz, $f_{C4} = 10.00$ GHz, $f_{C5} = f_{C6} = 2.000$ GHz, $f_{C7} = 4.500$ GHz, $f_{C8} = 5.000$ GHz, and $L_1 = 1.50$ nH. Possible meaningful solutions are listed in Table 2.2.

The dispersion diagram of these solutions is plotted in Fig. 2.27. The Bloch impedances are calculated in Fig. 2.28 (a) for Eqs. (2.103) and (2.108), and in Fig. 2.28 (b) for Eqs. (2.105)

and (2.106). Two stop-bands at (3.000∼4.000 GHz) and (4.500∼5.000 GHz) are shown in these figures. At the middle-frequency band (4.000∼4.500 GHz) and the high-frequency band (> 5.000 GHz), the Bloch impedances of two solutions show similar frequency behaviors with the unbalanced case in Figs. 2.26 (a) and (b). On the other hand, the Bloch impedances exhibit a complementary behavior at the low-frequency band (< 3.000 GHz).

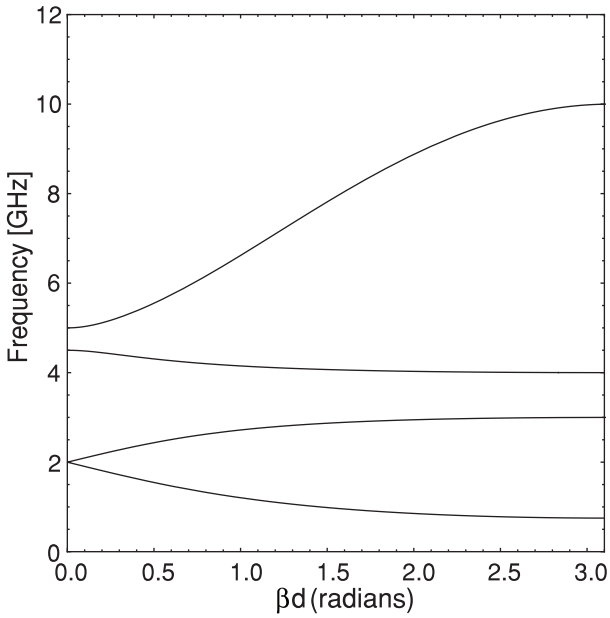

Figure 2.27: Dispersion diagram in an mixed case with the L–C elements in Table 2.2.

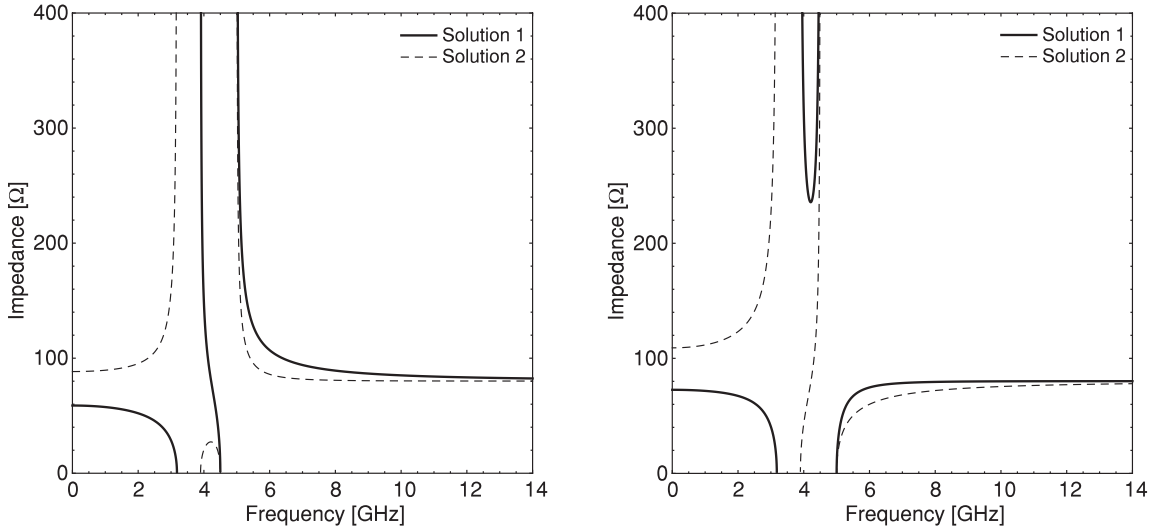

Figure 2.28: Bloch impedances in a mixed case with the L–C elements in Table 2.2. (a) Bloch impedance for Eqs. (2.103) and (2.108). (b) Bloch impedance for Eqs. (2.105) and (2.106).

Table 2.2: The solutions in a mixed case with $f_{C1} = 0.7500$ GHz, $f_{C2} = 3.000$ GHz, $f_{C3} = 4.000$ GHz, $f_{C4} = 10.00$ GHz, $f_{C5} = f_{C6} = 2.000$ GHz, $f_{C7} = 4.500$ GHz, $f_{C8} = 5.000$ GHz.

Eqs.	Sol.	L_1 [nH]	C_1 [pF]	C_2 [pF]	L_2 [nH]	C_3 [pF]	L_3 [nH]	L_4 [nH]	C_4 [pF]
(2.103), (2.108)	1	1.50	3.17	4.53	0.368	0.467	5.49	6.03	0.415
	2	1.50	2.11	2.76	0.908	0.467	8.24	7.51	0.222
(2.105), (2.106)	1	1.50	2.57	2.34	0.714	0.467	6.77	8.85	0.283
	2	1.50	1.71	1.88	1.33	0.467	10.2	14.6	0.115

c. Balanced case

For a balanced case with design parameters: $f_{C1} = 0.7500$ GHz, $f_{C2} = 3.000$ GHz, $f_{C3} = 4.000$ GHz, $f_{C4} = 9.000$ GHz, $f_{C5} = f_{C6} = 2.000$ GHz, $f_{C7} = f_{C8} = 4.500$ GHz, and $L_1 = 1.50$ nH, two solutions for Eqs. (2.103), (2.105), (2.106), and (2.108) are shown in Table 2.3. Physically meaningful solutions also do not exist for Eqs. (2.104) and (2.107). Figures 2.29 and 2.30 present the dispersion diagram and the Bloch impedances for this case. The dispersion diagram shows a dual-pass band characteristic at (0.7500∼3.000 GHz) and (4.000∼9.000 GHz). The Bloch impedance exhibits a complementary behavior, and has one stop-band corresponding to one gap in the dispersion diagram at (3.000∼4.000 GHz).

Table 2.3: The solutions in a balanced case with $f_{C1} = 0.7500$ GHz, $f_{C2} = 3.000$ GHz, $f_{C3} = 4.000$ GHz, $f_{C4} = 9.000$ GHz, $f_{C5} = f_{C6} = 2.000$ GHz, $f_{C7} = f_{C8} = 4.500$ GHz.

Eqs.	Sol.	L_1 [nH]	C_1 [pF]	C_2 [pF]	L_2 [nH]	C_3 [pF]	L_3 [nH]	L_4 [nH]	C_4 [pF]
(2.103), (2.105)	1	1.50	3.24	4.83	0.338	0.582	5.34	7.07	0.361
(2.106), (2.108)	2	1.50	2.07	2.74	0.931	0.582	8.35	12.4	0.131

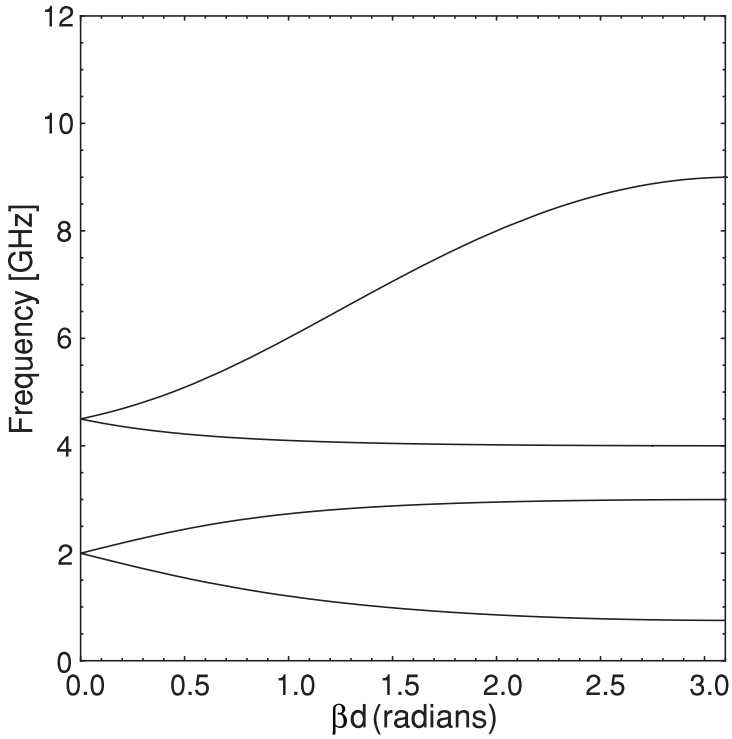

Figure 2.29: Dispersion diagram in a balanced case with the L–C elements in Table 2.3.

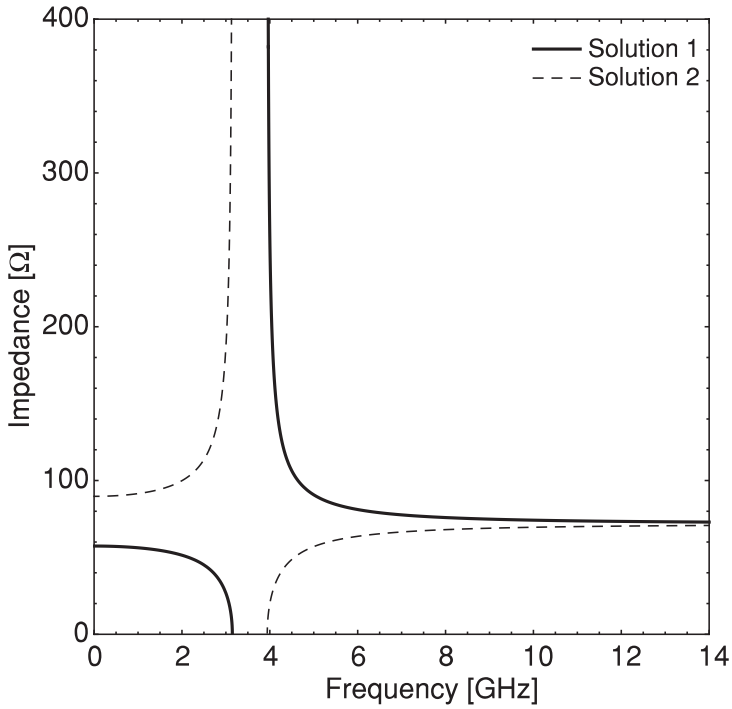

Figure 2.30: Bloch impedance in a balanced case with the L–C elements in Table 2.3.

2.2.4 A special case for a constant Bloch impedance

A constant Bloch impedance allows us an easy broadband impedance matching with other circuits, and is preferable for many practical applications. From Eq. (2.91), one gets a constant Bloch impedance

$$Z_B = \sqrt{2L_1/C_3}, \tag{2.119}$$

by setting:

$$\omega_{Z01} = \omega_{Y01}, \quad \omega_{Z02} = \omega_{Y02}, \quad \omega_{Z\infty} = \omega_{Y\infty}. \tag{2.120}$$

This is a special case of the balanced E-CRLH TL for Eqs. (2.103), (2.105), (2.106), and (2.108). It leads to $\Delta = 0$ and two solutions degenerate. Thus L–C elements become

$$C_1 = \frac{B}{2x_5x_7L_1}, \tag{2.121}$$

$$C_2 = \left[\left(x_5 + x_7 - \frac{2x_5x_7}{B} - \frac{B}{2}\right)L_1\right]^{-1}, \tag{2.122}$$

$$L_2 = \frac{2}{BC_2}, \tag{2.123}$$

$$C_3 = \frac{2}{\left[(x_1 + x_2 + x_3 + x_4) - (x_5 + x_6 + x_7 + x_8)\right]L_1}, \tag{2.124}$$

$$L_3 = \frac{B}{2x_6x_8C_3}, \tag{2.125}$$

$$L_4 = \left[\left(x_6 + x_8 - \frac{2x_6x_8}{B} - \frac{B}{2}\right)C_3\right]^{-1}, \tag{2.126}$$

$$C_4 = \frac{2}{BL_4}, \tag{2.127}$$

where

$$x_5 = x_6, \quad x_7 = x_8, \quad x_5x_7 = x_6x_8 = \sqrt{x_1x_2x_3x_4}, \quad x_5 + x_7 = x_6 + x_8 = T, \tag{2.128}$$

and T is calculated from the following equation:

$$\begin{aligned} &T^4 - (12\sqrt{x_1x_2x_3x_4} + 2E)\,T^2 + \left[8\,(x_1 + x_2 + x_3 + x_4)\,\sqrt{x_1x_2x_3x_4} + 8D\right]T \\ &\quad + \left(E - 2\sqrt{x_1x_2x_3x_4}\right)^2 - 4D(x_1 + x_2 + x_3 + x_4) = 0. \end{aligned} \tag{2.129}$$

In this case, cut-off frequencies f_{C5}~f_{C8} are calculated from f_{C1}~f_{C4} because of the setting $\omega_{Z\infty} = \omega_{Y\infty}$. Equation (2.129) may have four possible roots. However, only the real and positive roots are chosen to satisfy the condition in Eq. (2.117). From Eqs. (2.119)

and (2.124), the relation between L_1 and Z_B is

$$L_1 = \frac{Z_B}{\sqrt{(x_1 + x_2 + x_3 + x_4) - (x_5 + x_6 + x_7 + x_8)}}. \tag{2.130}$$

Inductance L_1 may be determined from a desired Z_B for an impedance matching. For example, let us design a desired dispersion diagram in a special case from design parameters: $Z_B = 50.00\ \Omega$, $f_{C1} = 0.7500$ GHz, $f_{C2} = 3.000$ GHz, $f_{C3} = 4.000$ GHz, and $f_{C4} = 9.000$ GHz. With these design parameters, one gets four roots of T ($T_1 = -3.435 \times 10^{21}, T_2 = 4.145 \times 10^{20}, T_3 = 1.954 \times 10^{21}, T_4 = 1.066 \times 10^{21}$) from Eq. (2.129). Only $T = 1.066 \times 10^{21}$ satisfies the condition. Then L–C elements are calculated from Eqs. (2.121)∼(2.127), and (2.130), and are shown in Table 2.4. The cut-off frequencies f_{C5}∼f_{C8} are given as $f_{C5} = f_{C6} = 1.854$ GHz, $f_{C7} = f_{C8} = 4.854$ GHz from Eq. (2.128).

Table 2.4: The solutions in a special case with $Z_B = 50.00\ \Omega$, $f_{C1} = 0.7500$ GHz, $f_{C2} = 3.000$ GHz, $f_{C3} = 4.000$ GHz, $f_{C4} = 9.000$ GHz.

Eqs.	Sol.	L_1 [nH]	C_1 [pF]	C_2 [pF]	L_2 [nH]	C_3 [pF]	L_3 [nH]	L_4 [nH]	C_4 [pF]
(2.103), (2.105), (2.106), (2.108)	1, 2	1.10	3.63	2.92	0.682	0.878	4.53	3.65	0.546

Figures 2.31 and 2.32 present dispersion diagram and Bloch impedance of the designed E-CRLH TL in this special case. One should notice that the gap between f_{C2} and f_{C3} is unavoidable due to the band-stop nature of the D-CRLH TL [10].

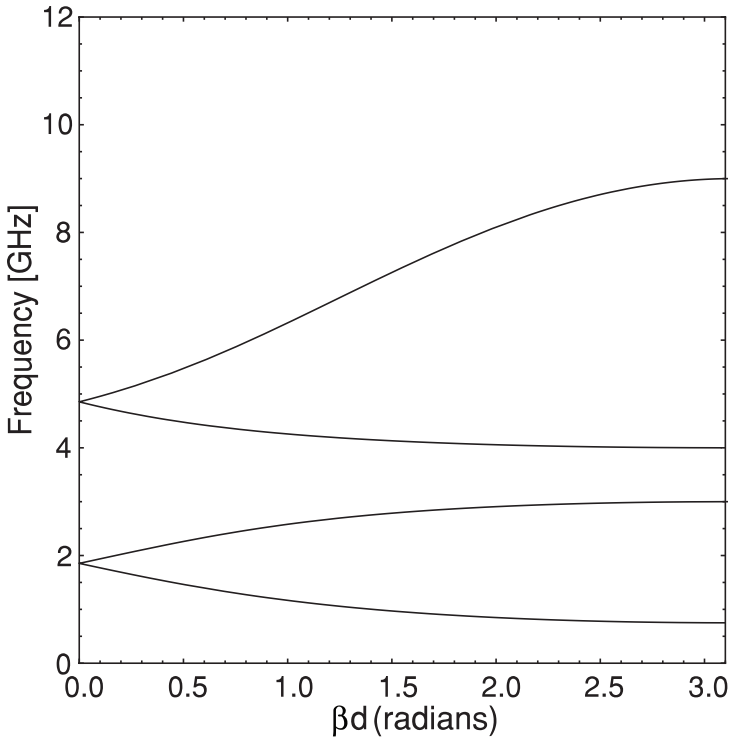

Figure 2.31: Dispersion diagram in a special case with the L–C elements in Table 2.4.

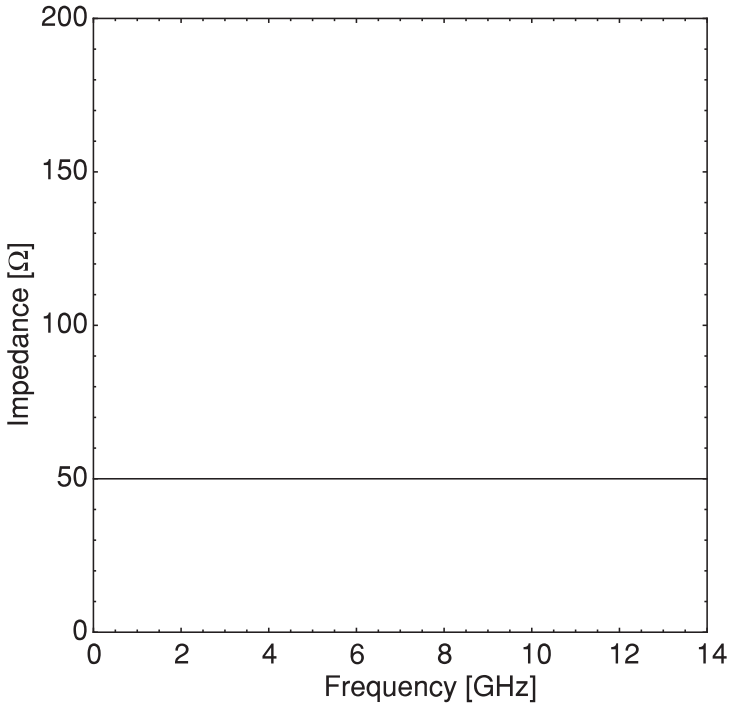

Figure 2.32: Bloch impedance in a special case with the L–C elements in Table 2.4.

2.2.5 Scattering parameters

Scattering parameters of the E-CRLH TLs for various cases in the previous subsections are calculated to check the impedance matching for a network connection. A periodic E-CRLH TL unit cells network is shown in Fig. 2.33 with standard 50.00 Ω impedances in two ports, and N is the number of unit cells. L–C elements in each cell are given from Solution 1 of Eq. (2.103) in Tables 2.1, 2.2, and 2.3 for an unbalanced case, a mixed case, and a balanced case, respectively, and in Table 2.4 for a special case.

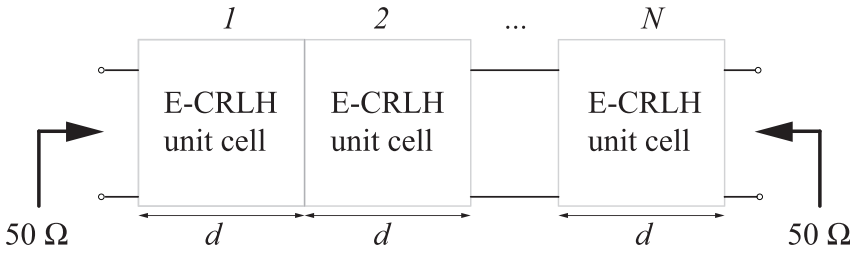

Figure 2.33: A periodic E-CRLH TL unit-cells network.

Important parameter in design process is the number of unit cells. Effect of the number of unit cells is illustrated in Fig. 2.34 by calculating S_{21} characteristic for different number N. A similar effect with the investigation of the CRLH TL unit cells network in Ref. [8] can be seen here. The small number of unit cells provides weak-slope edges of the bands, while the cutoffs are sharp as the number of cells are increased. The balanced and special cases have dual-band characteristics even designed with one cell. The highlight point occurs at $N = 1$ in the unbalanced and mixed cases. These cases show dual-band properties. One needs a larger number of the unit cells to accomplish the quad-band and tri-band properties. From our calculation, N should be selected to be larger than 3 for better filter performance.

With $N = 10$, calculated S_{11} and S_{21} of these designed E-CRLH TLs are presented in Fig. 2.35. S_{11} and S_{21} show the impedance matching and filtering characteristics. For practical applications, pass-bands are determined at frequencies in which $|S_{21}| = -3$ dB. These frequencies may slightly differ the cut-off frequencies $f_{C1} \sim f_{C8}$ of RH and LH bands. For example, the pass bands of the designed E-CRLH TL in the unbalanced case are $(0.954 \sim 1.915$ GHz), $(2.546 \sim 2.993$ GHz), $(4.001 \sim 4.517$ GHz) and $(5.361 \sim 9.884$ GHz). Therefore, the bandwidth of RH and LH bands in the dispersion diagram should be designed large enough to get desired pass-bands in S-parameters.

To avoid complexity, S-parameters of the E-CRLH TL in the unbalanced case have not been characterized [10, 19, 20]. By using our closed-form solutions, Figure 2.35 (a) confirms that the E-CRLH TL in the unbalanced case can be applied easily for quad-band applications while the mixed case is preferred for tri-band applications as can be seen from Fig. 2.35 (b). On the other hand, this section presents the results for one solution

of these case, while eight and four solutions for L–C elements are available from Tables 2.1 and 2.2. Since each solution has a distinct Bloch impedance for the impedance matching consideration, one may choose a best solution depend on the performance of S-parameters. Both the balanced case and the special case are suitable for dual-band applications from Figs. 2.35 (c) and (d). The main difference between the balanced case and the special case are the performance of S_{11} and the bandwidth of RH, LH bands.

With the constant Bloch impedance, the special case has better S_{11} characteristic than the balanced case. However, the balanced case is easier to control the bandwidth of RH and LH bands because of a flexibility of selecting $f_{C5}{\sim}f_{C8}$, while the cut-off frequencies $f_{C5}{\sim}f_{C8}$ of the special case are calculated from $f_{C1}{\sim}f_{C4}$ in Eqs. (2.128) and (2.129). The bandwidth of RH and LH bands is useful for positive/negative index artificial lenses. In order to evaluate our method for designing S-parameters of E-CRLH TL, one may compare with previous results. Reference [10] already presented S-parameters of a balanced E-CRLH TL consisting of 10 unit-cells. This case is similar to a special case with a constant Bloch impedance, since the balanced case of homogeneous E-CRLH medium in Ref. [10] associate with a constant characteristic impedance. Our closed-form solutions in the special case can be used to calculate L–C elements from cut-off frequencies $f_{C1}{\sim}f_{C4}$ and Bloch impedance. The design parameters for this case are $f_{C1} = 0.726$ GHz, $f_{C2} = 1.953$ GHz, $f_{C3} = 2.351$ GHz, $f_{C4} = 6.311$ GHz (these cut-off frequencies are chosen approximately from Fig. 6 of Ref. [10]), and $Z_B = 50.00\ \Omega$.

Then one gets four roots of T ($T_1 = -1.558 \times 10^{21}, T_2 = 2.744 \times 10^{20}, T_3 = 4.499 \times 10^{20}, T_4 = 8.335 \times 10^{20}$) from Eq. (2.129). Only $T = 4.499 \times 10^{20}$ satisfies the condition in Eq. (2.117). L–C elements are calculated from Eqs. (2.121)∼(2.128), and (2.130) as $L_1 = 1.534$ nH, $C_1 = 3.604$ pF, $C_2 = 7.428$ pF, $L_2 = 0.7426$ nH, $C_3 = 1.227$ pF, $L_3 = 4.505$ nH, $L_4 = 9.284$ nH, and $C_4 = 0.5941$ pF. The cut-off frequencies $f_{C5}{\sim}f_{C8}$ are given as $f_{C5} = f_{C6} = 1.522$ GHz, and $f_{C7} = f_{C8} = 3.013$ GHz from Eq. (2.128). Figure 2.36 shows the S-parameters of the designed E-CRLH TL connected 10 cells in cascade. From the calculated results, the proposed approach gives us the results comparable with those in Fig. 6 of Ref. [10]. It confirms the good quality of our method for designing S-parameters of E-CRLH TL circuit.

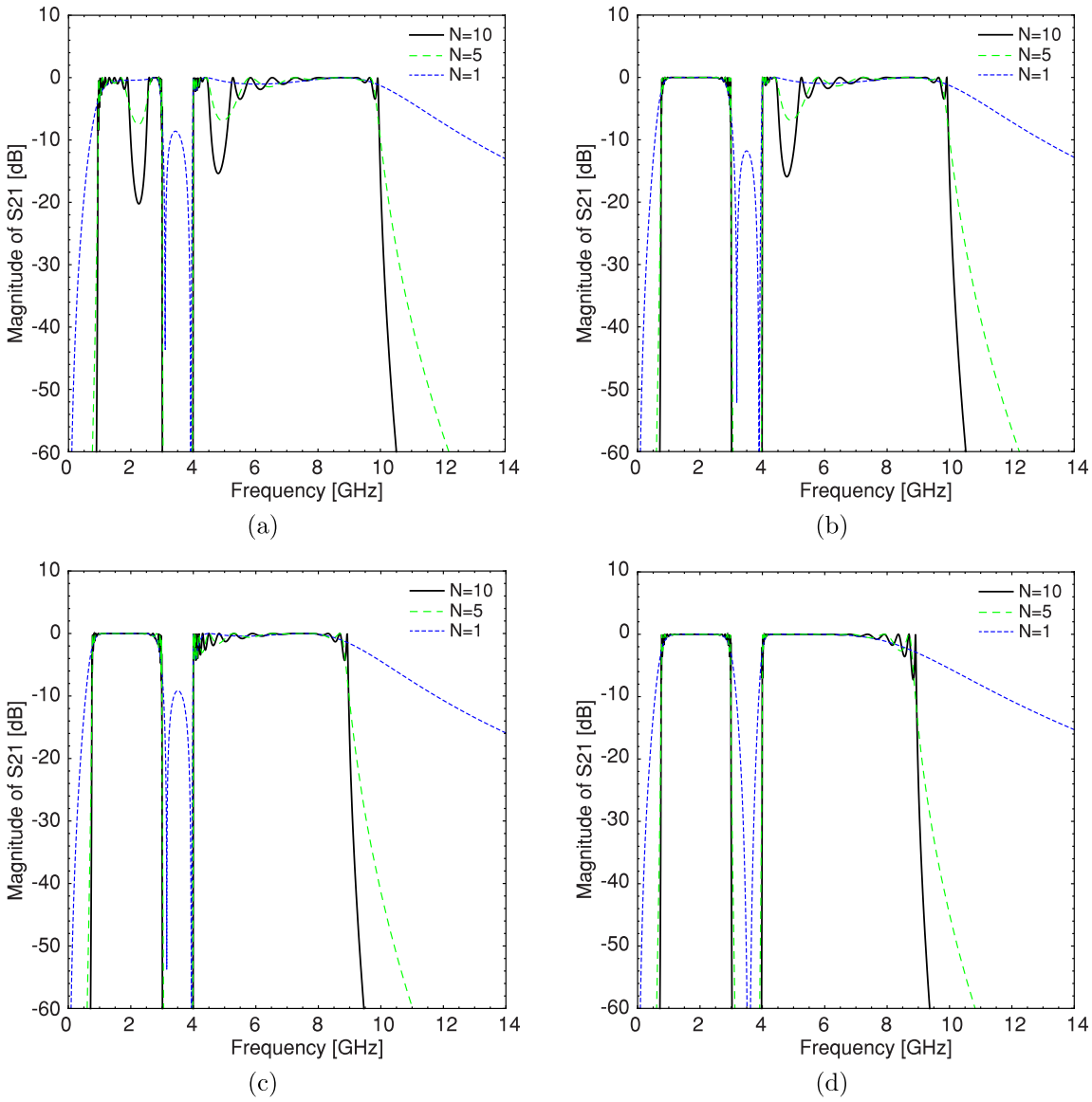

Figure 2.34: S_{21} characteristic for different number N of unit cells, $N = 1$, 5, and 10, (a) an unbalanced case with the L–C elements from Solution 1 of Eq. (2.103) in Table 2.1, (b) a mixed case with the L–C elements from Solution 1 of Eq. (2.103) in Table 2.2, (c) a balanced case with the L–C elements from Solution 1 of Eq. (2.103) in Table 2.3, (d) a special case with the L–C elements in Table 2.4.

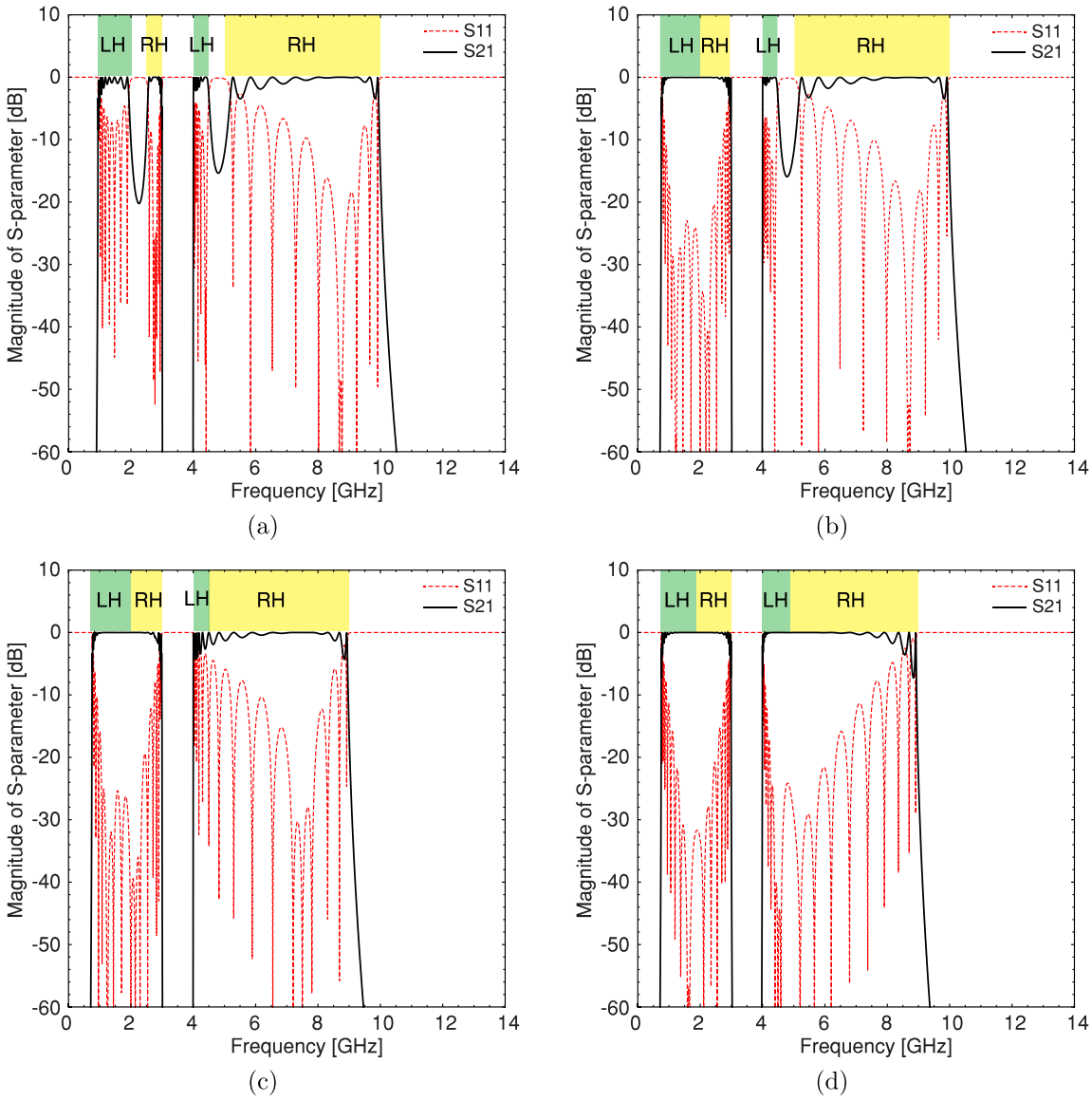

Figure 2.35: Calculated S-parameters of E-CRLH TL for 10 cells network, S_{11} (dashed line), S_{21} (solid line), (a) an unbalanced case with the L–C elements from Solution 1 of Eq. (2.103) in Table 2.1, (b) a mixed case with the L–C elements from Solution 1 of Eq. (2.103) in Table 2.2, (c) a balanced case with the L–C elements from Solution 1 of Eq. (2.103) in Table 2.3, (d) a special case with the L–C elements in Table 2.4. Shading areas indicate RH and LH bands.

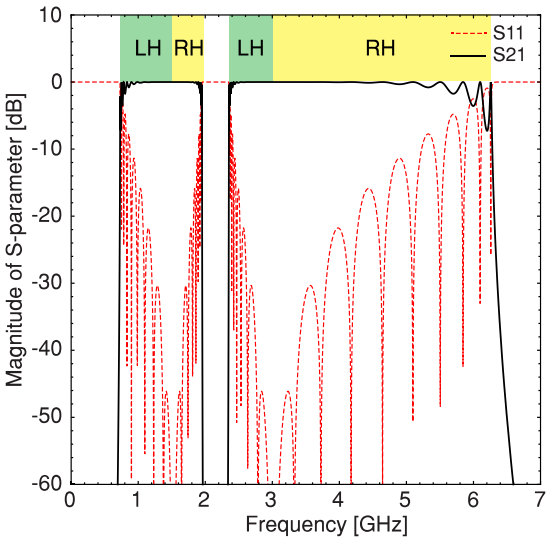

Figure 2.36: Calculated S-parameters of E-CRLH TL for 10 cells network with L–C elements: $L_1 = 1.534$ nH, $C_1 = 3.604$ pF, $C_2 = 7.428$ pF, $L_2 = 0.7426$ nH, $C_3 = 1.227$ pF, $L_3 = 4.505$ nH, $L_4 = 9.284$ nH, and $C_4 = 0.5941$ pF.

2.2.6 Desired phase characteristic

This section presents for designing E-CRLH TL to achieve a desired phase characteristic $\phi_0 = \beta d$ ($-\phi_0$ in two LH bands, $+\phi_0$ in two RH bands) at four design frequencies f_{C1}~f_{C4} as shown in Fig. 2.37. It is useful for phase shift devices such as directional couplers and power dividers. For this case, the design frequencies f_{C1}~f_{C4} are determined from the equation:

$$Z_h Y_v + 1 - \cos(\phi_0) = 0. \tag{2.131}$$

Similarly, for Eq. (2.103), design equations for C_1, C_2, L_2, L_3, L_4, and C_4 are retained as shown in Eqs. (2.109) and (2.110) except that C_3 is given by

$$C_3 = \frac{1 - \cos(\phi_0)}{\left[(x_1 + x_2 + x_3 + x_4) - (x_5 + x_6 + x_7 + x_8)\right] L_1}. \tag{2.132}$$

While the solutions for Eqs. (2.104)~(2.108) are shown in Appendix A. For a constant Bloch impedance of the special case, design equations of C_1, C_2, L_2, L_3, L_4, and C_4 are the same with Eqs. (2.121)~(2.123), (2.125)~(2.127), and C_3 is calculated from Eq. (2.132). The relation between L_1 and Z_B becomes

$$L_1 = Z_B \sqrt{\frac{1 - \cos(\phi_0)}{2\left[(x_1 + x_2 + x_3 + x_4) - (x_5 + x_6 + x_7 + x_8)\right]}}. \tag{2.133}$$

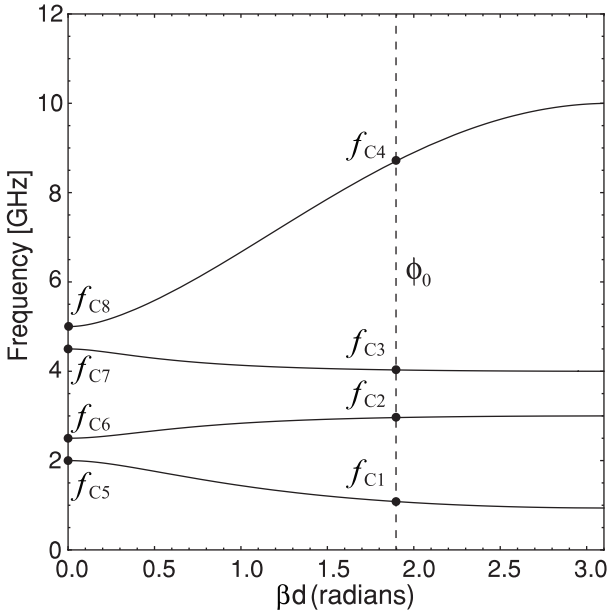

Figure 2.37: Dispersion diagram in a general unbalanced case for a desired phase characteristic ($\phi_0 = \beta d$).

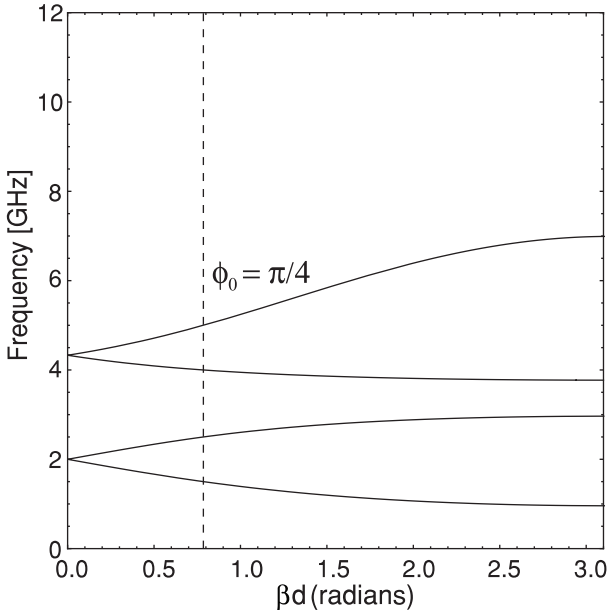

Figure 2.38: Dispersion diagram in a special case with the L–C elements in Table 2.5

For designing phase shift devices, it is important to achieve a desired phase characteristic at four design frequencies f_{C1}∼f_{C4} and to have good impedance matching. A numerical example for designing $\pi/4$ phase characteristic in a special case are listed in Table 2.5. The design procedures in the previous sections are used for obtaining these L–C elements.

Table 2.5: An example of $\pi/4$ phase characteristic.

$\phi_0 = \pi/4$ at $f_{C1} = 1.500$ GHz, $f_{C2} = 2.500$ GHz, $f_{C3} = 4.000$ GHz, $f_{C4} = 5.000$ GHz, $Z_B = 50.00\ \Omega$. $T = 8.981 \times 10^{20}$. $f_{C5} = f_{C6} = 2.000$ GHz, $f_{C7} = f_{C8} = 4.330$ GHz.									
Eqs.	Sol.	L_1 [nH]	C_1 [pF]	C_2 [pF]	L_2 [nH]	C_3 [pF]	L_3 [nH]	L_4 [nH]	C_4 [pF]
(2.103), (2.105) (2.106), (2.108)	1, 2	1.52	2.63	3.65	0.584	1.22	3.29	4.56	0.468

Figures 2.38 shows the corresponding dispersion diagram calculated from the L–C elements in Table 2.5. The dispersion diagram presents correctly four designed frequencies, $f_{C1} = 1.500$ GHz, $f_{C2} = 2.500$ GHz, $f_{C3} = 4.000$ GHz, and $f_{C4} = 5.000$ GHz at the desired phase characteristics $\phi_0 = \pi/4$. Our calculated result covers the result in Fig. 2 of Ref. [19], in which the balanced case with some specified conditions is a special case in this paper. Therefore our design equations are in a general form and can be used for many cases, while the design equations of Ref. [19] may only be used for a special case.

2.3 A compact metamaterial antenna based on asymmetric E-CRLH TL unit cell for multiband applications

2.3.1 Introduction

Nowadays, the development of modern wireless communication systems requires compact devices to work at different standards. It leads to the necessary of designing small antennas with a multiband operation [22]. Many studies on dual- and tri-band antennas have been reported while quad-band antennas are seldom proposed. To compare with dual- and tri-band antennas, quad-band antennas are more desirable for reducing the fabrication cost. Some kinds of quad-band have been designed by using conventional methods such as a monopole antenna [23], slot antennas [24]–[27], a fractal antenna [28], a pentangle-loop antenna [29], and a Hilbert shaped antenna [30]. However, they still have large size in corresponding to the wavelength at their operating frequencies. Other more compact techniques have also been presented in the literature based on parasitic elements [31], loops [32], and matching networks [33].

Metamaterials provide a conceptual way to reduce the size of the antennas for satisfying the requirements of modern wireless communication systems. Composite right/left handed transmission line (CRLH TL) and dual-composite right/left handed transmission line (D-CRLH TL) have been employed to design many compact dual- and tri-band antennas for wireless communications [34]–[38]. Few antennas based on E-CRLH TL and NRI-TL were proposed up to now. A dual-band leaky wave antenna comprising 10 NRI-TL unit cells was simulated in Ref. [39]. Another dual-band leaky wave antenna has been designed from 10 E-CRLH unit cells in Ref. [40]. These leaky wave antennas are used in specific radar applications for their capability of beam scanning and high directivity. Reference [41] presents a dual-band antenna based on a modified asymmetric NRI-TL unit cell. This antenna has a compact size, but exhibits a very low gain at the operating frequencies. More recently, a multiband antenna based on one asymmetric E-CRLH unit cell is designed for quad-band [42]. However, the resonant frequencies are not analyzed yet.

In our previous section, symmetric E-CRLH TL can be applied for quad-, dual-, and tri-band application by selecting the cut-off frequencies of the dispersion diagram in unbalanced, balanced, and mixed cases, respectively. In this section, the design scheme is now extended to apply for asymmetric cases. By carefully choosing the L–C lumped circuit elements, one can analyze the resonant frequencies of the E-CRLH antennas.

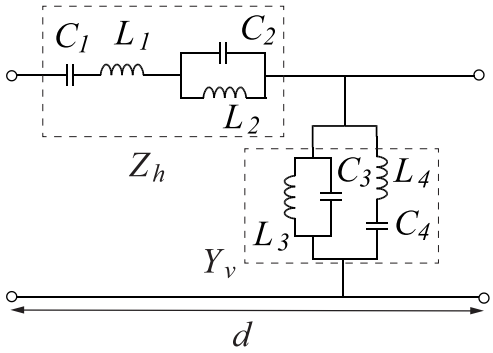

Figure 2.39: Equivalent circuit of an asymmetric E-CRLH unit cell

In order to show the realizability of this design, a quad-band antenna has been made from an unit cell of asymmetric E-CRLH TL on a co-planar printed circuit board. The proposed antenna in this study has a compact size to compare with the previously proposed quad-band antennas.

2.3.2 Antenna analysis and design

The equivalent circuit of an asymmetric E-CRLH unit cell is shown in Fig. 2.39. In the horizontal branch, a series L_1–C_1 resonator connects in series with a parallel L_2–C_2 resonator. The vertical branch contains a parallel L_3–C_3 resonator in shunt with a series L_4–C_4 resonator. The impedance Z_h of the horizontal branch and the admittance Y_v of the vertical branch are given respectively by

$$Z_h = \frac{jL_1(\omega^2 - \omega_{Z01}^2)(\omega^2 - \omega_{Z02}^2)}{\omega(\omega^2 - \omega_{Z\infty}^2)}, \tag{2.134}$$

$$Y_v = \frac{jC_3(\omega^2 - \omega_{Y01}^2)(\omega^2 - \omega_{Y02}^2)}{\omega(\omega^2 - \omega_{Y\infty}^2)}, \tag{2.135}$$

where

$$\omega_{Z\infty}^2 = \frac{1}{L_2C_2},\ \omega_{Y\infty}^2 = \frac{1}{L_4C_4}, \tag{2.136}$$

$$\omega_{Z01}^2 = \frac{B_1 + \sqrt{B_1^2 - 4A_1}}{2},\ \omega_{Z02}^2 = \frac{B_1 - \sqrt{B_1^2 - 4A_1}}{2}, \tag{2.137}$$

$$\omega_{Y01}^2 = \frac{B_2 + \sqrt{B_2^2 - 4A_2}}{2},\ \omega_{Y02}^2 = \frac{B_2 - \sqrt{B_2^2 - 4A_2}}{2}, \tag{2.138}$$

$$A_1 = \frac{1}{L_1C_1L_2C_2},\ B_1 = \frac{1}{L_1C_1} + \frac{1}{L_2C_2} + \frac{1}{L_1C_2}, \tag{2.139}$$

$$A_2 = \frac{1}{L_3C_3L_4C_4},\ B_2 = \frac{1}{L_3C_3} + \frac{1}{L_4C_4} + \frac{1}{L_4C_3}. \tag{2.140}$$

By using the results for the asymmetric unit cell in Section 2.1.6, the dispersion relation is obtained as

$$\cos(\beta d) = 1 + \frac{Z_h Y_v}{2}, \tag{2.141}$$

where β is the propagation constant for the Bloch waves, and d is the length of the unit cell. To realize an antenna based on E-CRLH resonators in a general N unit cells, the following resonant condition should be applied:

$$\beta d N = n\pi, \tag{2.142}$$

where the resonant modal index n can be positive integers for RH bands, zero and negative integers for LH bands. Therefore, one may calculate the resonant frequencies of an antenna based on N-asymmetric E-CRLH unit cell as:

$$1 + \frac{Z_h Y_v}{2} - \cos(\frac{n\pi}{N}) = 0, \qquad n = 0, \pm 1, \pm 2, ..., \pm N, \tag{2.143}$$

which is a fourth order equation with respect to ω^2. Since the proposed antenna has built from one unit cell ($N = 1$), possible resonant frequencies are calculated for even integer n from

$$(\omega^2 - \omega_{Z01}^2)(\omega^2 - \omega_{Z02}^2)(\omega^2 - \omega_{Y01}^2)(\omega^2 - \omega_{Y02}^2) = 0, \tag{2.144}$$

and for odd integer n from

$$\begin{aligned}\omega^8 - (B_1 + B_2 + \frac{4}{L_1 C_3})\omega^6 + (A_1 + A_2 + B_1 B_2 + \frac{4\omega_{Z\infty}^2 + 4\omega_{Y\infty}^2}{L_1 C_3})\omega^4 \\ - (B_1 A_2 + B_2 A_1 + \frac{4\omega_{Z\infty}^2 \omega_{Y\infty}^2}{L_1 C_3})\omega^2 + A_1 A_2 = 0.\end{aligned} \tag{2.145}$$

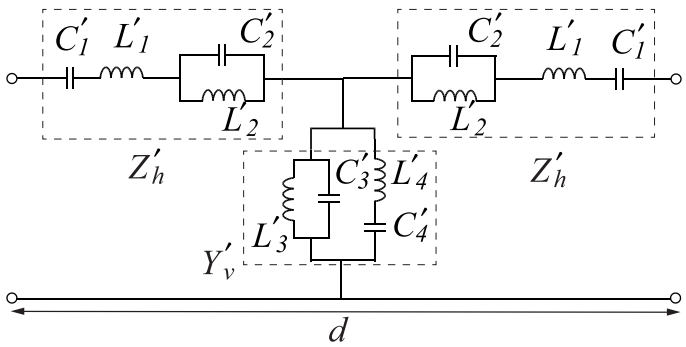

Figure 2.40: Equivalent circuit of a symmetric E-CRLH unit cell

In this study, an asymmetric E-CRLH unit cell in Fig. 2.39 is chosen to design the antenna because of smaller configuration to compare with symmetric E-CRLH unit cell in Fig. 2.40. Closed-form solutions can still be derived for the asymmetric E-CRLH unit cell by setting

$$L_1 = 2L_1^{'},\ C_1 = C_1^{'}/2,\ L_2 = 2L_2^{'},\ C_2 = C_2^{'}/2,\ L_3 = L_3^{'},\ C_3 = C_3^{'},\ L_4 = L_4^{'},\ C_4 = C_4^{'}, \quad (2.146)$$

or

$$L_1 = L_1^{'},\ C_1 = C_1^{'},\ L_2 = L_2^{'},\ C_2 = C_2^{'},\ L_3 = L_3^{'}/2,\ C_3 = 2C_3^{'},\ L_4 = L_4^{'}/2,\ C_4 = 2C_4^{'}. \quad (2.147)$$

These settings lead to $Z_h Y_v/2 = Z_h^{'} Y_v^{'}$, then one gets the same dispersion diagram between asymmetric and symmetric E-CRLH unit cells.

The configuration of the proposed antenna has been built from one asymmetric E-CRLH unit cell in Fig. 2.41. A CPW configuration with a FR4 substrate with dielectric constant $\varepsilon_r = 4.4$, $\tan\delta = 0.02$, 1.6 mm substrate thickness and 35 μm copper layer thickness is used in this study. As can be seen from this figure, the antenna structure can be expressed by lumped elements. The capacitors C_1, C_2, C_3 and C_4 are formed by interdigital capacitors while the inductors L_1, L_2, L_3 and L_4 are realized by meander strip lines. The dimensions of the proposed antenna are shown in Table 2.6. The design equations to calculate the capacitance value of the interdigital capacitors and the inductance value of the meander strip lines can be found in [43]. Then we get L_1 = 25.9 nH, C_1 = 2.62 pF, L_2 = 22.3 nH, C_2 = 1.93 pF, L_3 = 8.36 nH, C_3 = 0.36 pF, L_4 = 12.0 nH, C_4 = 0.12 pF. Using Eq. (2.141), the dispersion diagram of the proposed asymmetric E-CRLH unit cell is plotted in Fig. 2.42. The dispersion diagram is in an unbalance case with two RH and two LH bands. One may use the dispersion diagram to determine which resonant modal index n corresponds to resonant frequencies of the proposed antenna. The possible resonant frequencies of the proposed antenna are calculated from Eq. (2.144) for $n = 0$ as 0.41 GHz, 1.14 GHz, 2.38 GHz and 5.12 GHz. This corresponds to $\beta d = 0$ in the dispersion diagram. The other possible resonant frequencies of the proposed antennas can get from Eq. (2.145) and $\beta d = \pi$ in the dispersion diagram as (3.29 GHz, 5.69 GHz) for $n = +1$, and (0.32 GHz, 0.92 GHz) for $n = -1$.

The simulated return loss of the proposed antenna from 0.1 GHz to 6 GHz is presented in Fig. 2.43. The resonant frequencies of the antenna are simulated to be 0.38 GHz, 0.81 GHz, 1.05 GHz, 2.43 GHz, 3.32 GHz, 5.20 GHz and 5.45 GHz. These simulated results are to resemble with the theoretical calculations. It is noticed that 7 resonance frequencies are appeared while one theoretically predicted resonant frequency 0.32 GHz of $n = -1$ mode is not observed. The difference between simulation and theoretical calculation may come from the parasitic effects by the mutual coupling between the elements in the

circuit. With S11 smaller than −6 dB, the proposed antenna exhibits four frequency bands: 0.773 – 0.836 GHz, 2.35 – 2.55 GHz, 3.05 – 3.71 GHz and 4.88 – 5.81 GHz. These frequency bands cover four standard bands including GSM810, WLAN 2.45/5.5 GHz and WiMAX 3.5 GHz bands. The fractional bandwidth of the antenna are found to be 7.78% for the first (0.81 GHz) band, 8.16% for the second (2.45 GHz) band, 18.86% for the third (3.5 GHz) band and 16.91% for the fourth (5.5 GHz) band.

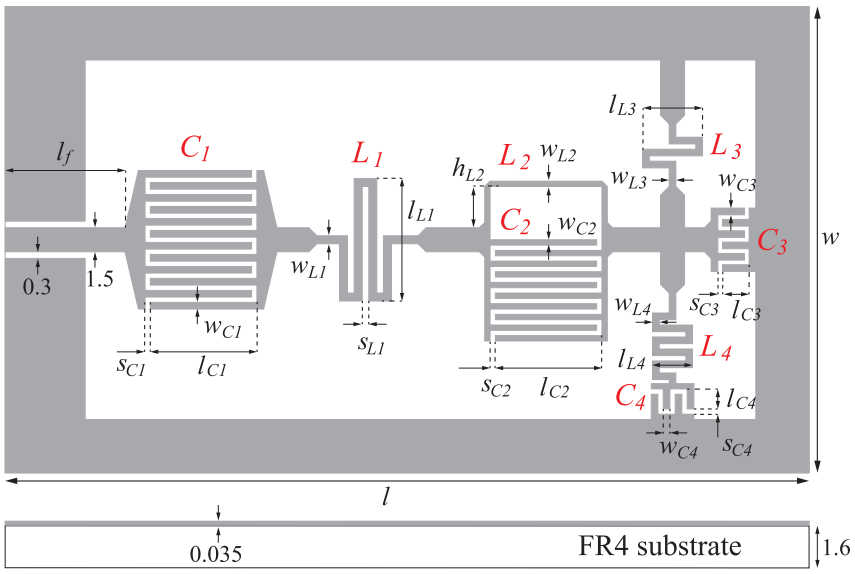

Figure 2.41: The configuration of the proposed antenna

Table 2.6: The dimensions of the proposed antenna

Parameter	Dimension	Parameter	Dimension
l	57.2 mm	s_{C2}	0.2 mm
w	31.2 mm	l_{L1}	8.8 mm
l_f	9.0 mm	w_{L1}	0.4 mm
l_{C1}	8.0 mm	s_{L1}	0.4 mm
s_{C1}	0.3 mm	l_{C2}	8.0 mm
w_{C1}	0.3 mm	w_{C2}	0.3 mm
w_{L2}	0.3 mm	l_{C4}	1.5 mm
h_{L2}	4.0 mm	w_{C4}	0.4 mm
l_{C3}	2.0 mm	s_{C4}	0.2 mm
w_{C3}	0.4 mm	l_{L4}	2.6 mm
s_{C3}	0.2 mm	w_{L4}	0.3 mm
l_{L3}	4.3 mm	w_{L3}	0.4 mm

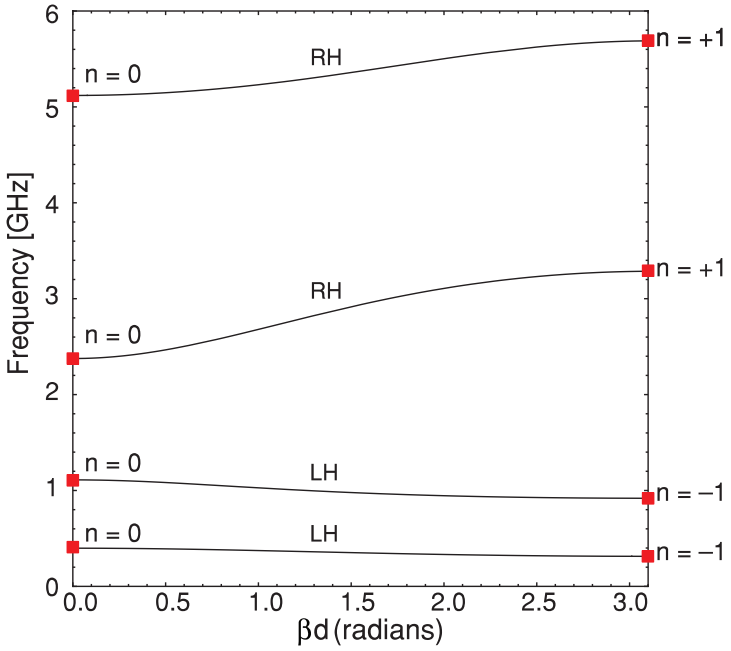

Figure 2.42: Dispersion diagram of the proposed asymmetric E-CRLH unit cell

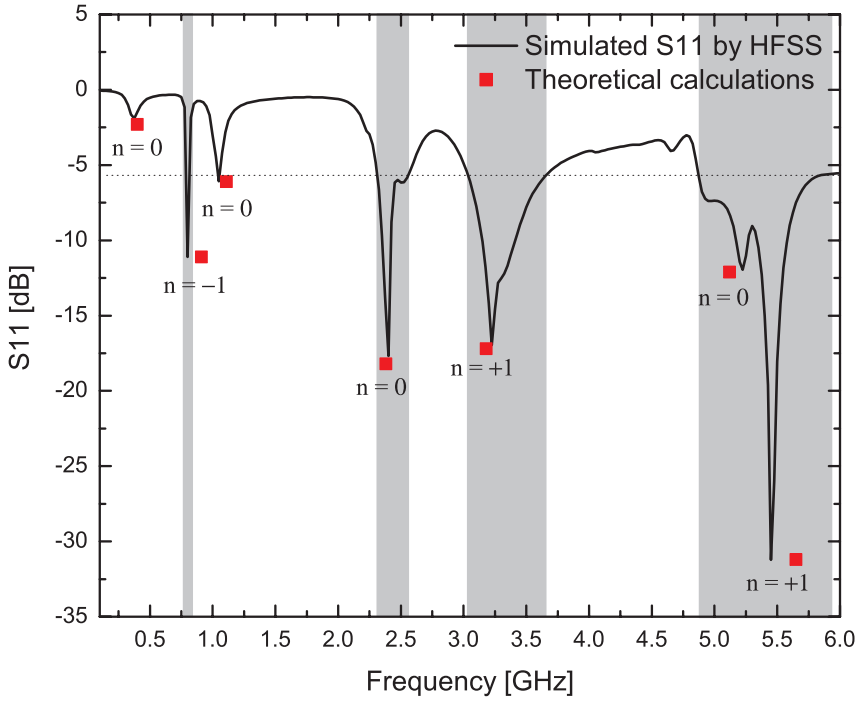

Figure 2.43: S11 characteristics of the proposed antenna

2.3.3 Fabrication, measurement results and discussions

A photograph of the fabricated antenna is shown in Fig. 2.44. Figure 2.45 presents the measured return loss S11 of the antenna from 0.5 to 6 GHz. The measurements are executed by Agilent E8361A network analyzer in an anechoic chamber and compared with the corresponding HFSS simulated results.

The first band (GSM810) and the second band (WLAN 2.45 GHz) have been shifted by 50 MHz and 120 MHz, respectively. At the third band (WiMAX 3.5 GHz) and the fourth band (WLAN 5.5 GHz), the measured bandwidth is slightly wider than the simulated bandwidth. The normalized radiation patterns of the antenna at different frequencies are shown in Figs. 2.46 and 2.47. As can be seen from Fig. 2.46, the measured radiation patterns at 0.81 GHz and 2.45 GHz are not so good to compare with the simulated ones as a result of the shifting of the resonant frequency of GSM810 and WLAN 2.45 GHz bands. Nevertheless, the measured radiation patterns at these frequencies show the omnidirectional radiation patterns which are suitable for wireless communications. At WiMAX 3.5 GHz and WLAN 5.5 GHz bands, a better agreement can be observed between the measured radiation patterns and the simulated ones at 3.5 GHz and 5.5 GHz in Fig. 2.47. The shifting frequency in S11 and the difference between the simulated and measured radiation patterns may come from the unstable FR4 substrate parameters and the manufacturing tolerance of the antenna dimensions. In addition, the SMA connector also affects to the measured results because of the connection loss between the board and the SMA connector. The gains of the proposed antenna are estimated as 3.66 dBi at 5.5 GHz, 1.46 dBi at 3.5 GHz, -1.31 dBi at 2.45 GHz and -8.12 dBi at 0.81 GHz. Due to the compact size, the gains of the antenna are quite low at low frequencies.

Table 2.7 summarizes the recently reported works about quad-band antennas including our design. Our quad-band antenna has an electrical size $0.15\lambda_0 \times 0.08\lambda_0$ at the center frequency (0.805 GHz) of the lowest band (GSM810) and its size is very small to compare with the other antennas [23]–[30] which designed by conventional methods. Although Reference [42] has made from the E-CRLH unit cell, our antenna can be designed by roughly one half size. The antenna in Ref. [44] has a similar electrical size with the proposed antenna, but that design used a thicker FR4 substrate.

It is found that the proposed antenna has low gain for low frequency bands. This characteristic is typical for electrically small antennas. At the higher frequencies, the gains of the antenna are enhanced and comparable with the previous quad-band antennas. In addition, the proposed antenna has a better gain at the low frequencies than the reported dual-band NRI-TL antenna (-17 dBi at 0.9 GHz and -8 dBi at 2.4 GHz) in Ref. [41].

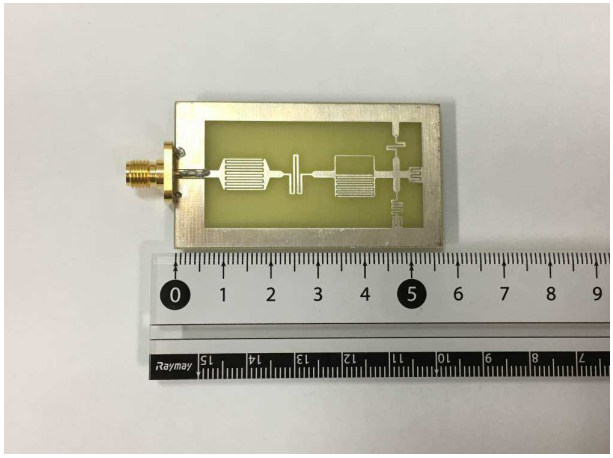

Figure 2.44: Fabricated antenna

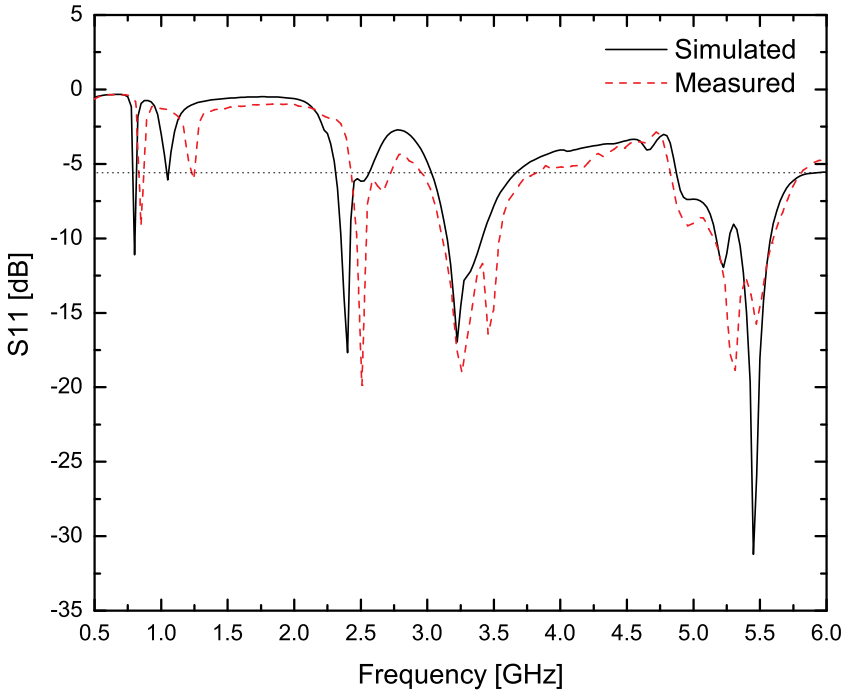

Figure 2.45: S11 characteristics of the fabricated antenna

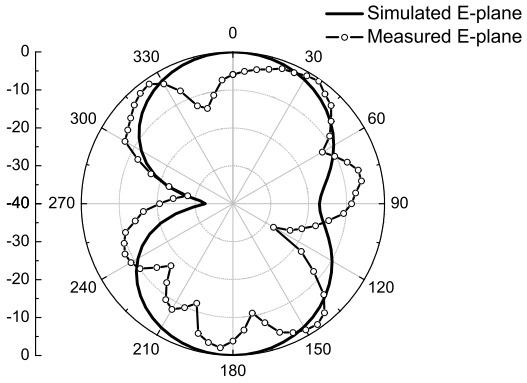

(a)

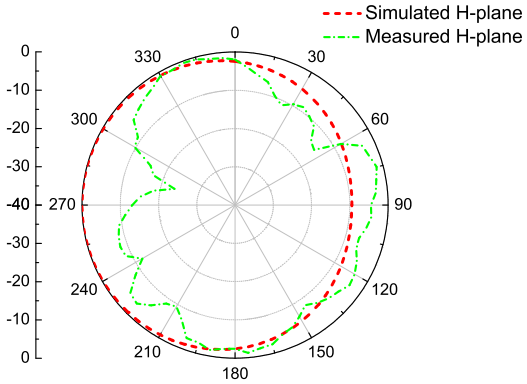

(b)

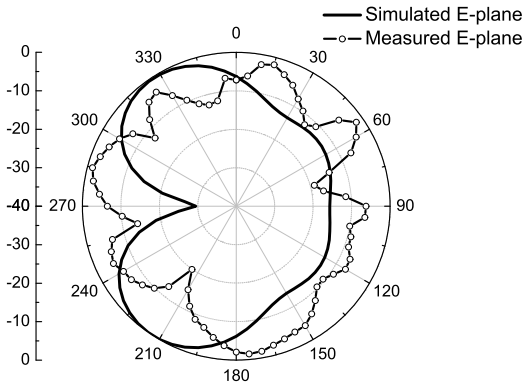

(c)

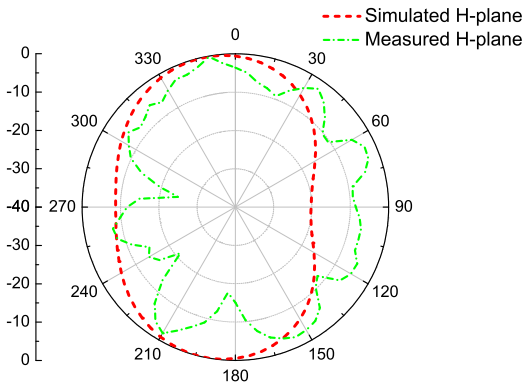

(d)

Figure 2.46: Normalized radiation patterns at different frequencies. (a) E-plane at 0.81 GHz, (b) H-plane at 0.81 GHz, (c) E-plane at 2.45 GHz, (d) H-plane at 2.45 GHz

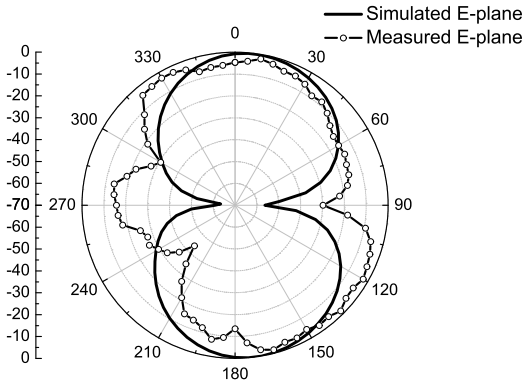

(a)

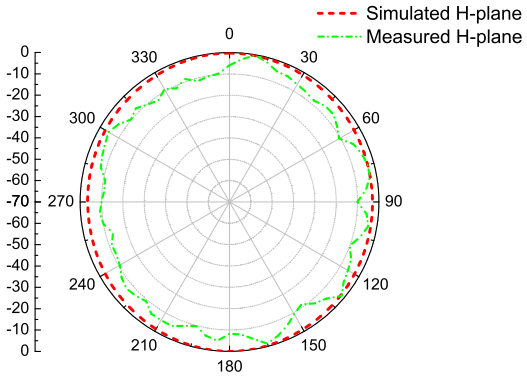

(b)

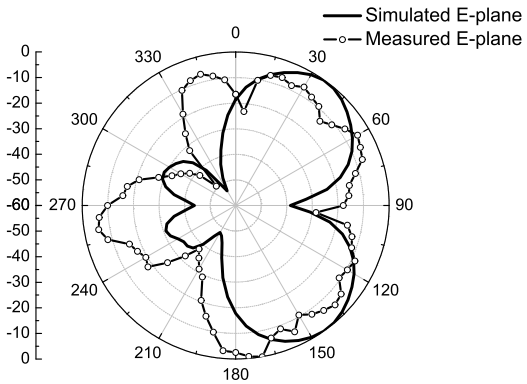

(c)

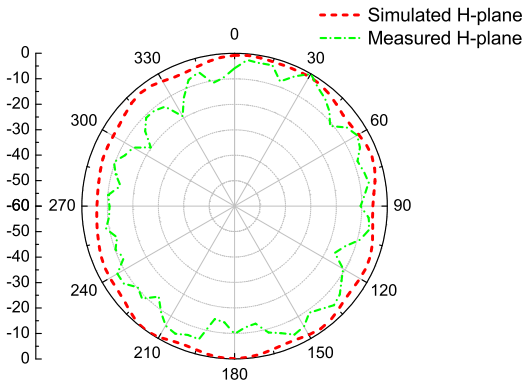

(d)

Figure 2.47: Normalized radiation patterns at different frequencies. (a) E-plane at 3.5 GHz, (b) H-plane at 3.5 GHz, (c) E-plane at 5.5 GHz, (d) H-plane at 5.5 GHz.

Table 2.7: The comparison with the previously proposed quad-band antennas

Ref. Year	Size [mm×mm]	Electrical size by lowest band	Operating bands [GHz]	Gain [dBi]	Substrate, parameters	Design methods
Ours 2017	57.2×31.2	$0.15\lambda_0 \times 0.08\lambda_0$, $\lambda_0 = 373$ mm	0.773–0.836, 2.35–2.55, 3.05–3.71, 4.88–5.81	−8.12, −1.31, 1.46, 3.66	FR4 substrate, ε_r=4.4, $\tan\delta$=0.02, h=1.6 mm.	E-CRLH unit cell, CPW.
[42] 2017	64×56	$0.19\lambda_0 \times 0.17\lambda_0$, $\lambda_0 = 338$ mm	0.862–0.912, 1.75–2.69, 3.40–3.69, 4.4–6.0	−3.38, 1.5, 1.6, 3.8	Rogers 5880, ε_r=2.2, $\tan\delta$=0.0009, h=1.575 mm.	E-CRLH unit cell, Microstrip line.
[25] 2015	56×44	$0.30\lambda_0 \times 0.24\lambda_0$, $\lambda_0 = 185$ mm	1.575–1.665, 2.4–2.545, 3.27–3.97, 5.17–5.93	3.55, 3.93, 5.02, 4.86	ε_r=3.5, $\tan\delta$=0.004, h=0.8 mm.	T-shaped stubs, E-shaped stubs, Microstrip line.
[29] 2015	90×60	$0.32\lambda_0 \times 0.21\lambda_0$, $\lambda_0 = 280$ mm	0.94–1.20, 2.23–2.43, 3.58–3.74, 4.93–5.29	5.47, 5.88, 1.97, 3.56	Flexible Rogers 5880, ε_r=2.2,$\tan\delta$=0.0009, h=0.127 mm.	Pentangle-loop radiator, CPW.
[44] 2013	31×21	$0.13\lambda_0 \times 0.09\lambda_0$, $\lambda_0 = 236$ mm	1.25–1.28, 2.44–2.73, 3.17–3.82, 5.03–6.16	−4.88, 2.82, 1.84, 1.78	FR4 substrate, ε_r=4.4, $\tan\delta$=0.02, h=2.0 mm.	CRLH unit cell, Meander monopole, CPW.
[26] 2012	42×36	$0.23\lambda_0 \times 0.19\lambda_0$, $\lambda_0 = 185$ mm	1.54–1.70, 2.38–2.76, 3.20–3.77, 5.12–6.25	1.84, 1.81, 2.03, 2.80	FR4 substrate, ε_r=4.4, h=1.0 mm.	Wide slots, Microstrip line.
[27] 2012	25×20	$0.20\lambda_0 \times 0.16\lambda_0$, $\lambda_0 = 124$ mm	2.07–2.77, 3.30–3.80, 5.15–5.35, 5.70–5.89	2.6, 2.0, 3.2, 2.9	FR4 substrate, ε_r=4.4, h=1.6 mm.	L-shaped slot, Rectangular slot, CPW.
[24] 2011	60×53	$0.32\lambda_0 \times 0.28\lambda_0$, $\lambda_0 = 190$ mm	1.525–1.625, 2.332–2.495, 3.42–3.7, 5.05–5.94	−1.0, 3.25, 2.0, 4.5	FR4 substrate, ε_r=2.7, $\tan\delta$=0.02, h=0.8 mm.	Circular slots, Concave slot, Microstrip line.
[23] 2011	30×30	$0.14\lambda_0 \times 0.14\lambda_0$, $\lambda_0 = 218$ mm	1.17–1.58, 2.4–2.70, 3.40–3.69, 4.70–5.50	0.51, 1.41, 2.68, 2.98	FR4 substrate, ε_r=4.4, $\tan\delta$=0.02, h=1.6 mm.	Invert-C slots, Invert-F strips, Microstrip line.
[28] 2011	86×62	$0.26\lambda_0 \times 0.19\lambda_0$, $\lambda_0 = 335$ mm	0.86–0.93, 1.69–1.73, 2.18–2.23, 2.67–2.73	1.0∼4.0	FR4 substrate, ε_r=4.7, h=0.78 mm.	Rectangular fractal, Microstrip line.
[30] 2009	52×49	$0.15\lambda_0 \times 0.14\lambda_0$, $\lambda_0 = 345$ mm	0.868–0.870, 1.225–1.227, 1.71–1.99, 2.40–2.48	N/A	Arlon substrate, ε_r=3.38, $\tan\delta$=0.002, h=0.8 mm.	Hilbert shapes, Microstrip line.

Chapter 3

Resonant metamaterials

3.1 Robust method to retrieve effective parameters of resonant metamaterials from S-parameters

3.1.1 Introduction

In frequency domain, all materials can be described by their complex electromagnetic properties including refractive index n, impedance z, permittivity ε and permeability μ. These electromagnetic properties are is very important for RF and microwave applications since they respond to electromagnetic radiation of materials. To determine unique electromagnetic properties of metamaterials, a retrieval method based S-parameters is used in this study.

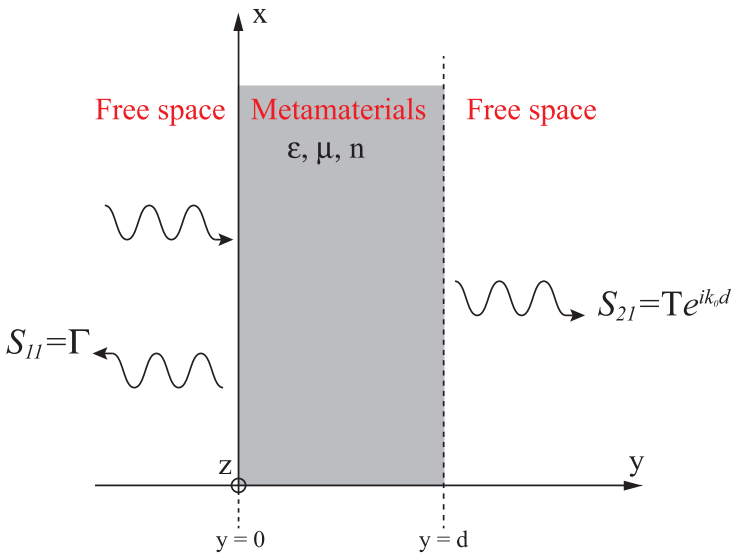

Figure 3.1: S-parameters on both sides of an 1D metamaterial slab

A metamaterial slab is placed in free space as shown in Fig. 3.1. A variety of reflection S_{11} and transmission S_{21} results are given for the scattering of normally incident plane waves from a material slab in free space. In order to retrieve the refractive index n, impedance z, permittivity ε and permeability μ of this metamaterial slab, we need to characterize it as an effective homogeneous slab. The data of S_{11} and S_{21} will be extracted from HFSS, which is commercially Finite Element Method (FEM) based full wave simulator. Before using simulated S-parameter data, normal incidence of plane wave on a homogeneous slab in free space should be investigated.

3.1.2 Normal incidence of plane wave on a homogeneous slab in free space

The problem geometry is depicted in Fig. 3.2. Let assume that a plane wave is traveling in the $+y$ direction. The incident electric field is assumed to be the $+x$ direction while the incident magnetic field is in the $-z$ direction. An infinite length homogeneous slab of thickness d is placed between the $z = 0$ and $z = d$ planes in free space.

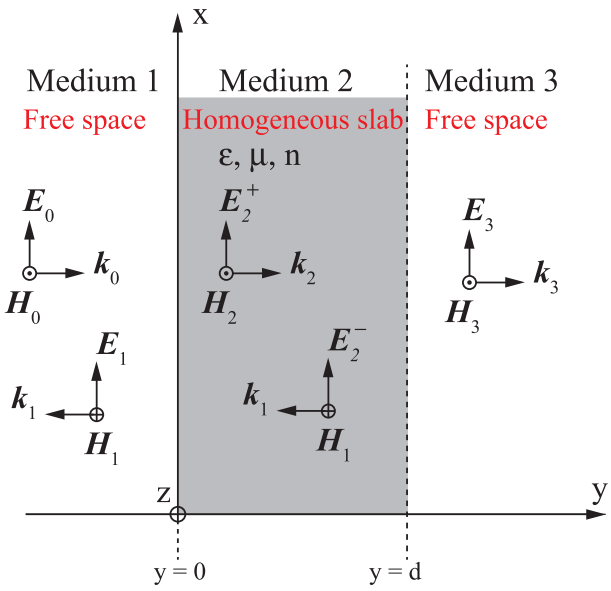

Figure 3.2: A plane wave normally incident on a homogeneous slab

In Medium 1, the incident waves $(\boldsymbol{E}^i, \boldsymbol{H}^i)$ and the reflected waves $(\boldsymbol{E}^r, \boldsymbol{H}^r)$ are

$$\boldsymbol{E}^i = E_0 \hat{\boldsymbol{x}} e^{ik_0 y}, \tag{3.1}$$

$$\boldsymbol{H}^i = -\frac{E_0}{Z_0} \hat{\boldsymbol{z}} e^{ik_0 y}, \tag{3.2}$$

$$\boldsymbol{E}^r = E_1 \hat{\boldsymbol{x}} e^{-ik_0 y}, \tag{3.3}$$

$$\boldsymbol{H}^r = -\frac{E_1}{Z_0} \hat{\boldsymbol{z}} e^{-ik_0 y}, \tag{3.4}$$

where k_0 denotes the wave number of the incident wave in free space.

In Medium 2, one gets the total electric and magnetic fields as

$$\boldsymbol{E}^m = E_2^+ \hat{\boldsymbol{y}} e^{ink_0 y} + E_2^- \hat{\boldsymbol{y}} e^{-ink_0 y}, \tag{3.5}$$

$$\boldsymbol{H}^m = -\frac{E_2^+}{Z} \hat{\boldsymbol{z}} e^{ink_0 y} + \frac{E_2^-}{Z} \hat{\boldsymbol{z}} e^{-ink_0 y}, \tag{3.6}$$

where n is the refractive index in the homogeneous slab.

In Medium 3, the transmitted wave are

$$\boldsymbol{E}^t = E_3 \hat{\boldsymbol{x}} e^{ik_0 y}, \tag{3.7}$$

$$\boldsymbol{H}^t = -\frac{E_3}{Z_0} \hat{\boldsymbol{z}} e^{ik_0 y}. \tag{3.8}$$

By applying the boundary condition at $y = 0$ and $y = d$, we have

$$E_0 + E_1 = E_2^+ + E_2^-, \tag{3.9}$$

$$\frac{E_0}{Z_0} - \frac{E_1}{Z_0} = \frac{E_2^+}{Z} - \frac{E_2^-}{Z}, \tag{3.10}$$

$$E_2^+ e^{ink_0 y} + E_2^- e^{-ink_0 y} = E_3 e^{ik_0 y}, \tag{3.11}$$

$$\frac{E_2^+}{Z} e^{ink_0 y} - \frac{E_2^-}{Z} e^{-ink_0 y} = \frac{E_3}{Z_0} e^{ik_0 y}. \tag{3.12}$$

For convenience, we introduce the variable $z = Z/Z_0$ which is the impedance relatively to free space, then Eqs. (3.10) and (3.12) become

$$zE_0 - zE_1 = E_2^+ - E_2^-, \tag{3.13}$$

$$E_2^+ e^{ink_0 y} - E_2^- e^{-ink_0 y} = zE_3 e^{ik_0 y}. \tag{3.14}$$

From Eq. (3.9) and Eq. (3.13), one gets

$$2E_2^+ = (z+1)E_0 - (z-1)E_1, \tag{3.15}$$

$$2E_2^- = -(z-1)E_0 + (z+1)E_1. \tag{3.16}$$

From Eq. (3.11) and Eq. (3.14), we have

$$2E_2^+ e^{ink_0 y} = (z+1)E_3 e^{ik_0 y}, \tag{3.17}$$

$$2E_2^- e^{-ink_0 y} = -(z-1)E_3 e^{ik_0 y}. \tag{3.18}$$

From Eqs. (3.15), (3.16), (3.17) and (3.18), one gets

$$(E_0 - R_{01}E_1)e^{ink_0y} = E_3e^{ik_0y}, \tag{3.19}$$

$$(E_0 - \frac{E_1}{R_{01}})e^{-ink_0y} = E_3e^{ik_0y}, \tag{3.20}$$

where

$$R_{01} = \frac{z-1}{z+1}. \tag{3.21}$$

Finally, the reflection coeficient Γ and the transmission coefficient T are calculated from Eqs. (3.19) and (3.20)

$$\Gamma = \frac{E_1}{E_0} = \frac{R_{01}(1-e^{i2nk_0d})}{1-R_{01}^2e^{i2nk_0d}}, \tag{3.22}$$

$$T = \frac{E_3}{E_0} = \frac{(1-R_{01}^2)e^{i(n-1)k_0d}}{1-R_{01}^2e^{i2nk_0d}},. \tag{3.23}$$

3.1.3 Theoretical retrieval equations for resonant metamaterials

Since S_{11} is equal to the reflection coefficient Γ, and S_{21} is related to the transmission coefficient T by $S_{21} = Te^{ik_0d}$, the S-parameters are related to refractive index n and impedance z by:

$$S_{11} = \frac{R_{01}(1-e^{i2nk_0d})}{1-R_{01}^2e^{i2nk_0d}}, \tag{3.24}$$

$$S_{21} = \frac{(1-R_{01}^2)e^{ink_0d}}{1-R_{01}^2e^{i2nk_0d}}. \tag{3.25}$$

By inverting Eqs. (3.24) and (3.25), the impedance z and the refractive index n can be directly applied in the case of a homogeneous slab. However, a metamaterial itself is not homogeneous, the calculations for z and n should be carefully considered. As it has been pointed out in [45], the refractive index n and impedance z are obtained as

$$z = \pm\sqrt{\frac{(1+S_{11})^2 - S_{21}^2}{(1-S_{11})^2 - S_{21}^2}}, \tag{3.26}$$

$$e^{ink_0d} = \frac{S_{21}}{1 - S_{11}\dfrac{z-1}{z+1}}. \tag{3.27}$$

We are working with a passive medium. Therefore, the following conditions are required

$$\mathrm{Re}[z] \geq 0, \tag{3.28}$$

$$\mathrm{Im}[n] \geq 0. \tag{3.29}$$

In fact, z and n are related so that their relation ship can be used to determine the correct sign of z in Eq. (3.26). Two cases are distinguished in order to correctly find the sign of z. The first case is for $|\,\mathrm{Re}[z]| \geq \delta$ where δ is a positive number and for which $\mathrm{Re}[z] \geq 0$. In the second case, the sign of z is chosen so that the corresponding $\mathrm{Im}[n] \geq 0$, or equivalent $|e^{ink_0d}| \leq 1$. The value of refractive index n can be determined from Eq. (3.27) as

$$n = \frac{1}{k_0 d}\{\mathrm{Im}[\ln(e^{ink_0d})] + 2m\pi\} - \frac{i}{k_0 d}\{\mathrm{Re}[\ln(e^{ink_0d})]\}, \tag{3.30}$$

where m is an integer related to the branch index of $\mathrm{Re}[n]$. As can be seen from Eq. (3.30), $\mathrm{Im}[n]$ can be calculated without any problems, but we must resolve the branching problem to determine the correct $\mathrm{Re}[n]$. To ensure the refractive index function is smooth and continuous, one may use Taylor series to calculate the branch index of $\mathrm{Re}[n]$ as shown in Ref. [45]. Finally, The permittivity ε and the permeability μ are related to the refractive index and impedance by the following expressions:

$$\varepsilon = \frac{n}{z}, \tag{3.31}$$

$$\mu = nz. \tag{3.32}$$

By using the retrieval equations, the electromagnetic properties (z, n, ε and μ) of a conventional Split Ring Resonator (SRR) and a thin wire as shown in Fig. 3.3 are calculated to check the procedure. The copper SRR is placed in the top of the FR4-substrate while the copper thin wire is positioned in the bottom of the FR4-substrate. The dimensions of the sample is chosen similarly with Ref. [46] and shown in Table 3.1.

The proposed sample is to setup and simulate in HFSS simulator with frequency range from 1 to 20 GHz. Figure 3.4 show the magnitude and phase of the simulated S-parameters. The dip in the phase of S_{21} indicates the presence of a negative index band. The retrieved index n and impedance z is shown in Fig. 3.5. It is observed that the negative index band is between 9 and 12 GHz. In addition, $\mathrm{Re}[z]$ and $\mathrm{Im}[n]$ satisfy the conditions in Eqs. (3.28) and (3.29) to confirm the consideration of the passive medium. Using Eqs. (3.31) and (3.32), we find out the permittivity and the permeability from the impedance and index as shown in Fig. 3.6.

In general, these calculated results are the same with those in Fig. 3 of Ref. [46].

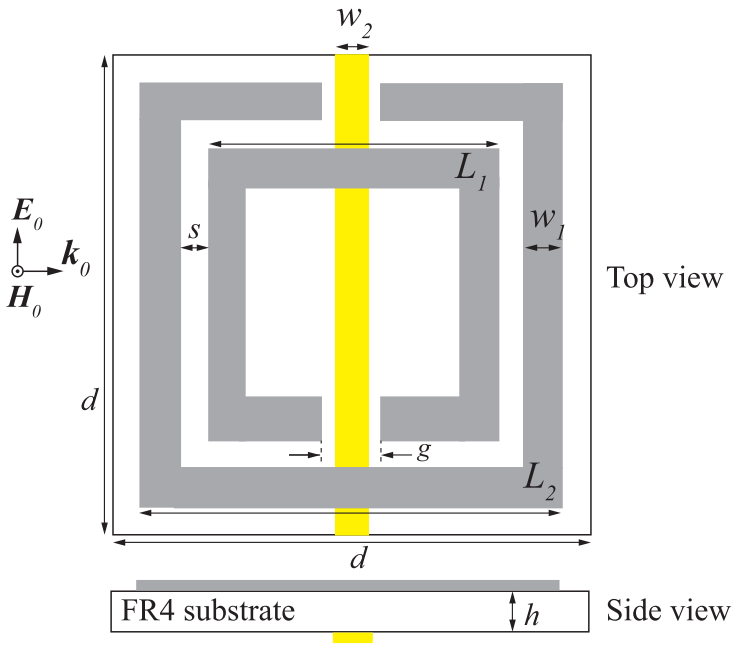

Figure 3.3: The configuration of a conventional SRR with a thin wire unit cell

Table 3.1: The dimensions of the proposed SRR unit cell

Parameter	Dimension
d	2.50 mm
h	0.25 mm
w_1	0.30 mm
w_1	0.20 mm
w_2	0.14 mm
L_1	1.50 mm
L_2	2.20 mm
g	0.25 mm
s	0.15 mm

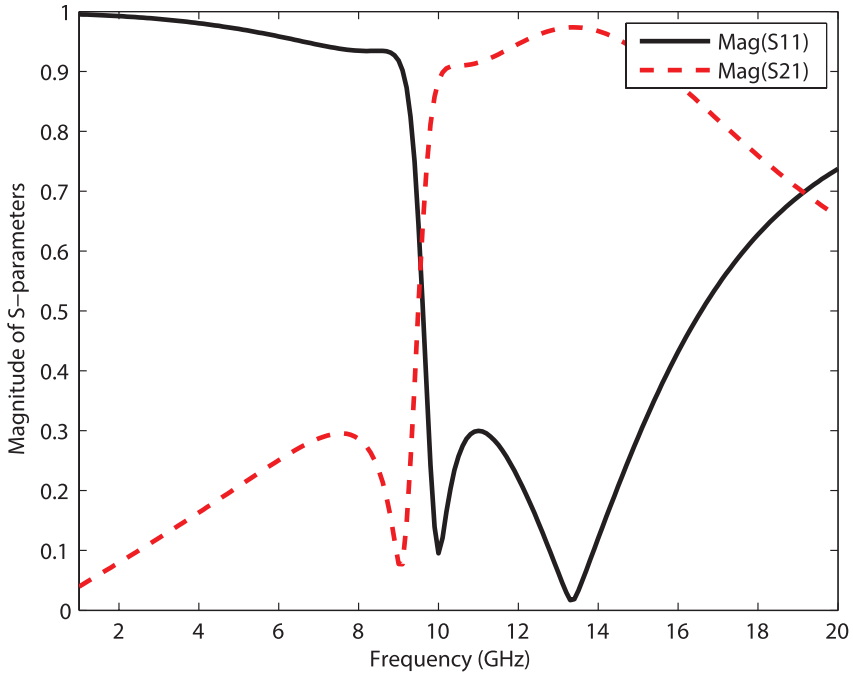

(a)

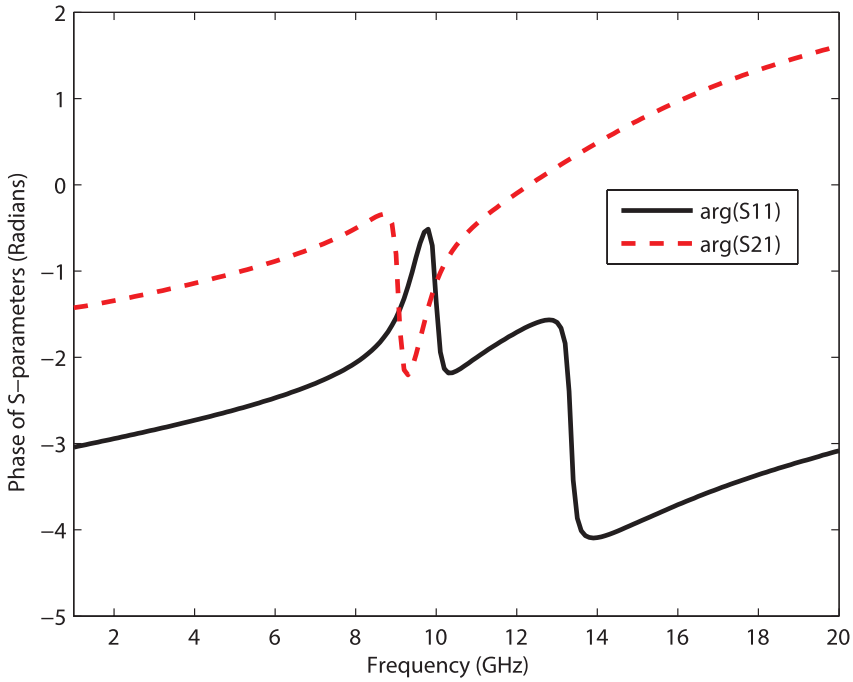

(b)

Figure 3.4: Simulated S-parameters for the proposed unit cell with the dimension in Table 3.1. (a) Magnitude (b) Phase.

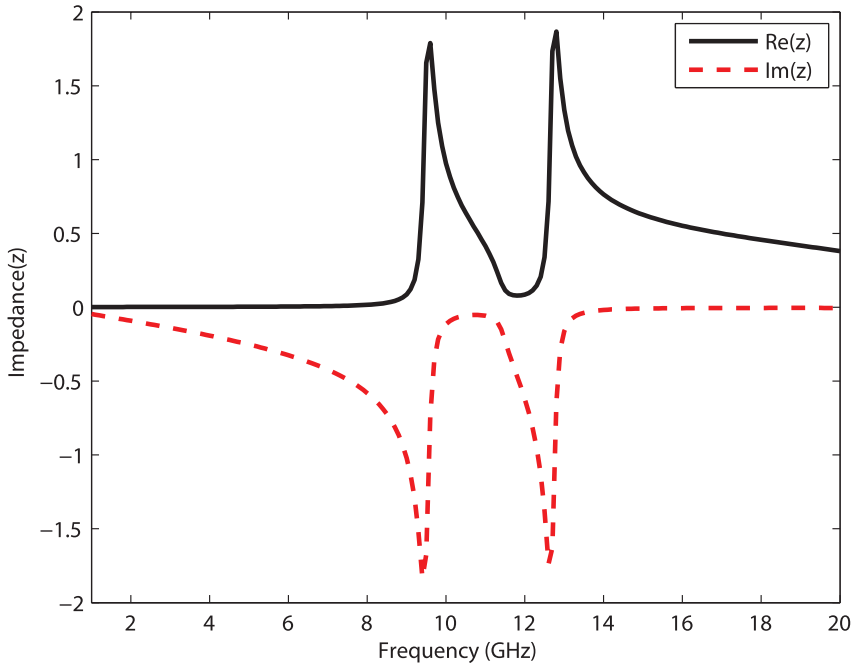

(a)

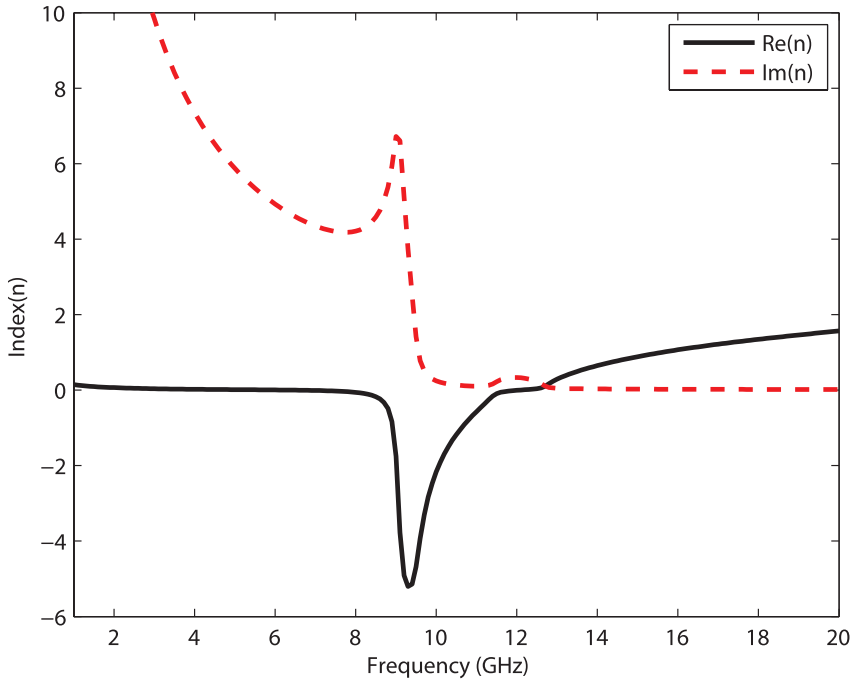

(b)

Figure 3.5: Retrieved parameters of the metamaterial unit cell (a) Impedance (b) Refractive index

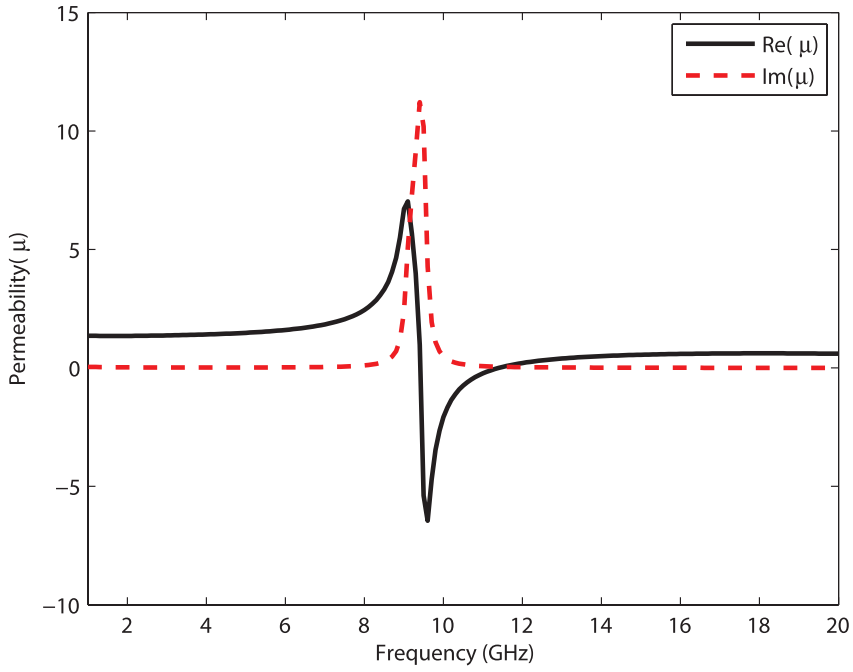

(a)

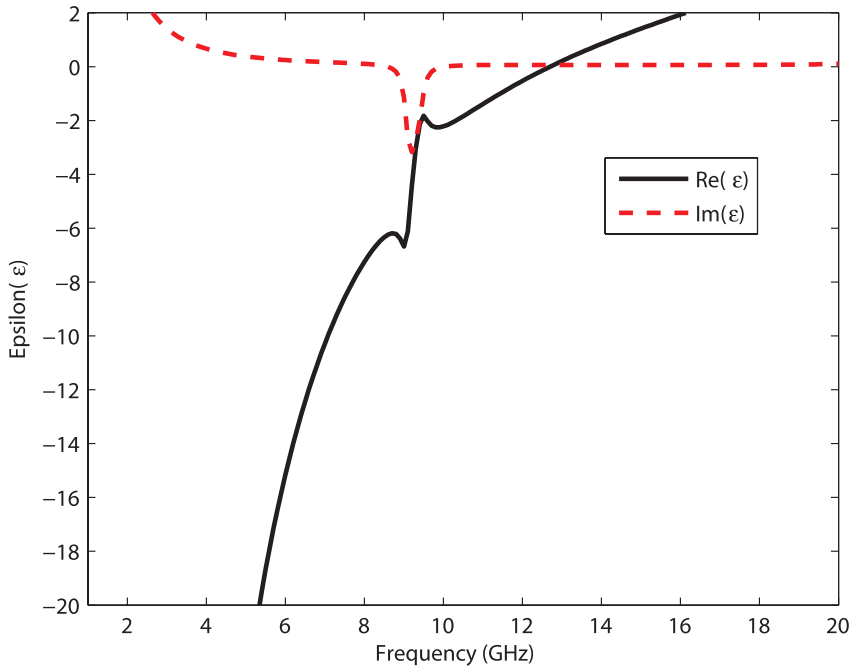

(b)

Figure 3.6: Retrieved parameters of the metamaterial unit cell (a) Permeability (b) permittivity

3.2 Zero-index metamaterial (ZIM) unit cell for improving gain of antipodal Vivaldi antenna

3.2.1 Introduction

Recently wireless communication using the ultra wideband (UWB) has expanded rapidly, since the United States Federal Communication Commission nominated the frequency band of 3.1 to 10.6 GHz for the UWB operation [47]. Many kinds of UWB antennas have been designed such as bow-tie, conical, TEM horn, spiral, fractal, and log-periodic antennas. The Vivaldi antenna is one of the classic UWB antennas with many advantages. It was first investigated by P. Gibson in 1979 [48]. Many studies including two remarkable improvements [49, 50] have been reported since then.

The antipodal type of Vivaldi antennas offers broad bandwidth, minimal signal distortion, and high gain properties. However, the operation mechanism of the antipodal Vivaldi antenna is not well understood. Previously, antipodal Vivaldi antennas have been mainly designed by empirical methods without rigorous theory or formulas [51]–[56]. While the operational upper frequency end of the antipodal Vivaldi antenna is theoretically infinity, the low frequency end has not been predicted and explained clearly. Therefore, the first objective of this study are to get better insight on the operation of the antipodal Vivaldi antennas, and to develop an accurate estimation of the low frequency end of the operational range.

In addition, the gain of the antipodal Vivaldi antenna is a very important parameter for UWB applications. Therefore, there many studies have been carried out to enhance the gain of the Vivaldi antenna. Some methods have been proposed to improve the gain of Vivaldi antennas by making corrugated structure at the edges of the Vivaldi antenna [57]–[63]. These improvements are obtained at the cost of the change in the antenna configuration and at a narrow band of the enhanced gain. By adding a high permittivity dielectric [64, 65, 66] and a parasitic elliptical patch [67] as a director in the aperture of the Vivaldi antenna, a stronger radiation in the end-fire direction is observed. However, they elongate the antenna length to much for some applications. Another research [68] loads a hemisphere len in front of the antenna. This kind of lens increases the complexity and the cost for fabrication and combination with the monolithic integrated circuits. Hence, the second objective of this study is to enhance the gain of the antipodal Vivaldi antenna by using resonant metamaterials. A simple symmetric zero-index metamaterial (ZIM) unit cell is proposed. The ZIM unit cells are arranged to the aperture of antipodal Vivaldi antenna to make a stronger end-fire radiation.

This study content is organized as follows. Basic antipodal Vivaldi antenna design has been analytically first in Section 3.2.2 and detail specification has been adjusted by simulation software. New estimation for low frequency end of the antipodal Vivaldi antenna will be discussed in Section 3.2.3. The antenna and its performance has been presented in Section 3.2.4. Finally, gain improvement of the antipodal Vivaldi antenna with ZIM unit cells are made in Section 3.2.5.

3.2.2 Antipodal Vivaldi antenna design

The geometry of the antipodal Vivaldi antenna is shown in Fig. 3.7. This antenna is constituted by two main parts: a feeding line and radiation flares. Previously proposed Vivaldi antennas are mostly installed on the PEC grounded substrate with a microstrip line. In order to have a smooth transition between the feeding line and radiation flares, and to keep a symmetric structure, microstrip twin lines are chosen here for the feeder. These twin lines apparently serve as an impedance matching circuit between an input connector and the radiation flares, so that the characteristic impedance of twin lines may not be 50 Ω.

The characteristic impedance Z_0 of twin lines may be calculated from the corresponding characteristic impedance $\overline{Z}_0$ of a single microstrip line on the PEC grounded structure. Using the image theory, $Z_0(h, \varepsilon_r)$ on the substrate of the thickness h and the relative dielectric constant ε_r can be obtained from $\overline{Z}_0(h, \varepsilon_r)$ as

$$Z_0(h, \varepsilon_r) = 2\overline{Z}_0(h/2, \varepsilon_r), \tag{3.33}$$

where $\overline{Z}_0(h, \varepsilon_r)$ may be found from the following approximation [18]:

$$\overline{Z}_0(h, \varepsilon_r) = \frac{120\pi}{\sqrt{\varepsilon_e}} \left[\frac{w_f}{h} + 1.393 + 0.667 \ln\left(\frac{w_f}{h} + 1.444\right)\right]^{-1} \tag{3.34}$$

for $w_f \geq h$,

$$\overline{Z}_0(h, \varepsilon_r) = \frac{60}{\sqrt{\varepsilon_e}} \ln\left(\frac{8h}{w_f} + \frac{w_f}{4h}\right) \tag{3.35}$$

for $w_f \leq h$, and the effective dielectric constant ε_e is given by

$$\varepsilon_e = \frac{\varepsilon_r + 1}{2} + \frac{\varepsilon_r - 1}{2}\left(1 + \frac{12h}{w_f}\right)^{-1/2}. \tag{3.36}$$

To design radiation flares, many authors have used exponential curves [58]–[60], [69]–[72] or Fermi-Dirac curves [57]. Here, somewhat simpler ellipse profiles are used for flare

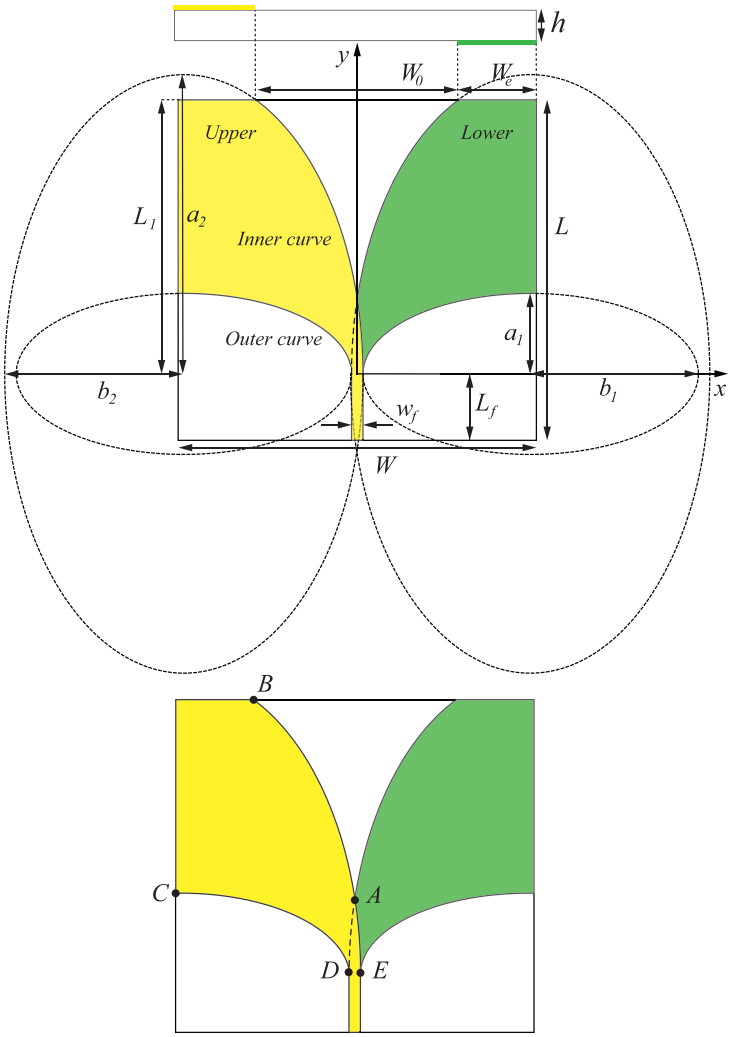

Figure 3.7: Antenna geometry

curves [51], [55], [73]–[75]. These curves are chosen here since the elliptical configuration is simple and it presents the smooth transition between the feeding line and the radiation flares. As shown in Fig. 3.7, each flare is composed by two ellipses of semi-major axis b_1, a_2 and semi-minor axis a_1, b_2, respectively, and is connected to the feeder of the width w_f as

$$b_2 = b_1 + w_f, \tag{3.37}$$

$$r_1 = \frac{a_1}{b_1}, \tag{3.38}$$

$$r_2 = \frac{a_2}{b_2}. \tag{3.39}$$

The axial ratios r_1 and r_2 are used to describe the curvature of the antipodal structure. Then the elliptical profile (x_i, y_i) and (x_o, y_o) of inner and outer lines for the upper surface

employed in this design can be described by the following equations:

$$y_i = r_2\sqrt{b_2^2 - \left\{x_i + (b_2 - w_f/2)\right\}^2}, \tag{3.40}$$

for $-W_0/2 \leq x_i \leq w_f/2$ and

$$y_o = r_1\sqrt{b_1^2 - \left\{x_o + (b_1 + w_f/2)\right\}^2}, \tag{3.41}$$

for $-W/2 \leq x_o \leq w_f/2$. Similar equations may be found for the axially symmetric curve on the lower surface.

The antipodal Vivaldi antenna may be easily made from a low-cost double-sided copper coated FR4 substrate with the thickness of the substrate $h = 1.6$ mm, the thickness of the copper $t = 18$ μm. The relative dielectric constant ε_r and the dielectric loss tangent δ of the utilized substrate could be frequency dispersive in general, but are found to be almost constant as $\varepsilon_r = 4.4$ and $\tan\delta = 0.03$ for the designed UWB frequency range by the measurement. First, the dimension of the antenna width W was initially selected to be one wavelength (100 mm) of the low frequency end (3 GHz). Then the width w_f (=3.2 mm) and length L_f (=18.54 mm) were chosen to get a better impedance matching with the input impedance 50 Ω by the High Frequency Structure Simulator (HFSS) for the extended UWB frequency range (2−15 GHz). Simulated magnitude of S_{11} with different width W is plotted in Fig. 3.8.

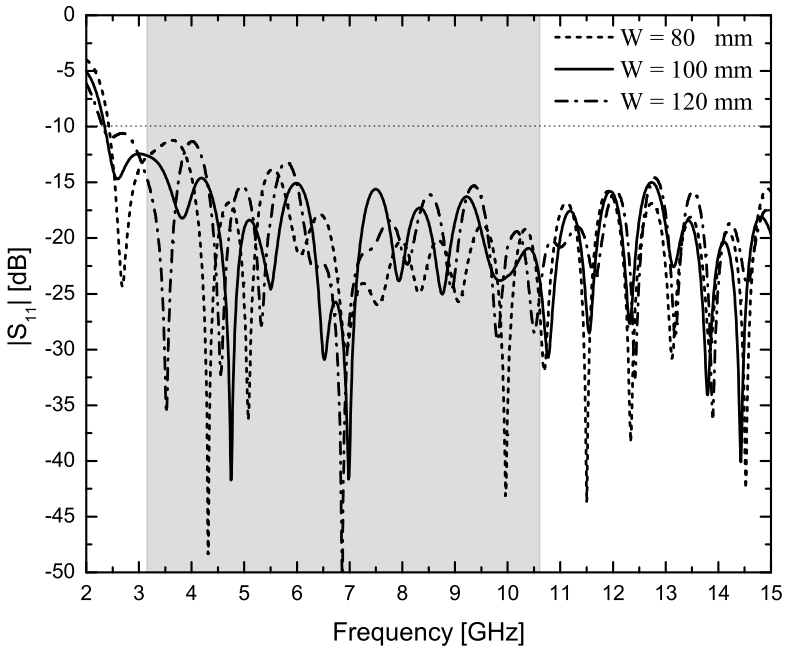

Figure 3.8: $|S_{11}|$ for different W

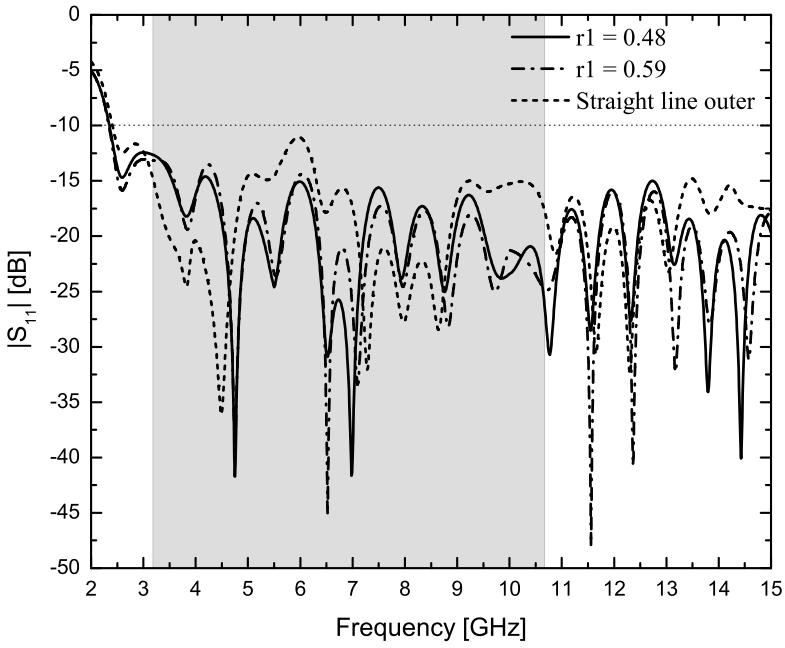

Figure 3.9: $|S_{11}|$ for different r_1

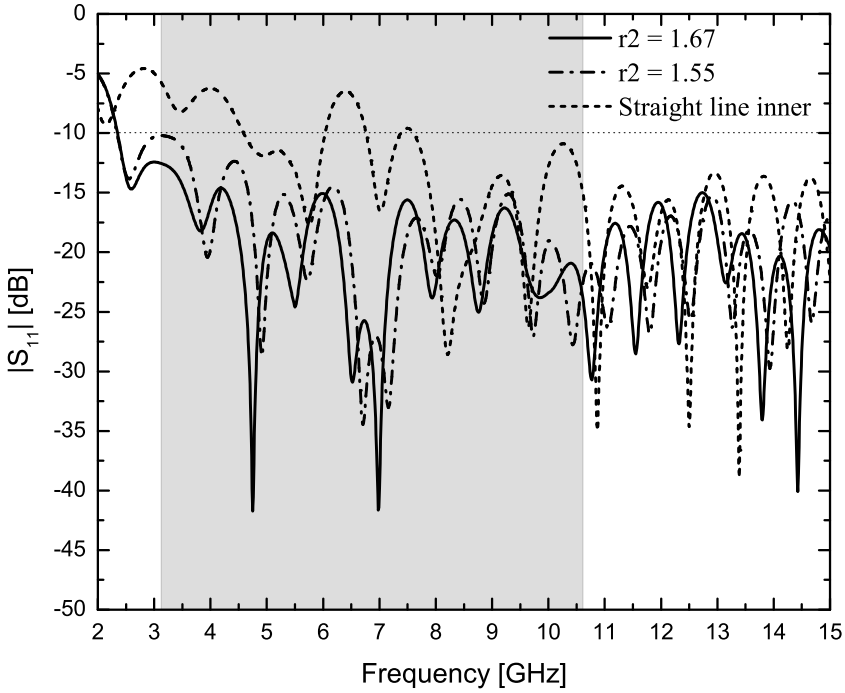

Figure 3.10: $|S_{11}|$ for different r_2

The shading area in the following figures denotes the frequency range for the UWB operation. The effect of the width W seems to be small, but the case $W = 100$ mm is the best among the cases for $W = 80, 100, 120$ mm. One may define the operational frequency range from $|S_{11}| \leq -10$ dB. While the antenna has the low frequency end f_- at 2.36 GHz from Fig. 3.8, it works superbly for high frequency and does not have the high frequency end f_+. This characteristic is typical for Vivaldi antennas [48].

The simulated $|S_{11}|$ with different curvatures of the outer curve are plotted in Fig. 3.9. $|S_{11}|$ does not change much, even the outer curve is a straight line which connects between points C and D for $r_1 = 0.48$. This suggests that the outer curve of the flares does not affect too much for the S_{11} parameter. The significant change occurs for changing the inner curve of the flares, and some results are shown in Fig. 3.10. Rapid change of the curvature prevents from smooth transition from the co-planar waveguide modes to the traveling type waves at the near low frequency end. $|S_{11}|$ gets increased when the inner curve becomes a straight line which connects points E and B for $r_2 = 1.67$ due to a lack of smoothness at point E. From this evaluation, one can determine that the inner curve is the most important parameter to design frequency range of the antipodal Vivaldi antennas.

The proposed Vivaldi antenna belongs to a class of surface traveling wave antennas on which the traveling wave propagates with a phase velocity less than or equals to the speed of light. This propagation mechanism results in an endfire radiation. A smooth transition from the slotline propagation modes to the radiating field is a key for better antenna performance. In order to establish this transition for a wide frequency range, one should avoid discontinuous points and elaborate matching circuits in the propagation path. Mismatch may occur at the connections between the feeding line, the radiation flare profile, and the antenna aperture. So these parts of the antenna are designed carefully to satisfy the requirement of the UWB applications.

Firstly, basic dimensions of the antenna size (W) and feeding line (W_f, L_f) are determined first as initial values. To compare with the conventional microstrip feeding line on the ground plane, the twin lines of the feeding area reduce discontinue points in the antenna structure [53]. Secondly, the radiation flare profile (b_1, b_2, r_1, r_2) are chosen by observing S_{11} parameter and the radiation pattern characteristics. This simple radiation flare and smooth transition ensure a constant group delay. By making corrugated structure at the edges of the antenna [71, 72, 74], extending and shaping radiation flares [54], these modifications increase the discontinuous points in the antenna structures. It leads to not only manufacturing complexities but also a large variation of the group delay. From the endfire radiation mechanism of the antenna, the antenna gain depends on the aperture lengths of the antenna end (W_0, W_e) and the length of the antenna (L), as well as the uniformity of the aperture field distribution. These antenna dimensions will be optimized by using HFSS to get a flat gain in the UWB range. Thus final dimensions of the proposed antenna have been determined and listed in Table 3.2.

Table 3.2: The dimensions of the proposed antenna

Parameter	Value	Parameter	Value
W	100.00 mm	w_f	3.20 mm
L	95.00 mm	h	1.60 mm
L_1	76.46 mm	b_1	46.80 mm
L_f	18.54 mm	b_2	50.00 mm
W_0	56.60 mm	r_1	0.48
W_e	21.70 mm	r_2	1.67

3.2.3 Estimation for the low frequency end f_-

Estimation of the operational range is important, but it is not clear yet how to define the low frequency end f_- for Vivaldi antennas. The previous formula for f_- may be calculated from the width of the antenna, or the antenna aperture without detail explanation and different estimation formulae are available. For example, f_- is given in terms of the antenna width W in Refs. [49] and [58] as

$$f_-^{(1)} = \frac{c}{2W}, \tag{3.42}$$

while others have defined as

$$f_-^{(2)} = \frac{c}{W\sqrt{\varepsilon_r}},\ f_-^{(3)} = \frac{c}{2W\sqrt{\varepsilon_e}},\ f_-^{(4)} = \frac{c}{W}\sqrt{\frac{2}{\varepsilon_r+1}} \tag{3.43}$$

in Refs. [74], [70] and [75], respectively.

Here ε_r denotes the relative dielectric constant of the substrate and ε_e is the effective dielectric constant defined in Eq. (3.36). In these formulae, the width of the antenna W is the key to design low frequency f_-. However, you can observe in Fig. 3.8 that the f_- does not change for different W when the other parameters are fixed. As shown in Sect. 2.2, the inner curve is found to be the most effective parameter to $|S_{11}|$. The importance of the inner curve has been pointed out by other authors [76]–[80], but none of the works predicts well for the operational low frequency end f_-.

Figures 3.11 and 3.12 show the current distribution on the upper copper sheet and the electric field distribution at the center of the substrate at some frequencies. Standing wave type oscillation at the microstrip co-planar waveguide shifts gradually to the aperture with somewhat a longer oscillation period. One should note from the current distribution that the distance between two conjugative antinodes of the standing wave is related to the wavelength of the operating frequency. At higher operating frequency, we have more antinodes and the distance between two conjugative antinodes become smaller. This is a basic characteristic of traveling wave on the antenna structure. Below the low frequency limit f_-(=2.36 GHz), the current distribution in the vicinity of the aperture is very weak

in Fig. 3.11 (a), and the aperture electric field in Fig. 3.12 (a) is not uniform and becomes weak in the middle. It is found that from these figures the current (or electric field), which has a peak at the intersection point A, needs to oscillate along the flare curve at least once to reach the flare end point B for the proper radiation.

Arai and Nakada examined optimum taper slot parameters to increase the FB ratio for proximity coupled taper slot antennas, and concluded that radiation taper slot needs multiple of half wavelength for strong forward radiation [79], [80]. As their tapered slot antenna is designed for narrow band, and its radiation property is obtained at resonant frequency, it is not clear how one can interpret the operational frequency range for wide band antennas like Vivaldi antennas. In fact if one uses a straight flare (taper) for Vivaldi antenna, $|S_{11}|$ gets increased as shown in Fig. 3.10.

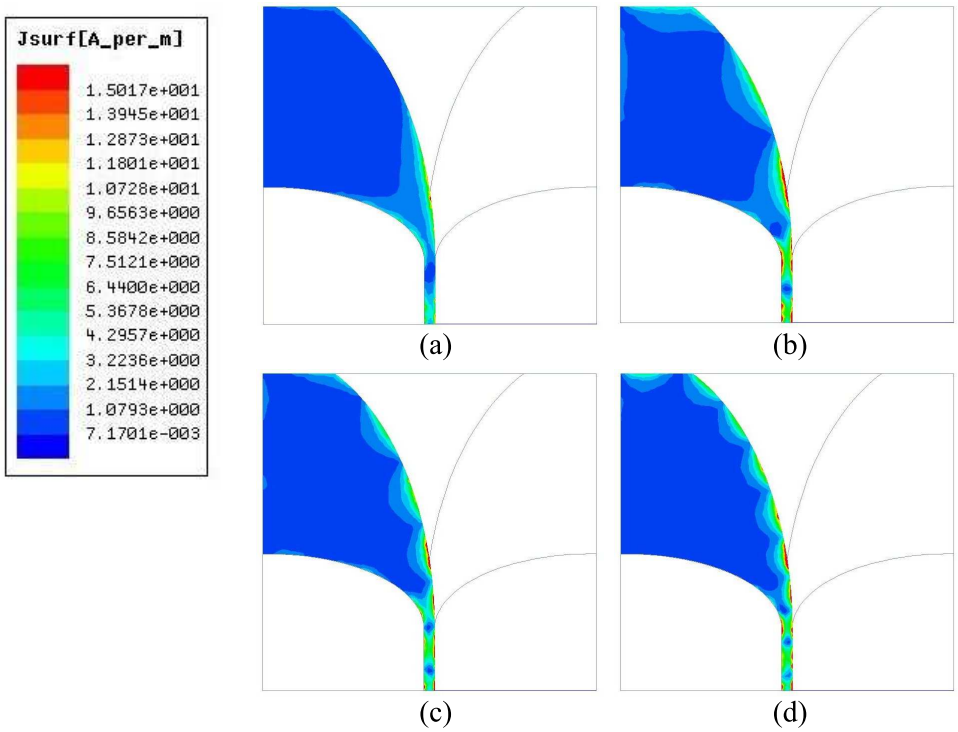

Figure 3.11: Current distribution at some frequencies (a) 2 GHz (b) 4 GHz (c) 6 GHz (d) 8 GHz

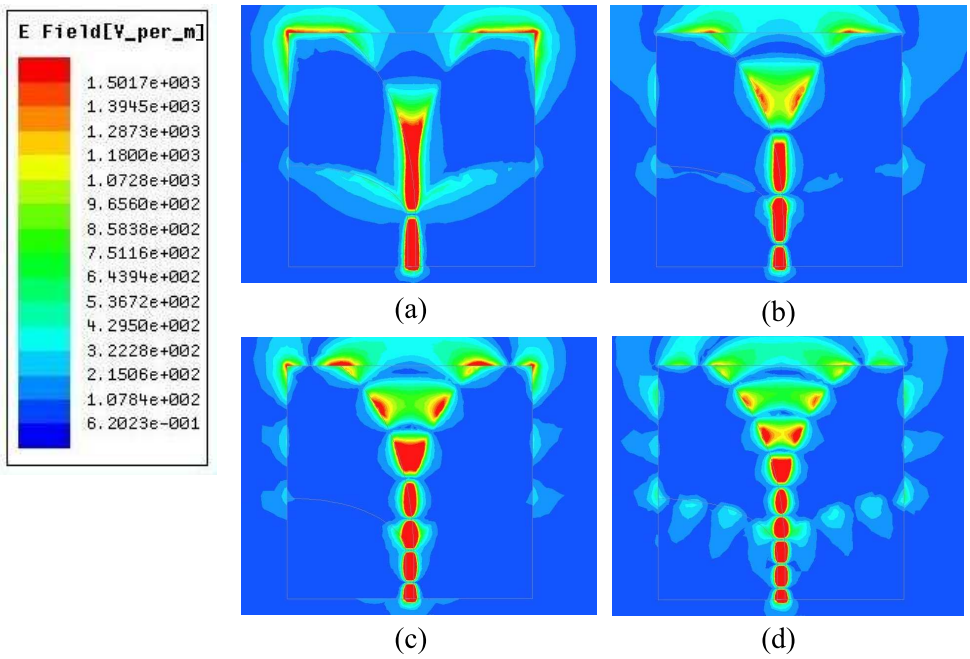

Figure 3.12: E field distribution at some frequencies (a) 2 GHz (b) 4 GHz (c) 6 GHz (d) 8 GHz

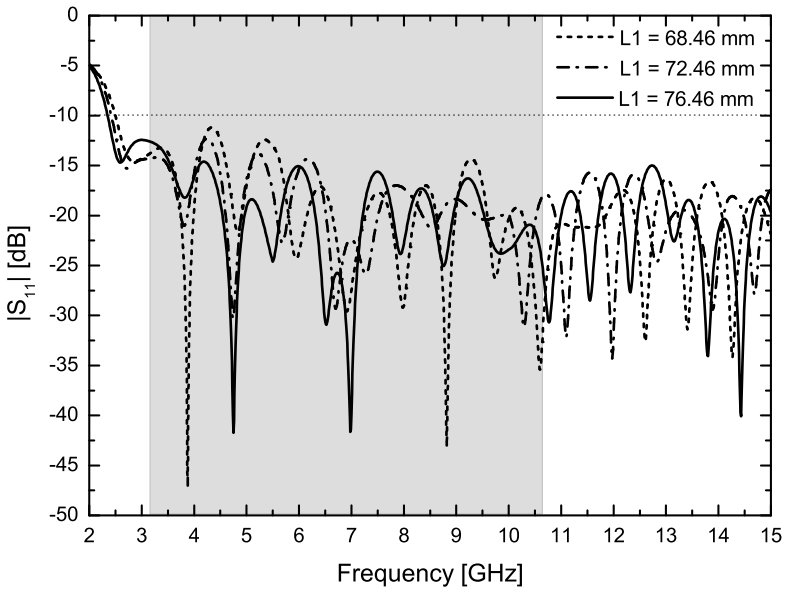

Figure 3.13: $|S_{11}|$ for different L_1

By changing the curved flare length L_1 in Fig. 3.13, the low frequency end f_- shifts gradually. Based upon this observation and the current distribution in Fig. 3.15 (a), we made an empirical assumption that the arc length of the inner curve from A to B becomes one half of the free space wavelength at the low frequency end. Namely, f_- can be approximately given by

$$f_- = \frac{c}{\lambda_-} = \frac{c}{2L_-}, \tag{3.44}$$

where L_- denotes the arc length between A to B. The arc length L_- of the ellipse can be derived analytically using the incomplete elliptic integrals of the second kind (see Appendix A). In order to confirm the accuracy of our formula, f_- was calculated for our final dimensions of the antenna in Table 3.2 and one gets $f_- = 2.40$ GHz ($L_- = 62.63$ mm). Reversely, if one wants f_- to be 4 GHz, one gets $L_- = 37.50$ mm from Eq. (3.44) and then $L_1 = 56.95$ mm from Eq. (A.4). Figures 3.14 and 3.15 show the simulated $|S_{11}|$ and the current distribution at low frequency end for these cases. As can be seen from Fig. 3.14, the low frequency end f_- of the antenna is 2.36 GHz for $L_- = 62.63$ mm and 4.00 GHz for $L_- = 37.50$ mm, respectively. At this low frequency end, one can also find very similar current distribution along the inner curve in Figs. 3.15 (a) and (b) with peaks at point A and B.

Table 3.3 shows the comparison of the low frequency end estimations. Our estimated f_- in Eq. (3.44) for Figs. 3.15 (a) and (b) are very close to those obtained from HFSS simulation and are far better than any previously proposed formulas in Eqs. (3.42) and (3.43). In this table, our estimation has been tested and compared for other Vivaldi antennas designed by other authors. From these comparisons, our estimation always gives good results.

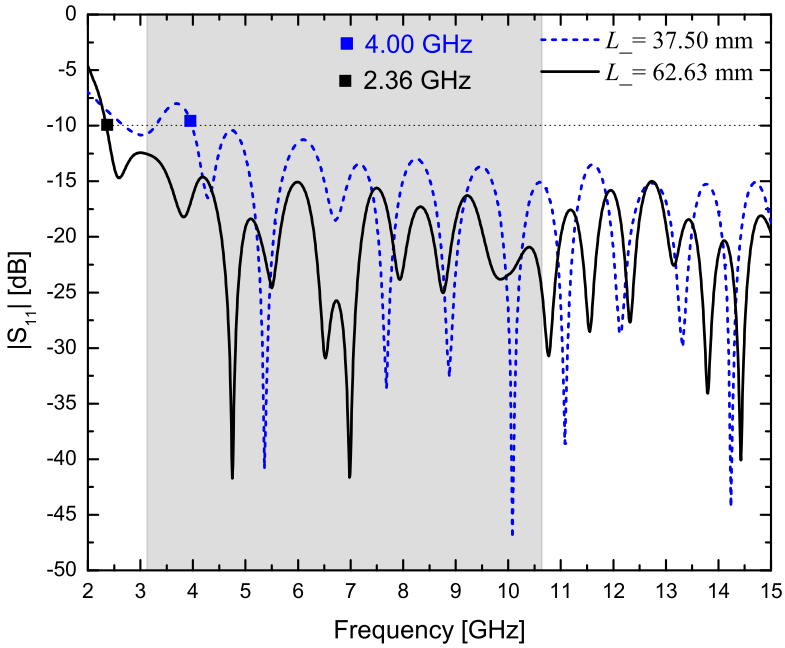

Figure 3.14: $|S_{11}|$ for different L_{-}

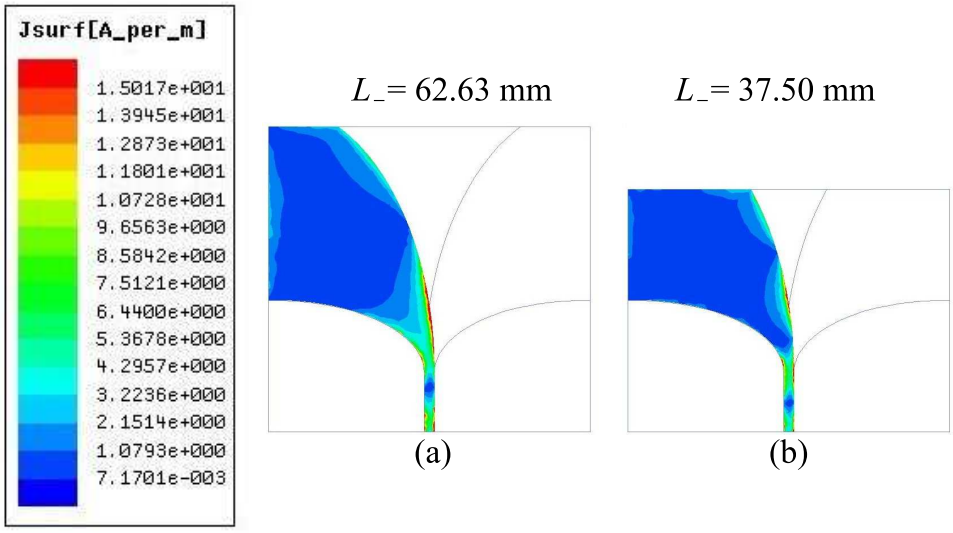

Figure 3.15: Current distribution at low frequency end f_{-} (a) $f_{-} = 2.36$ GHz, $L_{-} = 62.63$ mm (b) $f_{-} = 4.00$ GHz, $L_{-} = 37.50$ mm

Table 3.3: Comparison of the low frequency end estimations

Refs.	Models	Dimensions W, L_- [mm]	Dielectric constants ε_r, ε_e	$f_-^{(1)}$ [GHz]	$f_-^{(2)}$ [GHz]	$f_-^{(3)}$ [GHz]	$f_-^{(4)}$ [GHz]	f_- [GHz]	Result [GHz]
Ours	Fig. 3.15(a)	$W = 100.0$, $L_- = 62.63$	$\varepsilon_r = 4.40$, $\varepsilon_e = 3.34$	1.50	1.43	0.82	1.82	2.40	2.36
	Fig. 3.15(b)	$W = 100.0$, $L_- = 37.50$	$\varepsilon_r = 4.40$, $\varepsilon_e = 3.34$	1.50	1.43	0.82	1.82	4.00	4.00
Ref. [54]	Fig. 1	$W = 80.00$, $L_- = 62.09$	$\varepsilon_r = 3.38$, $\varepsilon_e = 2.67$	1.88	2.04	1.15	2.53	2.42	2.35
Ref. [56]	Fig. 1	$W = 31.20$, $L_- = 25.50$	$\varepsilon_r = 3.55$, $\varepsilon_e = 2.77$	4.81	5.10	2.89	6.37	5.88	6.00
Ref. [58]	Fig. 3(a)	$W = 64.00$, $L_- = 38.67$	$\varepsilon_r = 2.30$, $\varepsilon_e = 1.93$	2.34	3.09	1.69	3.65	3.88	4.00
Ref. [70]	$R_x = 0$	$W = 40.00$, $L_- = 44.62$	$\varepsilon_r = 3.00$, $\varepsilon_e = 1.43$	3.75	4.33	3.14	5.30	3.36	3.30
	$R_x = 10$ mm	$W = 60.00$, $L_- = 60.33$	$\varepsilon_r = 3.00$, $\varepsilon_e = 1.43$	2.50	2.89	2.09	3.54	2.49	2.30
Ref. [71]	Fig. 1(a)	$W = 48.00$, $L_- = 47.02$	$\varepsilon_r = 4.60$, $\varepsilon_e = 3.47$	3.13	2.91	1.68	3.74	3.19	3.30
Ref. [72]	Fig. 1(a)	$W = 36.30$, $L_- = 26.97$	$\varepsilon_r = 6.15$, $\varepsilon_e = 4.45$	4.13	3.33	1.96	4.37	5.56	5.28
Ref. [74]	Fig. 2(a)	$W = 22.00$, $L_- = 33.68$	$\varepsilon_r = 10.2$, $\varepsilon_e = 6.82$	6.82	4.27	2.61	5.76	4.45	4.70
Ref. [75]	Fig. 2	$W = 59.60$, $L_- = 53.75$	$\varepsilon_r = 10.2$, $\varepsilon_e = 6.74$	2.51	1.58	0.97	2.13	2.79	2.75
Ref. [78]	Fig. 3	$W = 175.0$, $L_- = 381.0$	$\varepsilon_r = 1.00$, $\varepsilon_e = 1.00$	0.86	1.71	0.86	1.71	0.39	0.35